공학박사학위논문

Ion Heating and Rotation Acceleration during Bursting MHD Events on Versatile Experiment Spherical Torus

VEST 장치에서 **Bursting MHD** 현상에 의한
이온 가열 및 회전 가속

2019년 8월

서울대학교 대학원
에너지시스템공학부
김 유 성

Ion Heating and Rotation Acceleration during Bursting MHD Events on Versatile Experiment Spherical Torus

VEST 장치에서 Bursting MHD 현상에 의한 이온 가열 및 회전 가속

지도 교수 황 용 석

이 논문을 공학박사 학위논문으로 제출함

2019 년 8 월

서울대학교 대학원
에너지시스템공학부
김 유 성

김유성의 박사 학위논문을 인준함

2019 년 8 월

위 원 장 나 용 수 (인)

부위원장 황 용 석 (인)

위 원 정 경 재 (인)

위 원 Yuejiang Shi (인)

위 원 고 원 하 (인)

Abstract

Ion Heating and Rotation Acceleration during Bursting MHD Events on Versatile Experiment Spherical Torus

Yoosung Kim
Department of Energy Systems Engineering
(Fusion & Plasma Engineering)
The Graduate School
Seoul National University

MHD instabilities in magnetically confined plasma significantly degrade the confinement and possibly leads to disruption. Plasma rotation and its shear have stabilization effects on various MHD instabilities such as NTMs (Neoclassical tearing modes) and RWMs (Resistive wall modes). On the other hand, MHD instabilities can have a significant influence on plasma rotation. While it is an important piece toward a thorough understanding of the interaction between MHD instabilities and plasma rotation, its experimental exploration has been limited to a few phenomena and still remains to be incomplete. In this thesis, detail dynamics of plasma rotation and ion temperature are

investigated in bursting MHD activity on VEST (Versatile Experiment Spherical Torus). For this purpose, a novel ion Doppler spectroscopy (IDS) is newly developed with a superb temporal resolution ranging from 0.2-1 ms. This IDS capability permits to investigate the bursting MHD activity with fast crash time (~0.3ms). Interestingly, significant toroidal rotation acceleration as well as ion heating is observed in the bursting MHD activity. In order to explain the sudden spin-up phenomenon, several candidate mechanisms are discussed and compared with the experimental result.

The fast IDS system is carefully designed and installed to measure the plasma rotation and ion temperature in VEST. A high throughput spectroscopic system is successfully developed by employing the transmission grating and by matching the etendue across the whole of the optical system. Fast temporal resolution can be attained to 1 ms for 10 spatial channels and 0.2 ms for one spatial channel. The diagnostic is based on the line emission of intrinsic carbon impurity and it can cover the R>0.5 m.

The measured spectra by the IDS system are averaged spectra over the line-of-sight. Doppler tomographic inversion technique is employed to extract the local plasma rotation and ion temperature from the line integrated spectra. However, the inversion problem is a highly ill-posed problem and the reconstructed results sometimes have an unphysically oscillating feature. Second-order Tikhonov regularization method is utilized to properly estimate the local plasma properties which are believed to be continuous. This method is based on the minimization of the cost function which includes not only the accuracy of measurement but also the smoothness of the solution. Also, appropriate quantification of the uncertainties of the IDS system is analyzed by considering the

propagation of errors of fitted parameters of spectra based on the numerical Monte Carlo (MC) method.

Bursting MHD activities are usually observed in the low q Ohmic discharge with low prefill gas in VEST. These events are characterized by a spike in the plasma current, loop voltage and a burst of magnetic fluctuations with a high frequency above 10 kHz. Magnetic fluctuation shows a very fast exponential growth with a typical time constant of tens of microsecond (~$100\tau_A$). Interestingly, fast IDS diagnostic reveals that significant toroidal rotation acceleration in the counter-Ip direction as well as ion heating are observed in the bursting MHD activity. The rotation and ion temperature are changed globally in the same manner in the entire of the plasma volume, which clearly shows that some kind of rotation torque and ion heating are acting on the plasma, instead of locally enhanced plasma transport. The rotation and ion temperature increase very fast with the time scale of < 300 μs and then recover slowly with the confinement time scale. Several physical mechanisms to account for the sudden spin-up are discussed in terms of temporal behavior, the direction of torque and torque amplitude. The considered mechanisms are reconnection outflows, toroidal electric field by reconnection process, enhanced electron loss, and NTV (Neoclassical toroidal viscosity) torque with offset rotation. Among them, NTV torque by non-axisymmetric magnetic fluctuation from the MHD activity seems to a most probable mechanism.

Strong plasma rotation accelerations during the MHD activities are experimentally investigated for the first time. This observation will help us understand the effect of MHD event in plasma rotation and temporal dynamics of MHD event. In

particular, this result suggests the possibility of the interplay between MHD instability and induced plasma rotation such as the self-organization process.

Keywords: Ion Doppler spectroscopy, Plasma rotation, MHD event, Spherical Torus, NTV, VEST
Student Number: 2013-21007

Contents

List of Tables

List of Figures

Chapter 1. Introduction

Development of alternative energy sources is an urgent issue because the world-wide energy demand is continuously growing. Nuclear fusion is one of the strong candidates for the future energy source. When light nuclei collide with a sufficient energy, they fuse to heavier nucleus releasing a huge amount of energy. The most probable nuclear fusion process is DT reaction, which is described by the following formula [1],

$$ {}_{1}^{2}D + {}_{1}^{3}T = {}_{2}^{4}He\ (3.5\ MeV) + {}_{0}^{1}n\ (14.1\ MeV). \qquad (1.1) $$

As a deuterium ion and a tritium ion collide with sufficient energy to generation fusion reaction, an alpha particle and a neutron are generated having energy of 3.5 MeV and 14.1 MeV, respectively. However, there is a strong coulomb barrier between ions and they require a certain amount of energy. Typically, DT fusion reaction requires temperature of at least 10 keV. The extremely high temperature with dense fuel density should be attained simultaneously to be economically feasible. The species in such a high temperature becomes plasma state which are fully ionized and separated by electron and ion. The most promising concept for the nuclear fusion is a Tokamak, which confine the ionized plasma in torus shape by using magnetic fields.

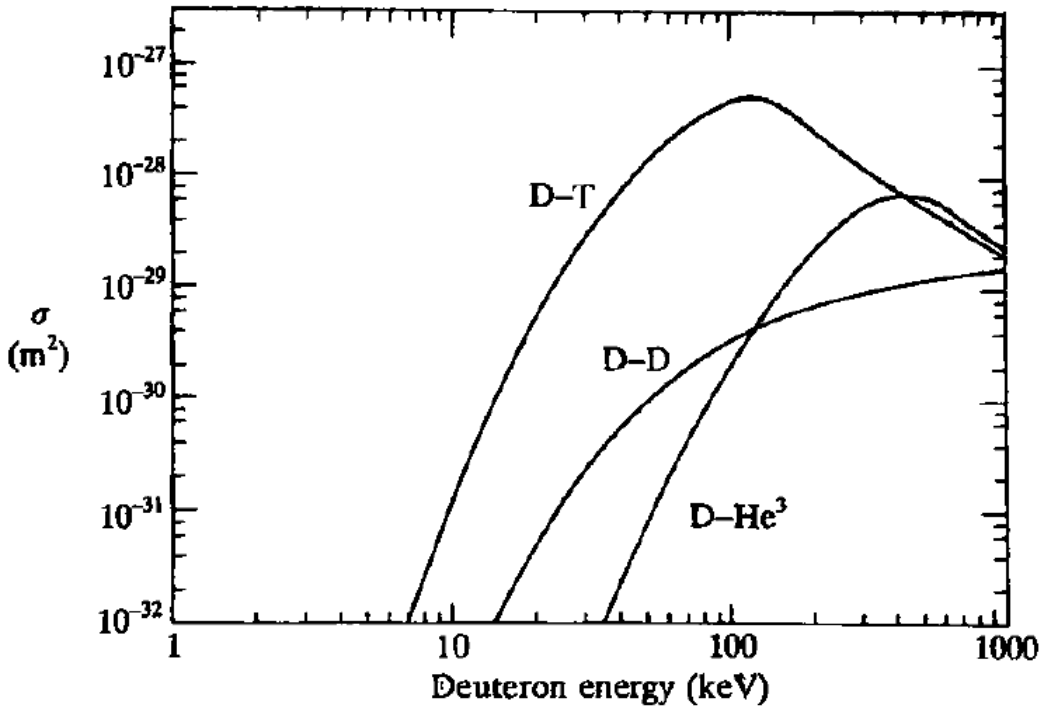

Figure 1-1 Cross-section for fusion reactions [2].

1.1. Tokamak

In the infinite electrical conductivity and zero viscosity (*i.e.* ideal MHD), the charged particle in magnetically confined plasma tend to stay within Larmor radius of a magnetic field. If the field line joins back on itself forming toroidal geometry, the particle will be confined by circulating along the field. This configuration can efficiently reduce the streaming out loss along the field line.

The usual method to produce a toroidal field is to wrap a series of coil around the toroidal vessel. This coil configuration makes *1/R* dependency on the toroidal magnetic field strength. An important consequence of this *1/R* dependency is drift motion by ∇B and magnetic curvature. If the field is purely in the toroidal direction, the ions and electrons are separated by drift motion and generation an electric field. $\mathrm{E} \times \mathrm{B}$ drift by combination with toroidal field cause species to go out of the plasma, resulting in complete loss of plasma confinement. One solution is to use poloidal magnetic field. The combination of a toroidal field and poloidal field forms helical field line which reduce drift loss from charge accumulation.

The tokamak is a device that generates the toroidal field using external coils and produces poloidal magnetic fields using a plasma current as shown in Figure 1-2. The helical magnetic field line is formed by a combination of a toroidal field and a poloidal field and confine a plasma in a stable equilibrium. The tokamak concept becomes mainstream in fusion research and has been investigated for several decades. An international megaproject called ITER (International Thermonuclear Experimental Reactor) is started to construct the largest facility in the world which demonstrates the

feasibility of the tokamak concept as a fusion reactor.

The spherical torus (ST) is a kind of tokamak with a low aspect ratio, which is the ratio of major radius to minor radius, R/a (Figure 1-3). Main advantages of spherical torus are compactness and high beta (β). The beta is defined as the ratio of plasma pressure to magnetic pressure indicating level of confinement.

$$\beta = \frac{\mathrm{p}}{B^2/2\mu_0} \tag{1.2}$$

Since START device has successfully demonstrated the high beta operation up to 40% [3], research on ST has been actively investigated on many ST devices including NSTX [4], MAST [5], ST-40 [6] and VEST [7].

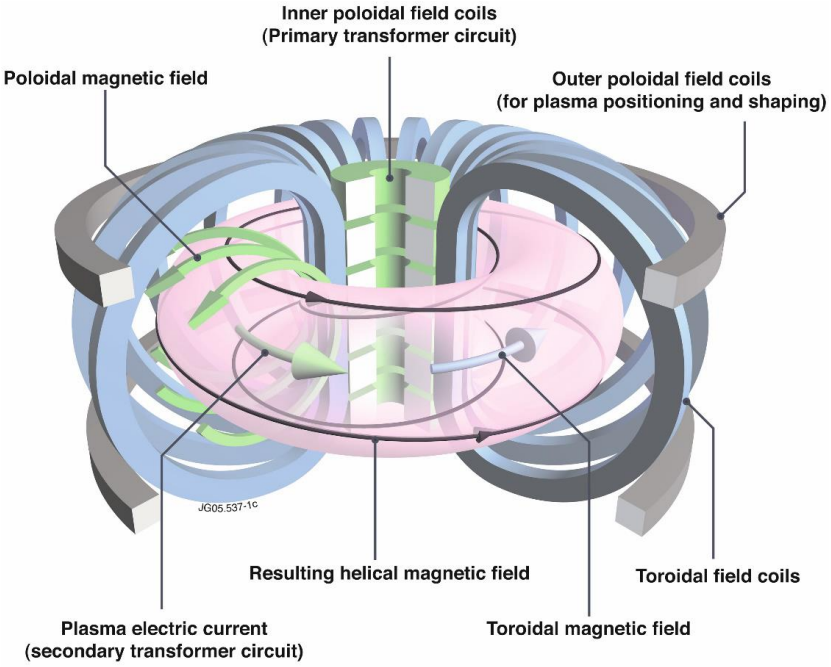

Figure 1-2 Schematic view of a tokamak with plasma current and magnetic field [8].

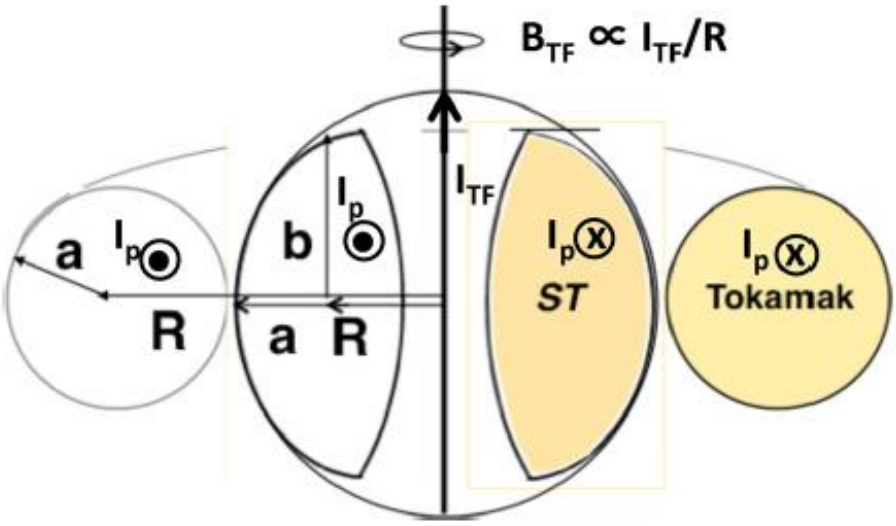

Figure 1-3 Schematic diagram of ST geometry compared to that of tokamak [9].

1.2. MHD Stability and Plasma Rotation

In a steady state, a tokamak plasma satisfies the MHD equilibrium ($\vec{J} \times \vec{B} = \nabla p$) and the magnetic field lines lay on the nested surfaces of constant pressure which are magnetic flux surfaces. However, a perturbation can trigger the large-scale MHD instabilities in unstable equilibrium. These instabilities distort the flux surface, significantly degrade the confinement [10] and possibly lead to disruption [11].

The role of plasma rotation on MHD stability is intensively investigated in many researches [12, 13, 14, 15, 16]. In particular, the rotation and its shear can stabilize the MHD instabilities including Resistive Wall Modes (RWMs) [16] and Neoclassical Tearing Modes (NTMs) [15]. On the other hand, the effects of MHD instability on plasma rotation is also reported such as momentum profile relaxation [17] and rotation damping [18, 19, 20](ex. Figure 1-4 and Figure 1-5). However, the detail effects are still unclear in many MHD instabilities owing to the complexity of the MHD effect. MHD activities have a strong transport effect on plasma current, heat and particles and significantly change the plasma equilibrium. In the MHD crash, the magnetic field lines break and magnetic reconnection occurs. The accompanying effects such as strong magnetic fluctuation, particle heating or acceleration also work on the plasma rotation. These effects potentially drive torque sources in a numerous way such as reconnection outflow, direct electron/ion loss, NTV torque, resonant torque, change in intrinsic rotation, etc. Nevertheless, the usual MHD transport simulation does not include the effect related to MHD events.

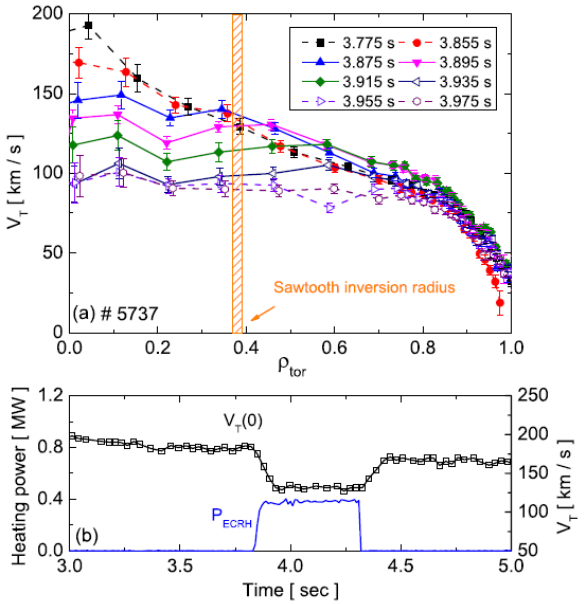

Figure 1-4 An example of rotation damping due to MHD instability. Internal kink mode is triggered by ECRH and clear rotation damping is observed in KSTAR [18].

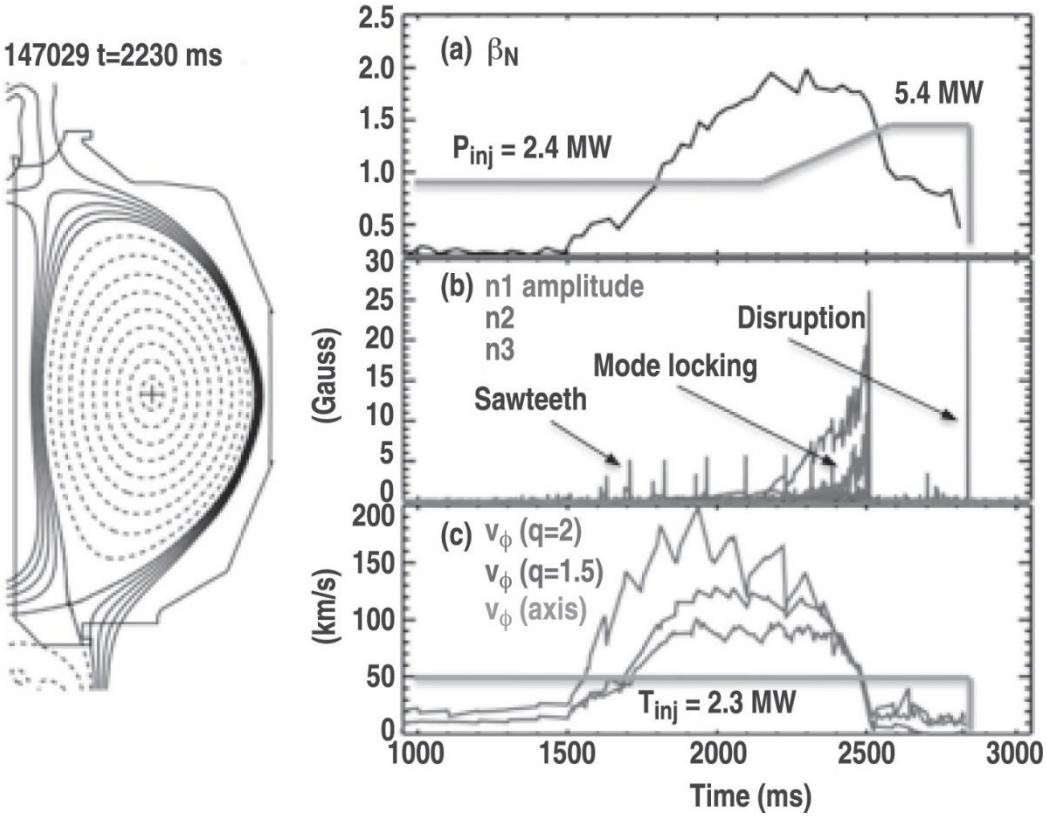

Figure 1-5 An instance of mode coupling and an associated collapse of ion fluid rotation [21]. (a) The evolution of β_N, and neutral power, P_{inj}. (b) RMS amplitude of magnetic fluctuations for n=1, n=2, and n=3. (c) Toroidal carbon impurity fluid velocity at the magnetic axis, the 3/2, and 2/1 rational surfaces. Modes decelerate and lock to the wall at 2.5 s, thermal quench begins at 2.8 s.

1.3. Versatile Experiment Spherical Torus (VEST)

Versatile experiment spherical torus (VEST) is a compact spherical torus that has been constructed for studying the innovative start-up, non-inductive current drive, and disruption studies. The schematic view of the devices and specifications are summarized in Figure 1-6. The additional heating and current drive systems including the electron Bernstein wave (EBW), lower hybrid fast wave (LHFW) current drive, and neutral beam injection (NBI) are under preparation for high beta operation in VEST. Recently, studies on MHD instability and disruption are carried out to understand the detailed physics on MHD precursor, mode onset, and disruption process.

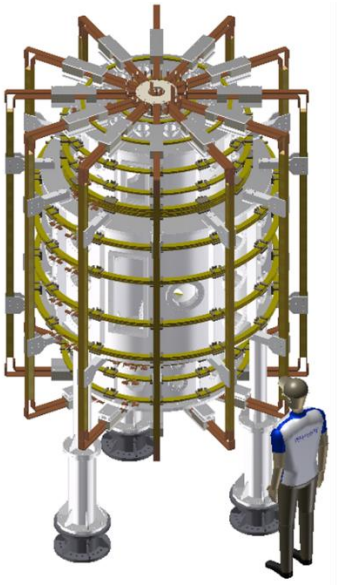

Parameter	Value
Toroidal B Field	0.1 T
Major Radius	0.44 m
Minor Radius	0.32 m
Aspect Ratio	>1.37
Plasma Current	<120 kA
H & CD (ECH, NBI, LHFW)	ECH (2.45GHz, 30kW) NBI (15keV, 600kW) LHFW (500MHz, 10kW)

Figure 1-6 Schematic view of VEST devices and specifications

1.3.1. Ohmic Discharge

The TF coil consist of 24 turns around the vacuum chamber and the one turn TF coil carry 8.3 kA to generate toroidal field of 0.1 T on the axis. The TF coils is powered by an ultracapacitor bank and the coil current is sustained during the end of discharge. VEST possesses several pairs of PF coils to provide Ohmic power (PF01), start-up (PF05) and position control (PF06, 10). The installed PF coil geometry in poloidal plane is shown in Figure 1-7

The PF coils are powered by the capacitor banks switched at the pre-programmed time sequence. PF05 is used for the formation of the trapped particle configuration which enables a more efficient ECH assisted startup. PF06 and PF10 provide the equilibrium field to control the plasma shape (elongation and triangularity) and position. PF01 is switched three times: C1 charges up the coil with current, C2 swings down to provide a loop voltage for a tokamak plasma startup, and C3 provides extra volt-second to persist the driving loop voltage.

The PEV (Piezo electric valve) injects a prefill gas prior to plasma discharge. The main gas used in VEST is hydrogen (H_2). It is noteworthy that the prefill gas pressure can be controlled by changing the PEV open time. Ohmic plasma operation is quite sensitive to the wall condition. Usually, the impurity (mainly oxygen) influx from the wall limits the plasma performance. In order to reduce the impurity contents, the plasma-facing components are covered with boron through a process of boronization. During the glow discharge cleaning, solid-state carborane is sublimed and deposited on the plasma facing components. This process is done every few run days.

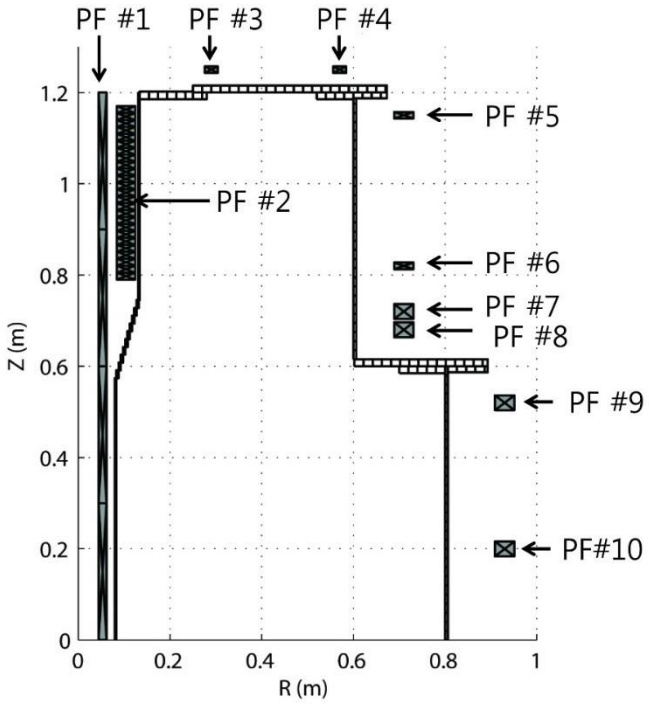

Figure 1-7 Schematics of PF coils system in a poloidal plane.

1.3.2. Diagnostics

The installed magnetic diagnostics is shown in Figure 1-8. The sampling rate of pick up coils and mirnov coils is 25 kHz and 250 kHz, respectively. Additionally, basic optical diagnostics such as a fast camera and line emission (H alpha, O I) monitoring systems are installed and operated.

Internal magnetic probes provide the direct measurements of magnetic fields and magnetic fluctuations inside the plasma [21]. A sensor group is composed of a Hall sensor to measure the equilibrium B_ϕ and two chip inductors to measure both equilibrium and fluctuating B_Z and B_R. The sensors are insulated by ¼ inch stainless steel pipe and 10 mm outer diameter alumina tube provides the thermal insulation. The cutoff frequency of Hall sensors and chip inductors are 23 kHz and 41 kHz, respectively. The probe can be moved between shots using the flexible vacuum bellows with a linear guide.

The Thomson system is a high-speed system capable of measuring the density and temperature of plasma in 1 ms resolution over a period of 10 ms by injecting a 2 J, 1 kHz burst laser into the plasma in a tangential direction, and is currently measuring both R = 0.37 and 0.47 m [22].

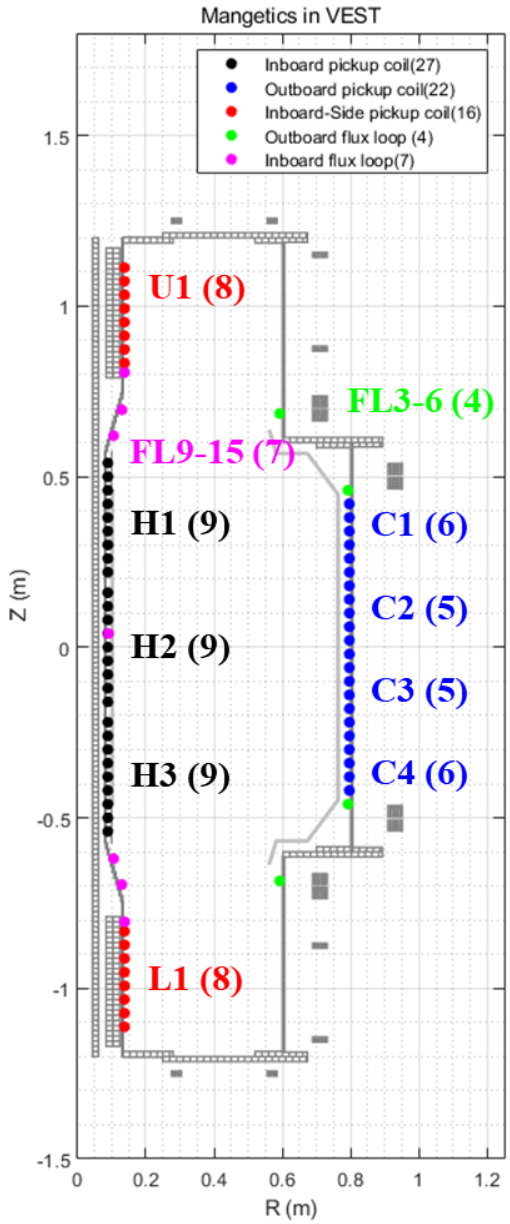

Figure 1-8 Magnetic diagnostics installed in VEST. There are 27 pickup coils on the inboard, 22 pickup coils on the outboard, and 8 pickup coils on the upper and lower chambers, respectively. 8 Flux loops are installed in inboard (7ea) and outboard (4ea).

1.4. Objectives of Research

The main purpose of this thesis is the experimental investigation of the plasma rotation during the bursting MHD event. However, the temporal resolution of conventional spectroscopy systems at present is only about 5 ms, which is far from meeting the requirements for related physics investigation. It is necessary to design and make the fast spectrometer with high throughput. The objectives of this thesis are,

1. Development of fast ion Doppler spectroscopy system in VEST
    - Design, install, and calibrate the spectroscopy system
    - Analyze the measured spectra and quantify the uncertainty of measurement

2. Experimental investigation of bursting MHD activity effect on plasma rotation
    - Detail spatio-temporal behavior of ion properties during bursting MHD events
    - Discuss the physical mechanism to account for the experimental observation.

Chapter 2. Ion Doppler Spectroscopy on VEST

In order to investigate the ion temperature and plasma rotation change during the fast MHD events, proper diagnostic of ion properties are required. Spectroscopic measurement of the Doppler shift and broadening in line emission of intrinsic carbon impurity is used to obtain the properties. It is called to ion Doppler spectroscopy (IDS). This technique is a non-invasive measurement technique without any perturbation to the plasma by collecting the light with an optics system installed outside the vacuum chamber. However, this technique has a limitation that the measured spectra are averaged over the line of sight. This limitation can be overcome by employing the proper Doppler tomographic inversion techniques [21, 22, 23]. Line integrated spectra are used to calculate the moments about the wavelength, which can be inverted to find local ion temperature and plasma rotation. The inversion problem is a highly ill-posed (underdetermined) problem. Proper regularization method is necessary to reduce the noise sensitivity in the inversion process. Also, appropriate quantification of the uncertainties is analyzed by considering the propagation of errors of fitted parameters of spectra.

Section 2.1 introduces the measurement principle of the IDS system. Detail hardware of ion Doppler spectroscopy is described in section 2.2. Calibration processes for intensity, wavelength, and spatial calibration are shown in Section 2.3. Section 2.4 presents data processing routines to analyze the raw spectra including spectrum fitting, inversion process, and uncertainty quantification.

2.1. Principle of Ion Doppler Spectroscopy (IDS)

The basic principle of IDS consists of measuring spectral profiles of emission lines from ions in the plasma which are excited by atomic processes such as electron impact excitation, charge exchange recombination, and electron capture. The relative motion of ions along the line-of-sight induces wavelength shift of emitted lines due to the Doppler effect as shown in equation (3.1).

$$\Delta\lambda = \frac{v}{c}\lambda_0 \cos\theta \,. \tag{3.1}$$

where $\Delta\lambda$ is the wavelength shift due to the Doppler effect, c is the speed of light, v is the speed of ion species for line radiation, θ is the angle between ion velocity direction and line-of-sight of measurement. From the linear relation between wavelength shift and ion speed, a spectroscopic measurement can provide a projection of the velocity-space distribution function. We expect the velocity distribution has the form of Maxwell-Boltzmann distribution, and ion temperature and ion rotation velocity can be determined from the Doppler broadening and Doppler shift of the spectra line. By selecting the wavelength window for the spectroscopic measurement, the diagnostic can be tuned for a particular ion species.

Line emissions from the low-Z impurities such as carbon, boron, helium, oxygen are usually used for spectroscopic measurement. However, these low-Z impurities have small ionization energy and are easily ionized to highly ionized states at the high electron temperature. For example, the equilibrium fractional abundance of carbon charge states is

drawn in Figure 2-1. The electron temperature of VEST plasma is in the range of 10-200 eV depending on the radial position. In this parameter ranges, various carbon charge states co-exist. Even though Figure 2-1 shows the result without considering transport effect (diffusion, convection, etc.) and this transport effect usually widen the charge state localization, each charge state ions are generally localized over some radial extent.

In this research, we choose the spectral line of CIII species near the 465 nm because of strong line intensity, available line database and relatively wide spatial coverage in VEST devices. Figure 2-2 shows a typically measured spectrum near the 465 nm. Strong triplet CIII lines (464.7 nm, 465.0, 465.15 nm) nm are located and overlapped with double OII lines. Detail deconvolution method of overlapped lines will be described in section 2.4. The radial extent for the CIII lines can cover from 0.5 m to 0.76 m (correspond to $\rho = 0.2 \sim 1$) as shown in Figure 2-3.

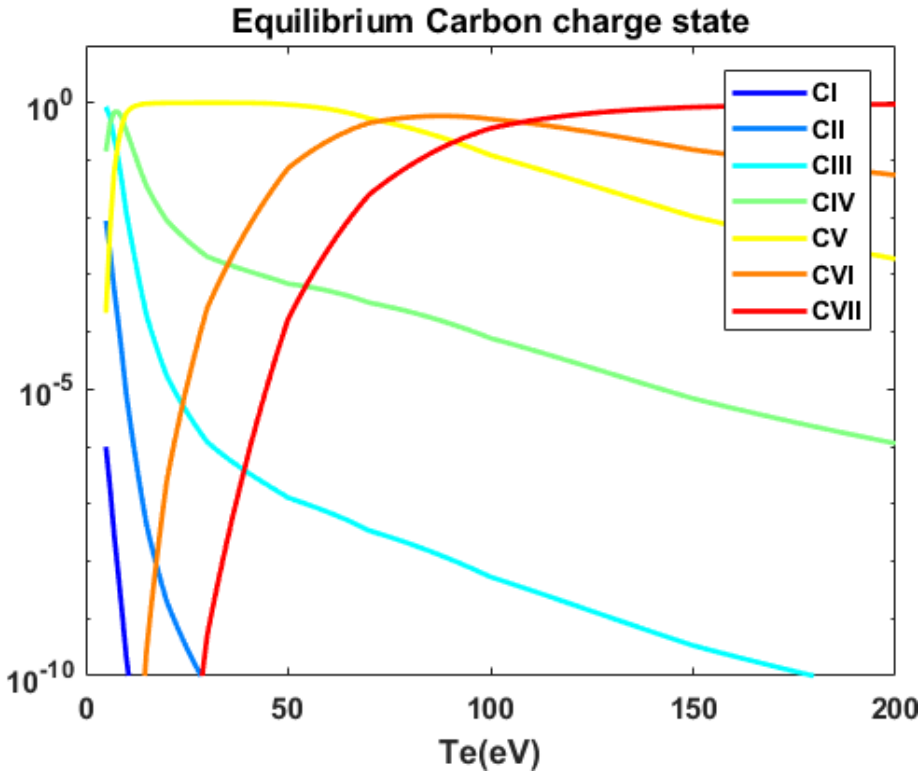

Figure 2-1 Equilibrium fractional abundances of carbon charge states calculated from a collisional radiative model with $n_e=10^{18}$ m^{-3} based on ADAS database

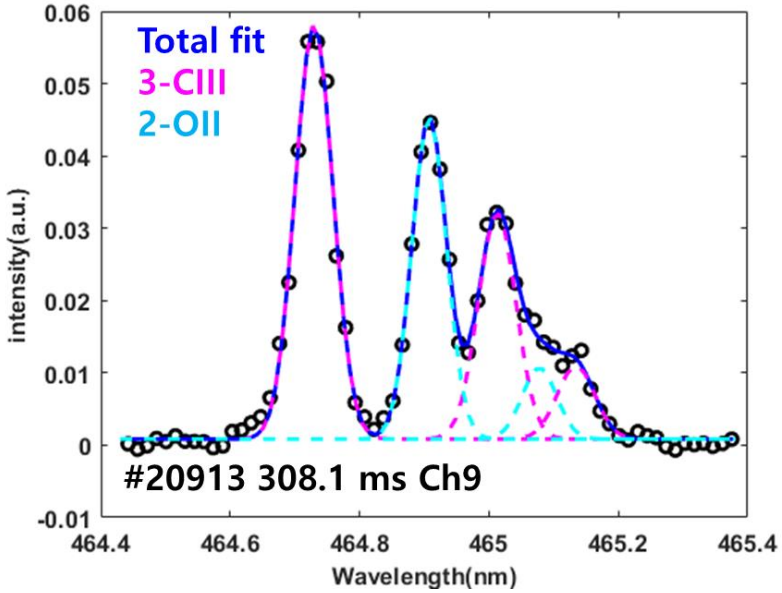

Figure 2-2 Typical measured spectra near the 465 nm. There are triplet CIII lines (magenta) and double OII lines (blue)

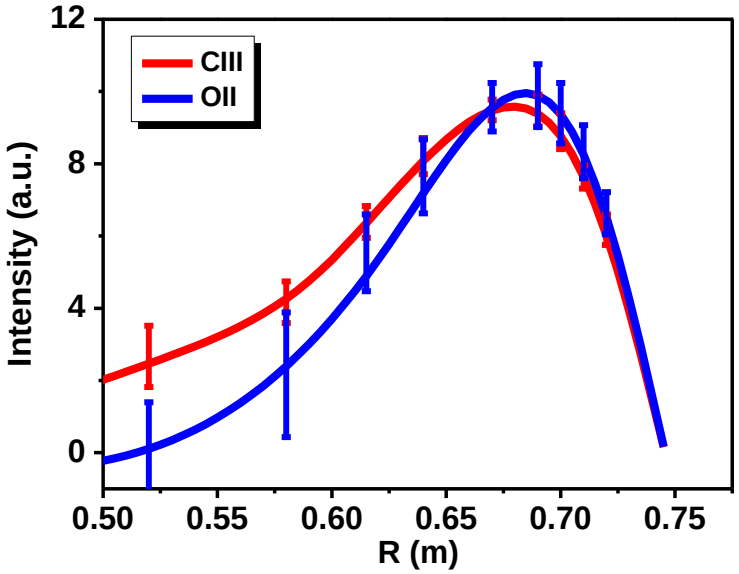

Figure 2-3 Radial emissivity profile of CIII at 464.74 nm and OII at 464.90 nm

2.2. Experimental Setup of IDS System

To measure the ion temperature and rotation with fast temporal resolution(<1 ms), dedicated system optimization as well as fast photon detector is essential due to the small signal levels compared to noises. Furthermore, low ion temperature and slow rotation require high dispersion spectrometer. High dispersion spectrometer spread out the light in broad wavelength domain and reduce the signal intensity in the pixel of the detector. In order to increase the signal intensity, careful system design has been conducted and presented in this section.

Figure 2-4 is a schematic illustration including the major components of the spectroscopic system. The system is mainly composed of viewing geometry, collection optics, fibers, and spectrometer.

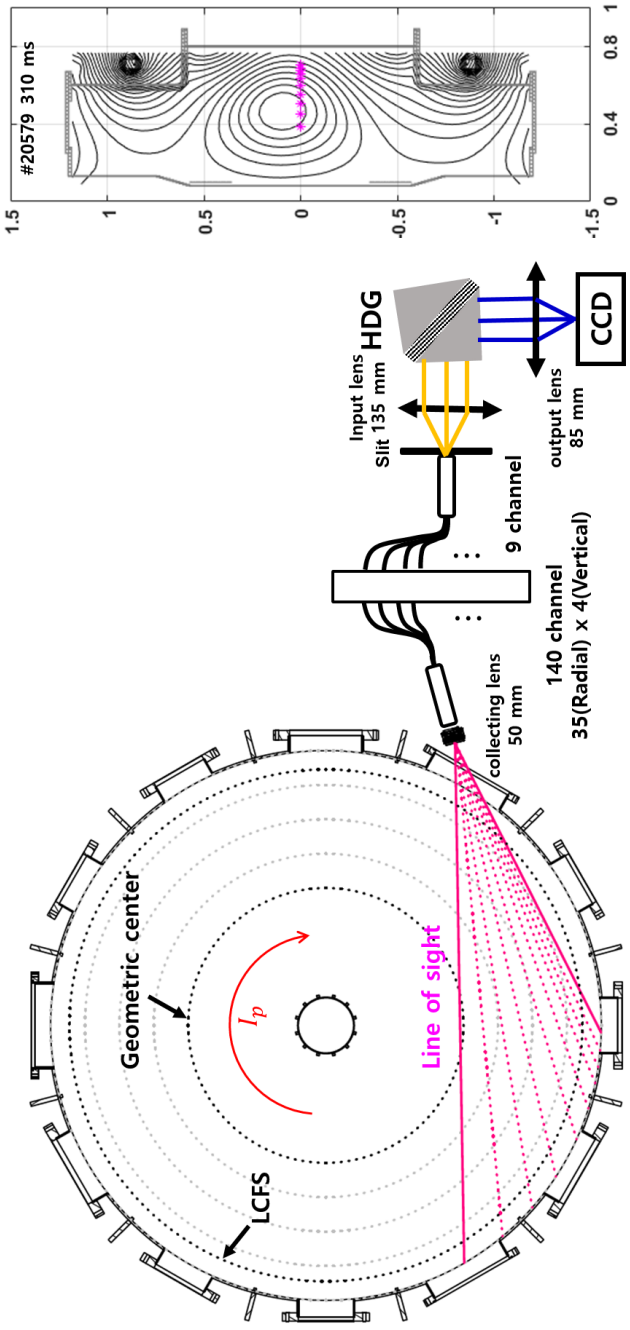

Figure 2-4 Schematic view of IDS system installed in VEST

2.2.1. Viewing Geometry

The toroidal viewing system is installed at the mid-plane of the chamber (see Figure 2-4). Wide-angle collection lens (f/2, f=35 mm) is used to image the outer half of the VEST plasma onto fibers optics. Nine radial channel is typically used for profile measurement and the tangential position of each channel is tabulated in Table 2.1. Actually, radial displacement of the measurement is adjustable by changing the optical fiber number installed in collecting optics down to 1 cm. The typical radial displacement is variable on the spatial position from 1 cm near the edge and 5 cm near the core. The uneven spatial measurement grids are helpful in the inversion process by measuring the strong edge emission accurately. The image spot size of each viewing channel is about 2-2.5 cm. The toroidal rotation in co-current direction induces the red-shift of lines peak in the given viewing geometry.

Table 2.1 Tangential position of spatial channels in IDS system in VEST

Channel	Fiber Number	R (m)	r/a
1	36	0.704	0.83
2	38	0.690	0.79
3	40	0.675	0.74
4	42	0.659	0.69
5	45	0.634	0.61
6	49	0.599	0.51
7	54	0.552	0.37
8	59	0.504	0.22
9	64	0.453	0.07
10	70	0.390	-0.1

2.2.2. Collecting Optics and Fibers

Lights from the plasma pass through a vacuum window and a collecting lens focus it onto the optical head of fiber bundle which consists of 140 fibers with 35 columns (radial) and 4 rows (vertical), each of which defines a line of sight through the plasma (see Figure 2-5). The diameter of optical fiber is 400 μm for the fiber core and 440 μm including cladding. Ten channels among the 35 radial channel in 2^{nd} row are used for measurement in the present setup. The other end of the fiber head is terminated with SC connector and attached to a patch panel as shown in Figure 2-6. Even if the patch panel has some connection loss (<20%), the patch panel makes it easy to handle the measurement position by plugging in the fiber in the spectrometer side.

In order to obtain the high optical throughput (*etendue*), the f-number of the optical components in measurement system should be matched. The collecting lens with a 35mm f/2 is well-matched to f-number of optical fiber (NA=0.22 correspond to f/2.2).

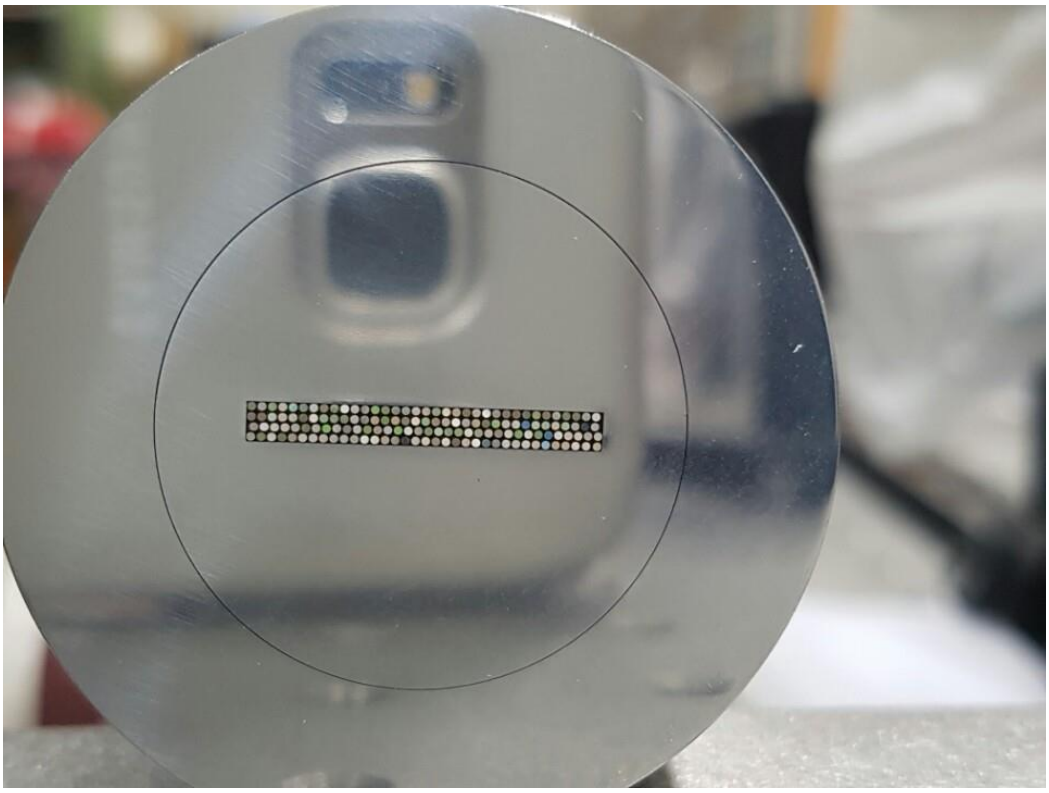

Figure 2-5 Image for the optical head of fiber bundle mounted in collecting optics. It consists of 140 fiber with 35 columns (radial) and 4 rows (vertical). The diameter of each fiber is 440 μm (400 μm for core, 40 μm for cladding). Uneven light intensity is due to the non-uniform light illumination.

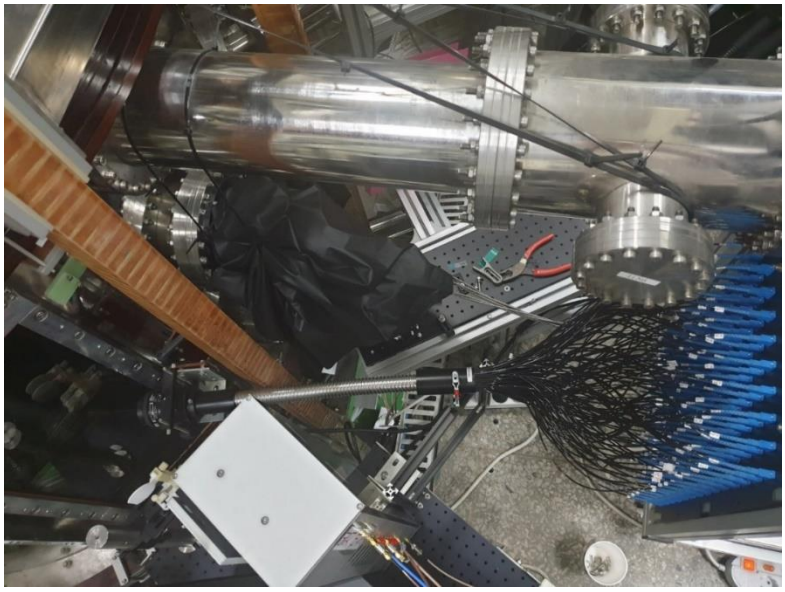

Figure 2-6 Collecting optics including collecting lens, fiber bundle, and patch panel.

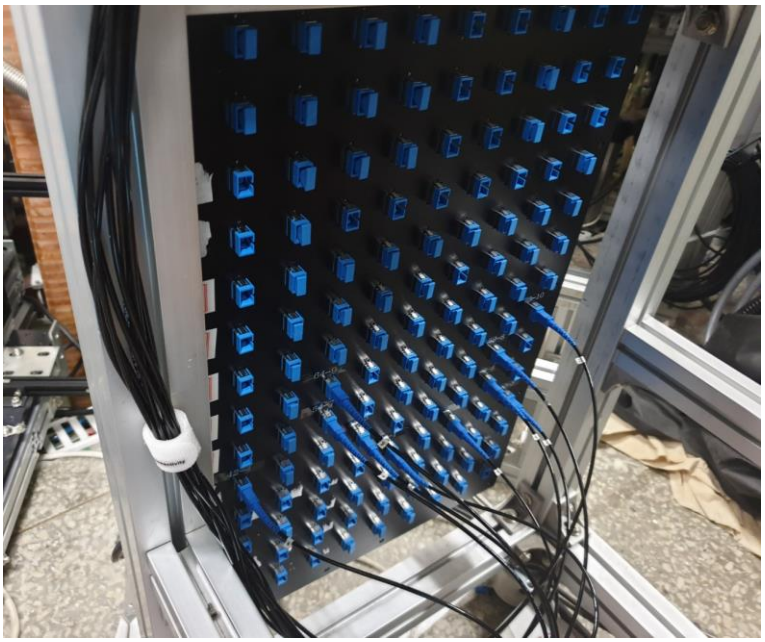

Figure 2-7 Patch panel in the spectrometer side. 10 spatial channel among the 140 channel is transferred to spectrometer

2.2.3. Spectrometer

The spectrometer installed in VEST is shown in Figure 2-8. Ten optical fibers from the patch panel are mounted onto fiber assembly. The fibers are vertically aligned inside the assembly and narrow entrance slit with 50 μm is attached to enhance the spectral resolution. The dichroic splitter (mirror) which transmits the high wavelength light (>550 nm) and reflects the light with short wavelength (<550 nm) is installed to share the line of sight with beam emission spectroscopy system planned in future [24].

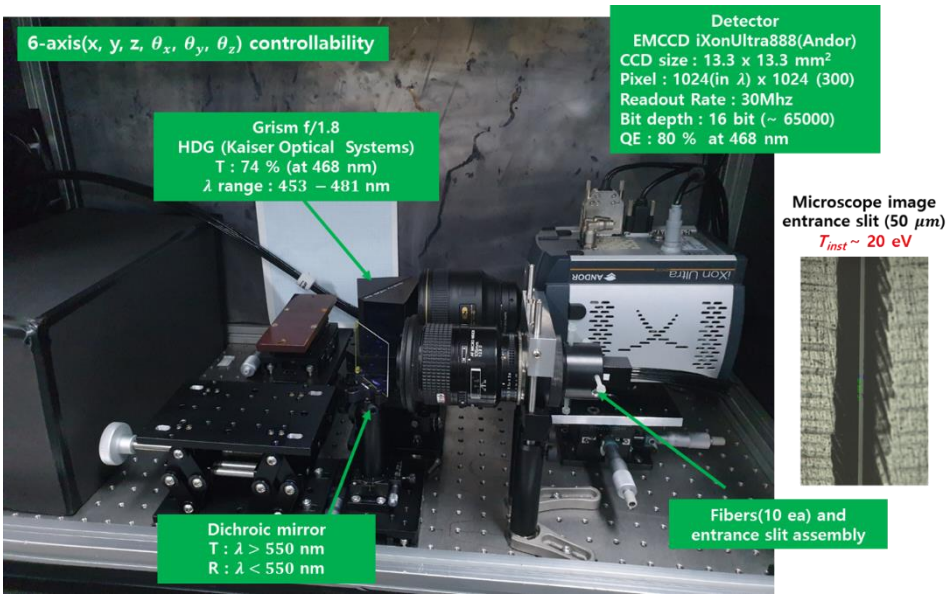

Figure 2-8 Image of spectrometer and detector. 50 μm entrance slit is mounted in fiber assembly.

Typical traditional spectrometers have used a long focal length system to increase the linear dispersion. In the common Czerny-Turner design [25], two mirrors with a long focal length are used to collimate and focus the light. This configuration is usually optimized for low aberration rather than optical throughput. The f-number of commercial Czerny-Turner spectrometer is quite large (typically, f/4-f/9) compared to typical optical fiber f-number f/2.2(i.e. NA=0.22). It requires the additional expanding optics to match the f-number between fiber and spectrometer. The development of short focal length spectrometer with transmission grating overcome the obstacle [26]. This grating offer many advantages over the Czerny-Turner spectrometer. High throughput (f/1.8) characteristics allow optical fiber to be directly mounted without inefficient matching optics. Also, transmission grating allows a full selection of m=1 diffraction and, optimizing the transmission efficiency (~70%). However, the transmission grating has a disadvantage in the ability for wavelength scanning. The grating has a narrow wavelength at the customized wavelength range and cannot tune the wavelength.

The high dispersion grating which is a special type of transmission grating sandwiched with two right-angle prisms is utilized in the IDS system. This grating-prism combination provides a higher dispersion. The grating is customized in the center wavelength at 468.6 nm s/n 56496. The transmission efficiency is 74% at the center wavelength.

The spectra are imaged in the 2D photon detector. The detector is a camera iXonUltra888 manufactured by Andor Technology Ltd. It is adequate in low light imaging environment with EMCCD (Electron Multiplying Charged-Coupled Devices) technology.

The thinned back-illuminated CCD provides 80 % quantum efficiency at 465 nm. The camera digitizes to 16 bits up to 30 MHz readout rate. The sensor has a 1024 × 1024 pixel array but only a 1024 × 300 pixel array is used to reduce the readout area. Each channel spans about 30 vertical pixels on the CCD. Vertical binning is performed on the chip to reduce readout time, forming an effective 1024 × 10 pixel array. The camera can be operated at 1 kHz for 10 channel measurements. For fast temporal measurement with scarifying spatial measurement, it can be operated in 5 kHz for 1 channel measurement. The CCD is cooled by a four-stage Peltier cooling assembly to -65 ℃ at a readout rate of 30MHz to minimize the dark noises.

In normal acquisition mode, the CCD is exposed for exposure time and must be blocked by the shutter while the charge is readout. In this research, the frame transfer mode is used. There are two regions in CCD sensor: exposed area and masked area. While the light is collected in the exposed area, collected data are readout in the masked area. The sensing and readout process are operated simultaneously in this mode. In this mode, the mechanical shutter is not necessarily needed. The CCD data acquisition is synchronized with the VEST master clock timing. When the plasma discharge signal is activated in the VEST control system [27], a master signal is transferred to a CCD camera 10 ms before the discharge. Then, the CCD camera begins to collect the light during the exposure period set by the operator. On completion of the exposure period, the camera performs the vertical shifts to the masked area and then collects the light again. This process repeats until discharge finished. In 1 kHz frame rate, the exposure time is 0.838 ms.

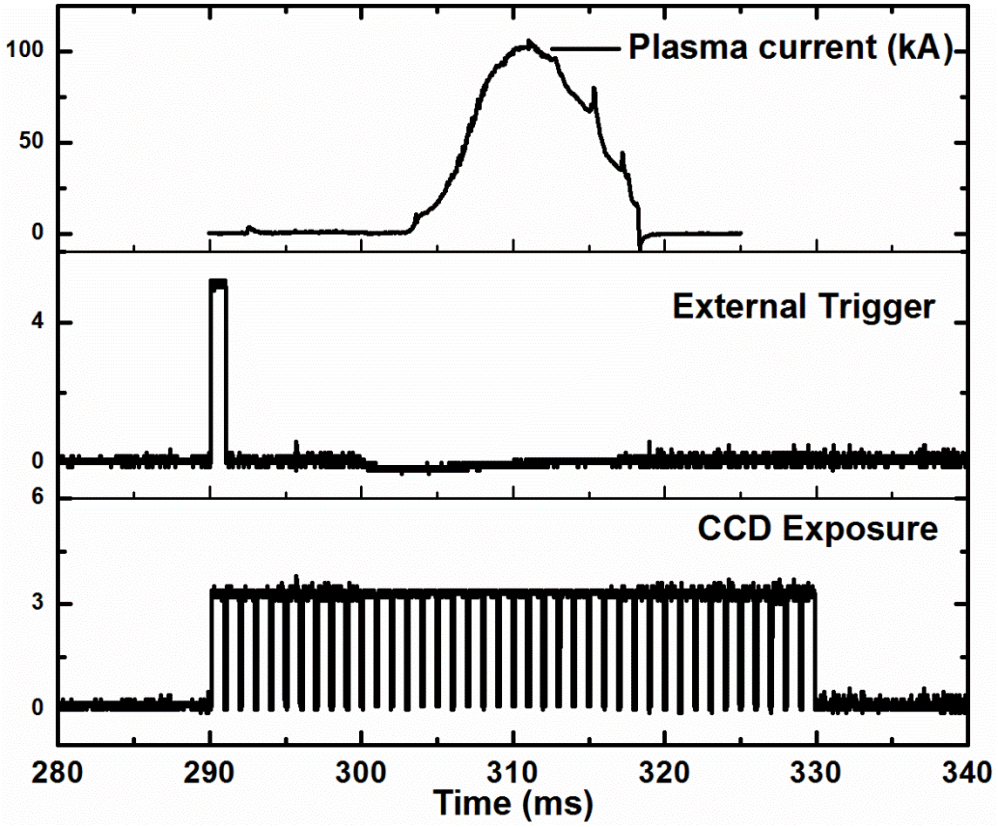

Figure 2-9 CCD timing diagram. CCD exposure timing is synchronized to the VEST master clock provided by external trigger input.

2.2.4. Optical Characteristics

A high throughput optical system is necessary in order to reduce the noises in the measurement. The throughput can be characterized by a photon efficiency and a geometric factor known as the *etendue*. The etendue is defined as

$$G = \int_S \int_\Omega n^2 \cos\theta d\Omega dS \,. \tag{3.3}$$

Where n is the index of refraction of the surrounding medium, θ is the angle of the light to the surface normal. By definition, etendue can be considered as a volume in phase space. If a lens is capable of transmitting light over a large angle and large area, it has a large value of etendue.

The important characteristic of the etendue is that the etendue of the whole optical system is limited by the minimum etendue across all of the optical components. The excess etendue in the system is wasted of resource and insufficient etendue of the optical component limits the total optical throughput. Therefore, the etendue of a well-designed system is matched to the etendue of the whole optical components. The geometric specification for the acceptance angle of the optical element is given by f-number which is the ratio of the focal length to the diameter of the entrance pupil. The f-number is usually written in the notation f/#, where # is the numeral value for f-number. Also, the numerical aperture (NA) which is a measure of the acceptable angle in optical fiber is related to the f-number. Approximately, the f-number is 0.5/NA.

2.3. Calibration of the System

Appropriate calibration of any diagnostics is a critical part to analyze the data properly. There are many misalignment sources in the tokamak experiment such as strong magnetic field, mechanical vibration, electromagnetic waves, and human carelessness. There are three kinds of calibrations: Wavelength calibration, Intensity calibration, spatial calibration. Intensity and spatial calibration require in-vessel access and only available during a vacuum opening period. Wavelength calibration is performed before and after the daily shot schedule.

2.3.1. Wavelength Calibration

Wavelength calibration is a procedure to map from the detector pixel number to wavelength. This procedure is performed by measuring the spectra of a xenon discharge lamp. The spectral peaks tabulated in Table 2.2 are matched to measured peaks in detector pixel. The relation between pixels to wavelength is not purely linear but somewhat curved due to the short focal length astigmatism. In wavelength calibration, a cubic polynomial is used to map from pixel to wavelength.

At first, the measured spectra are fitted with a sum of Gaussian in the CCD pixel domain. The sub-pixel resolved peak position by the fitting result is used to find the coefficients of a cubic polynomial. This procedure is conducted in each spatial channel day by day. In the real situation, the measured spectrum is multiplied by gain coefficients to calibrate the intensity (will be explained in Section 2.3.2) and the gain coefficient has a wavelength dependency. It can induce the small shift in peak wavelength and iterated wavelength calibration may be required to obtain the wavelength error below 10^{-4} nm.

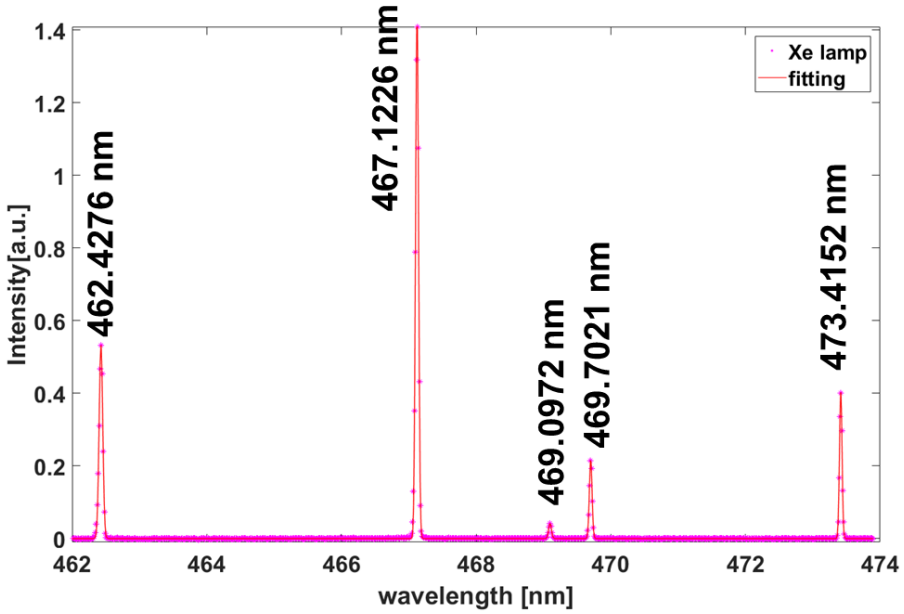

Figure 2-10 Xe discharge lamp spectrum. Five characteristic lines are used for wavelength calibration.

Table 2.2 List of characteristic lines of Xe I.

Wavelength	Transition
462.4276	$5p^5(\,^2P^o_{3/2})6s^2[3/2]^o_2 - 5p^5(\,^2P^o_{3/2})7p^2[3/2]_2$
467.1226	$5p^5(\,^2P^o_{3/2})6s^2[3/2]^o_2 - 5p^5(\,^2P^o_{3/2})7p^2[3/2]_3$
469.0972	$5p^5(\,^2P^o_{3/2})6s^2[3/2]^o_2 - 5p^5(\,^2P^o_{3/2})6p^2[3/2]_1$
469.7021	$5p^5(\,^2P^o_{3/2})6s^2[3/2]^o_2 - 5p^5(\,^2P^o_{3/2})7p^2[5/2]_2$
473.4152	$5p^5(\,^2P^o_{3/2})6s^2[3/2]^o_2 - 5p^5(\,^2P^o_{3/2})6p^2[3/2]_2$

2.3.2. Intensity Calibration

Intensity calibration is a critical process to analyze the measured spectrum. From the emission position to the detector, the light transmits the numerous optical component and is attenuated in various ways. Also, the attenuation is wavelength dependent and it may lead to a systematic error in spectral peak shift without intensity calibration. In order to obtain the accurate plasma parameter, proper correction is required.

Intensity calibration is performed by using an integrating sphere with a tungsten-halogen lamp mounted. Integrating sphere is a spherical cavity with an inner surface coated with highly diffusive reflective material. Light incident on any point on the inner surfaces is evenly distributed over all angles through multiple reflections. The sphere creates a reference radiation source suitable for the radiometric calibration. Ideally, the illuminated light is nearly independent of distance and angle, so small misalignment is acceptable as long as the sightline image completely enters the mouth of the cavity. The integrating sphere light source is calibrated by a calibrated lamp that is calibrated (LS-1-cal, Ocean Optics) based on the standard of NIST (National Institute of Standard and Technology).

The sphere is brought into the vacuum vessel and placed in the line-of-sight of each channel. Then, the detector captures the signal across the whole optical components in exactly the same condition as the actual experimental condition. The schematics of intensity calibration is shown in Figure 2-11. The gain coefficient is obtained as follows,

$$\mathrm{G} = \frac{spectral\ radiance\ (cm^{-2}s^{-1}\ nm^{-1})}{\#\ of\ count\ /\ exposure\ time}. \qquad (3.4)$$

The gain coefficient depends on the spatial channel and wavelength. The example of thegain coefficient is plotted in Figure 2-12.

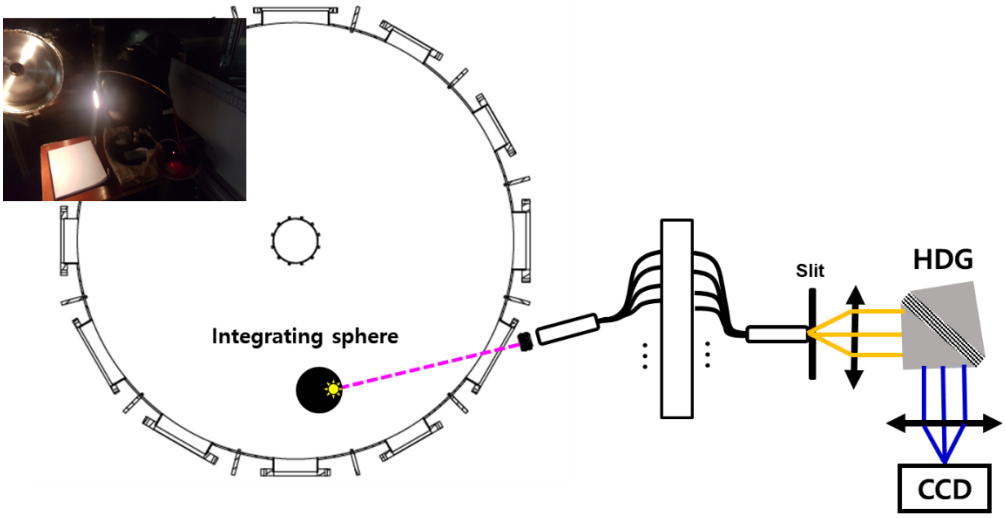

Figure 2-11 Schematic set-up for intensity calibration. Integrating sphere with halogen lamp is used for calibration

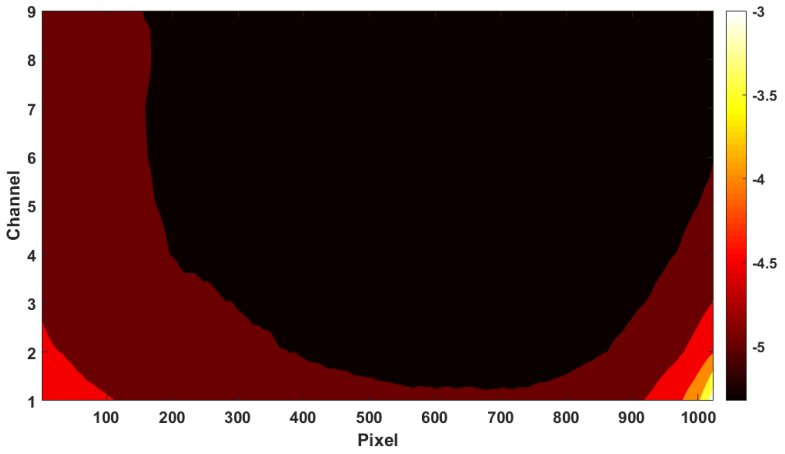

Figure 2-12 Gain coefficient as a function of wavelength and spatial channel.

2.3.3. Spatial Calibration

The exact spatial locations of the measured line-of-sight are verified through spatial calibration. The calibration is carried out by illuminating the light on the other side of the collection optics and measuring the image formed inside the vacuum vessel. The grid paper is placed in the path of line-of-sight and the illuminated image is carefully checked (see Figure 2-14). It is conducted in two different spatial locations to define a line-of-sight as shown in Figure 2-13. Two measurement points of each channel define an exact line of sight which is compared with estimated positions from that of mechanical drawing. Satellite images beside the original illuminated images are originated from the internal reflection inside the quartz window.

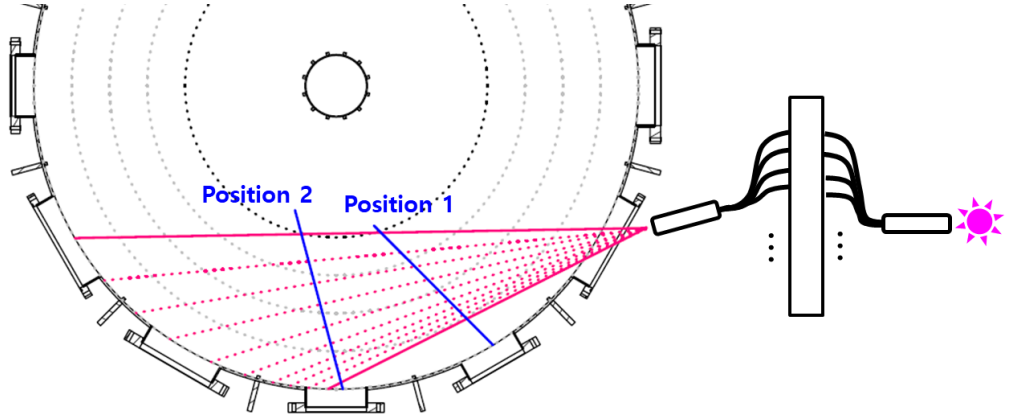

Figure 2-13 Schematic set up of spatial calibration. Backlighting the channels from the patch panel and measured the chord positions on a screen placed in the vessel. The spatial calibration is done in two different calibration position: Position 1, Position 2

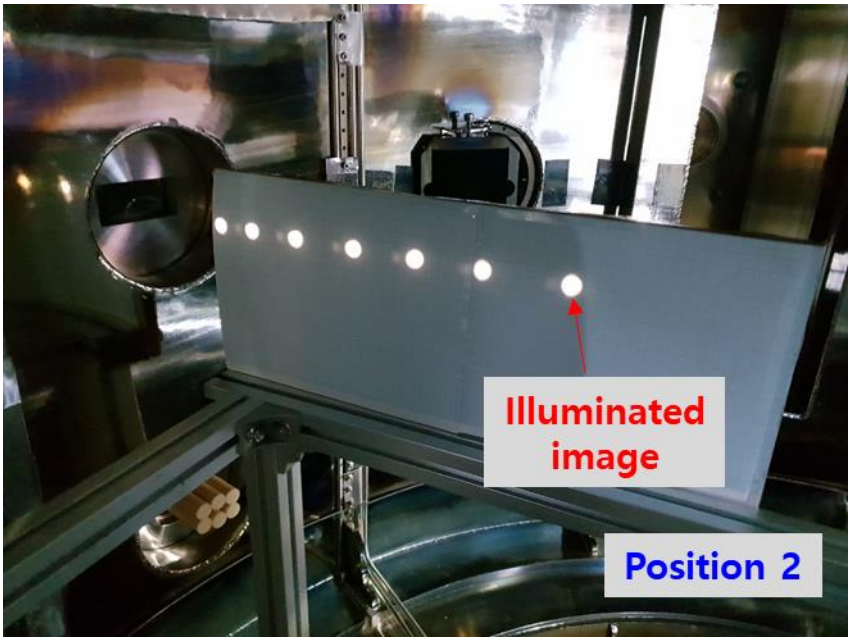

Figure 2-14 Illuminated image inside the vacuum vessel in calibration position 2.

2.4. Data Processing and Uncertainty

2.4.1. Spectrum Fitting Algorithm

Figure 2-2 shows a typically measured spectrum from the VEST discharge near the 465 nm. The CIII triplet lines (464.742, 465.025, and 465.147 nm) are multiplet lines from the LS coupling in the ^3P-$^3S_1$ transition as shown in Figure 2-15. [28, 29]. The upper state energies are split by spin-orbit interaction in LS scheme and the relative intensities in the pure LS coupling is well-known by the Burger-Dorgelo-Ornstein sum rule [30]. Each population of the energy states of upper and lower states of the line transitions should be statistically populated. Therefore, the ratios of the line intensities depend not on plasma parameters (n_e, T_e, etc.) but the atomic physics. We can check the degree of fitness by comparing the theoretical intensity ratios with measured ratios. There are two interference line from OII near 465 nm as shown in Figure 2-2. In order to extract CIII information, the measured spectra are fitted by a combination of five Gaussian functions with a constant baseline as following,

$$
\begin{aligned}
&F(I_{cont}, I_{CIII-1}, I_{CIII-2}, I_{CIII-3}, I_{OII-1}, I_{OII-2}, FWHM_{CIII}, FWHM_{OII}, \Delta\lambda_{CIII}, \Delta\lambda_{OII}; \lambda) \\
&= I_{cont} \\
&+ I_{CIII-1}\left(\frac{\sqrt{4\ln 2}}{\sqrt{\pi} FWHM_{CIII}}\right) \exp\left(-\frac{4\ln 2}{FWHM_{CIII}}(\lambda - \lambda_{CIII-1} - \Delta\lambda_{CIII})^2\right) \\
&+ I_{CIII-2}\left(\frac{\sqrt{4\ln 2}}{\sqrt{\pi} FWHM_{CIII}}\right) \exp\left(-\frac{4\ln 2}{FWHM_{CIII}}(\lambda - \lambda_{CIII-2} - \Delta\lambda_{CIII})^2\right) \\
&+ I_{CIII-3}\left(\frac{\sqrt{4\ln 2}}{\sqrt{\pi} FWHM_{CIII}}\right) \exp\left(-\frac{4\ln 2}{FWHM_{CIII}}(\lambda - \lambda_{CIII-3} - \Delta\lambda_{CIII})^2\right) \\
&+ I_{OII-1}\left(\frac{\sqrt{4\ln 2}}{\sqrt{\pi} FWHM_{OII}}\right) \exp\left(-\frac{4\ln 2}{FWHM_{OII}}(\lambda - \lambda_{OII-1} - \Delta\lambda_{OII})^2\right) \\
&+ I_{OII-2}\left(\frac{\sqrt{4\ln 2}}{\sqrt{\pi} FWHM_{OII}}\right) \exp\left(-\frac{4\ln 2}{FWHM_{OII}}(\lambda - \lambda_{OII-2} - \Delta\lambda_{OII})^2\right).
\end{aligned}
\tag{3.5}
$$

Where

I_{cont} : Constant background signal

I_{CIII-1} : CIII line intensity at 464.742 nm

I_{CIII-2} : CIII line intensity at 465.025 nm

I_{CIII-3} : CIII line intensity at 465.147 nm

I_{OII-1} : OII line intensity at 464.914 nm

I_{OII-2} : OII line intensity at 465.084 nm

$FWHM_{CIII}$: Full width Half Maximum of CIII line spectrum

$FWHM_{OII}$: Full width Half Maximum of OII line spectrum

$\Delta\lambda_{CIII}$: Wavelength shift of CIII line spectrum

$\Delta\lambda_{OII}$: Wavelength shift of OII line spectrum

The ten free parameters are used to fit the data. The same spectral widths and shifts for the same species are imposed because of the same ion temperature and rotation velocity. As mentioned before, triplet line ratios of CIII are used to confirm the goodness of fit as shown in Figure 2-16. Spectrum fitting method with all of the five spectral lines can enhance the robustness of fitting from the unwanted noises.

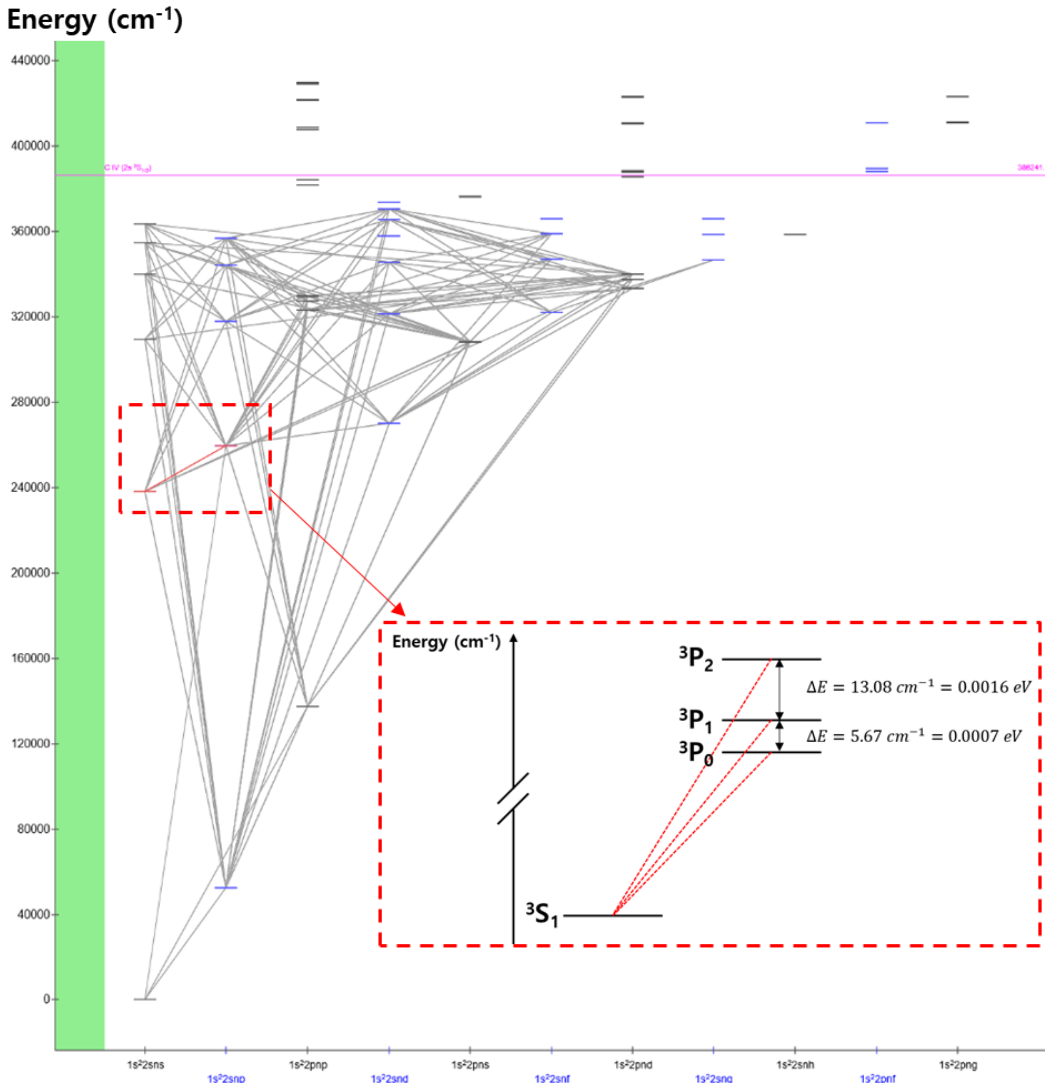

Figure 2-15 Grotrian diagram for the triplet system of CIII. The CIII lines of 464.742, 465.025, and 465.147 nm are indicated in red [28].

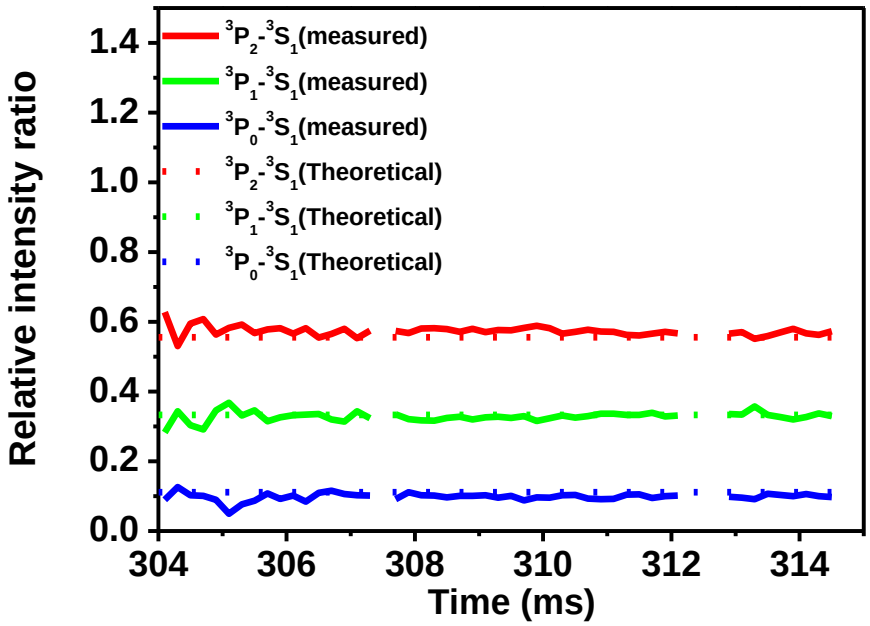

Figure 2-16 Measured CIII triplet line intensity ratios in #20913 are compared with theoretical ratios.

2.4.2. Doppler Tomographic Inversion

Measured spectra are averaged along a line of sight through a volumetric light source (plasma). In the tokamak device, we can assume the toroidal symmetry and circular Abel-like inversion can be used. In the VEST environment, spectral broadening mechanism except Doppler broadening is negligible such as natural broadening, stark broadening, and Zeeman splitting. The spectral broadening is mainly due to the Doppler broadening and it has the spectral shape of Gaussian. Assuming Gaussian line shape, the measured spectral power along the line of sight index *j* is

$$P_i(\lambda) = \sum_j E_j \left(\frac{\sqrt{4\ln 2}}{\sqrt{\pi} FWHM_j}\right) \exp\left(-\frac{4\ln 2}{FWHM_j}(\lambda - \lambda_0 - \Delta\lambda_j)^2\right) L_{ij} \cdot \quad (3.6)$$

Where

E_j : The local emissivity at position index *j* in photon/m^{3}s

$FWHM_j = \lambda_0 \left(\frac{8\ln(2) T_j}{Mc^2}\right)^{1/2}$: Doppler width of the line spectrum at position index *j*

$\Delta\lambda = \left(\frac{v_j}{c}\right) cos\theta_{ij}$: The Doppler shift of the line spectrum at position index *j*

L_{ij}: The discrete length element at position index *j*

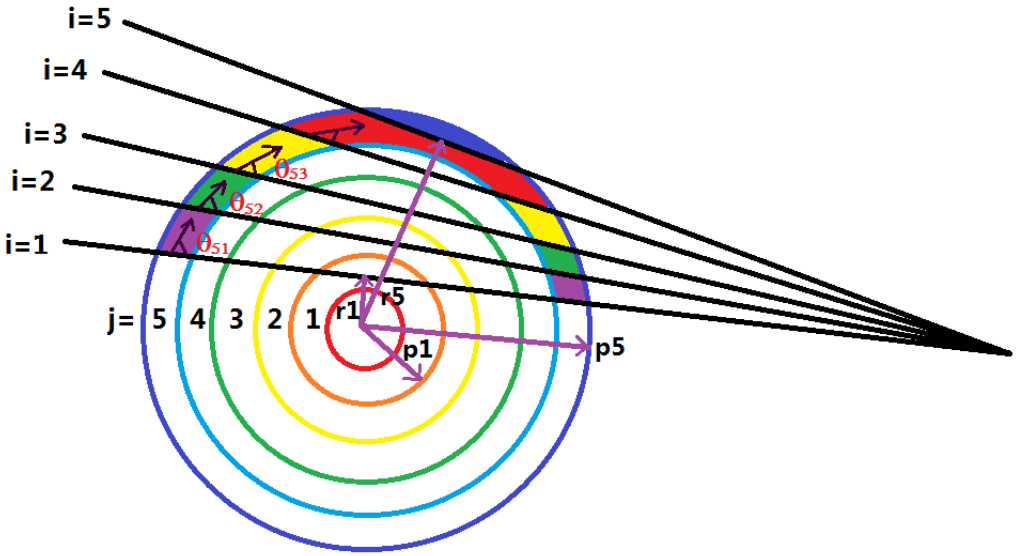

Figure 2-17 Schematics of inversion geometry. The indices i and j represent index of line-of-sight and emitting position.

In order to find the relationship between experimentally measurable parameters and plasma properties, moments of both sides of equation (3.6) are taken about the rest wavelength:

0^{th} moment $M_{0,i} = \int d\lambda (\lambda - \lambda_0)^0 P_i(\lambda) = \sum_j L_{ij} E_j$ (3.7)

1^{st} moment $M_{0,i} = \int d\lambda (\lambda - \lambda_0) P_i(\lambda) = \sum_j L_{ij} E_j \frac{v_j}{c} \cos\theta_{ij}$ (3.8)

2^{nd} moment

$$M_{0,i} = \int d\lambda (\lambda - \lambda_0)^2 P_i(\lambda) = \sum_j L_{ij} E_{ij} \left(\frac{\lambda_0^2 v_j^2}{c^2} \cos^2\theta_{ij} + \frac{\lambda_0^2 T_j}{mc^2}\right) \quad (3.9)$$

The 0th moment equation is a typical tomography problem used to find the emissivity profile from the line-integrated signal. Higher moments (1^{st}, 2^{nd}) contain the spectral shape information such as ion rotation and temperature. By calculating the 0^{th}, 1^{st}, 2^{nd} moment of the measured spectrum, we can relate to the plasma properties. We can consider the moment equations as matrix equations such as $\vec{M} = \mathbf{A} \cdot \vec{x}$ and the problems are an inverse problem to find $\vec{x}$ from the measurements$\vec{M}$. Note that the number of measurements (length of $\vec{M}$) and spatial grids (length of $\vec{x}$**)** are 10 and 70, respectively.

This inverse problem is an example of an ill-posed problem due to a lack of smoothness in the data, solution, and presence of noises. It is heuristically natural because the inversion problem is estimating quantities of nature with a fine spatial grid from the finite measurement. Without any treatment, these methods tend to amplify noise due to the ill-conditioning of the discrete inverse problem. To handle the inverse problem, the

regularization method is utilized to find the solution which is a minimization problem of the cost function. The cost function (F) is

$$F = (\mathbf{A}\cdot\vec{x}-\vec{b})^T(\mathbf{A}\cdot\vec{x}-\vec{b}) + \alpha^2(\mathbf{\Gamma}\cdot\vec{x})^T(\mathbf{\Gamma}\cdot\vec{x})\cdot \tag{3.9}$$

Where $\mathbf{\Gamma}$ is the regularization matrix and α is a regularization parameter. The first term of RHS of equation (3.9) represents the difference (accuracy) between modeled and measured data and the second term is regularization term which has the effect of smoothing the derived radial profile. The regularization parameter is a weighting coefficient of the regularization term. This method can also be sequentially in a similar manner for the higher moment equation in equation (3.8) and (3.9). 2nd derivative matrix with a small boundary value as a boundary condition is chosen for a regularization matrix as following,

$$\mathbf{\Gamma} = \nabla_{\mathbf{x}}^{\mathbf{2}} = \begin{bmatrix} 2 & -1 & & & \\ -1 & 2 & -1 & & \\ & \ddots & \ddots & \ddots & \\ & & -1 & 2 & -1 \\ & & & 0 & 1 \end{bmatrix}. \tag{3.10}$$

If too high regularization coefficient is imposed on the solution, then it will not tract the measured data properly. On the other hand, if too small regularization coefficient is imposed the residual will be good but the solution looks highly oscillating feature. In order to choose the appropriate value of regularization parameters, there are numerous researches to suggest several methods such as discrepancy principle [31], L-curve [32], and GCV [33]. In this research, we use L-curve method to find the optimum regularization parameter which finds an L curve corner in the plot ($\left\|\mathbf{A}\cdot\vec{x}_\lambda-\vec{b}\right\|_2$, $\left\|\mathbf{\Gamma}\cdot\vec{x}_\lambda\right\|_2$) and

corresponding regularization parameter. An example of L curve is shown in Figure 2-18 and typical optimum values are 3 for emissivity inversion (0^{th} moment) and 5 for rotation inversion (1^{st} moment). The inverted emissivity profiles with difference regularization parameters are shown in Figure 2-19. As mentioned before, strong regularization makes an inverted profile become the monotonic profile to maximize the smoothness. On the other hand, a solution with a weak regularization has a very oscillating feature and it is contrary to our prediction for plasma properties which is believed to be continuous. The estimated inverted profile with an optimum regularization parameter looks well-behaved.

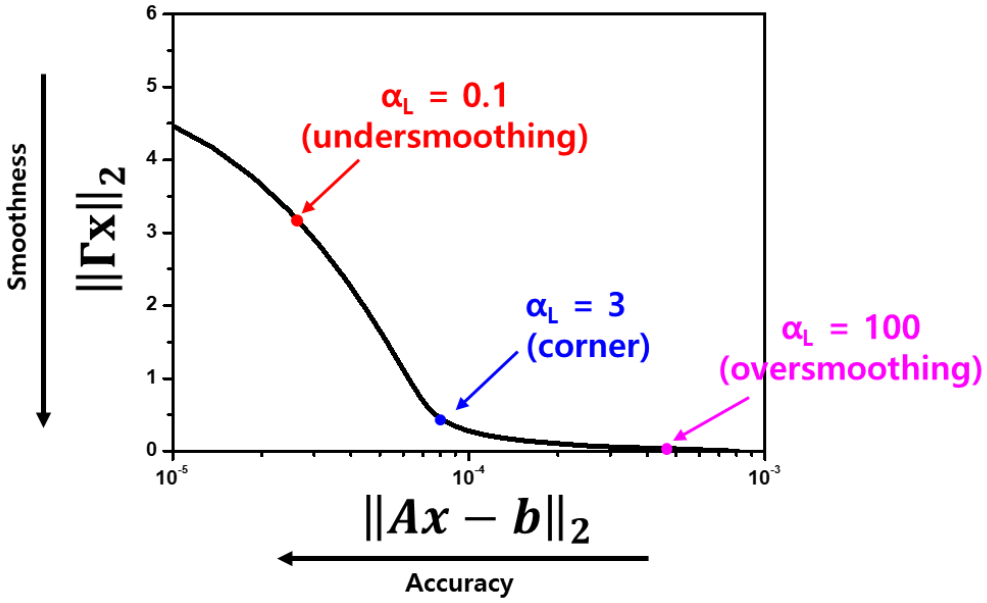

Figure 2-18 Typical L curve plot for emissivity profile inversion. Regularization parameter in the curve corner represents optimum regularization parameter in the L curve method.

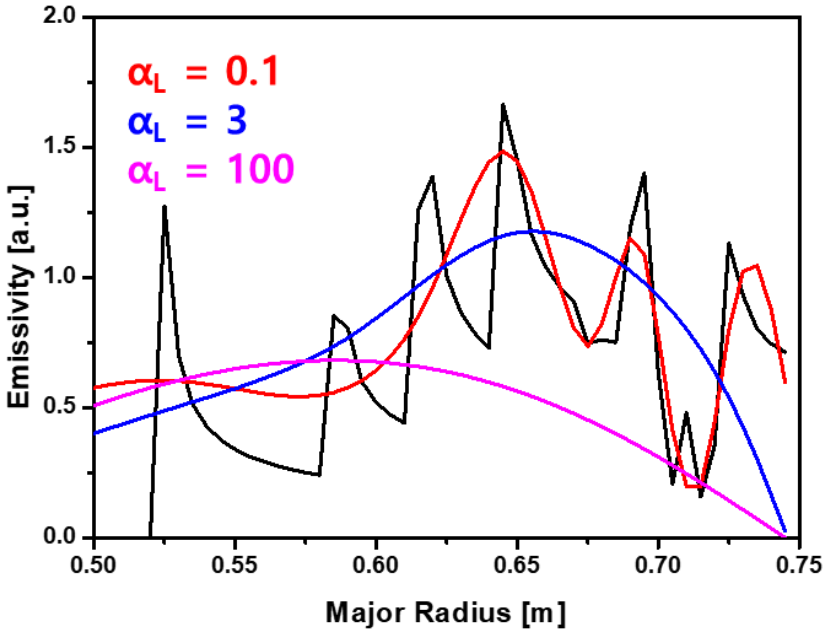

Figure 2-19 Example emissivity profiles from the inversion with different regularization parameters. Too small and too high value of regularization parameter induce undersmoothing (red) and oversmoothing (magenta) result. Inverted emissivity profile from the optimum regularization parameter estimate realistic profile (blue)

2.4.3. Phantom Test for the Doppler Tomography

In this section, we test the Doppler tomography algorithm with a phantom test. The purpose of the phantom test is to validate the Doppler tomography technique and performance of the designed spectroscopic system. With realistic artificial phantom profiles, we estimate the synthetic measured spectra of each spatial channel, conduct the inversion process and then compare the reconstructed profiles with phantom profiles. This process reflects the experimental setup of our spectroscopic system.

The typical emissivity profile of CIII emission of VEST plasma is a hollow profile that has small value at the core and large value near the edge. We assume that the VEST plasma-like emissivity phantom is a hollow shape and other properties (toroidal rotation and ion temperature) are peaked profile (see Figure 2-21 black line).

$$E_j = -E_0(R - R_0 + a)(R - R_0)^2(R - R_0 - a) \tag{3.10}$$

$$v_\phi = v_{\phi 0}(R - R_0 + a)(R - R_0 - a) \tag{3.11}$$

$$T_i = T_{i0}(R - R_0 + a)(R - R_0 - a) \tag{3.12}$$

Where R_0 and a is the major radius and minor radius of the plasma, respectively. The estimated measured spectra are calculated by integrating the spectrum of the local emission with fine spatial grids. Figure 2-20 shows the synthetic measured spectra of CIII emission of each spatial channel. This calculation reflects the real experimental setup of the spectroscopy system such as sightlines of each channel, number of channels, and wavelength resolution.

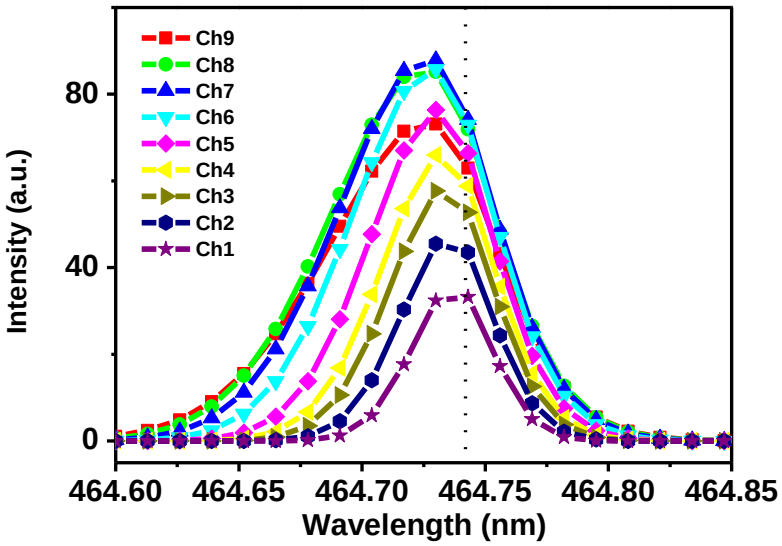

Figure 2-20 Synthetic measured spectra of CIII emission with an installed spectroscopic setup in phantom profiles

By taking a moment of the synthetic spectra, we obtain the apparent (line-integrated) properties as shown in the gray line of Figure 2-21. Without tomographic inversion, the measurement value cannot represent the real properties. In particular, the core properties are screened by strong emission in the intermediate range and the measurement values indicate the emission peak properties. With the tomographic inversion, the reconstructed profiles well described the real profiles except for the extreme edge region. The sensitivity of the noises in the measured spectra is also verified by adding the 5% random Gaussian noises in the spectra. Even in the noisy spectra, the reconstructed profiles (see red curve in Figure 2-21) are well-matched to real phantom profile. By adopting the regularization technique, we successfully reduced noise sensitivity.

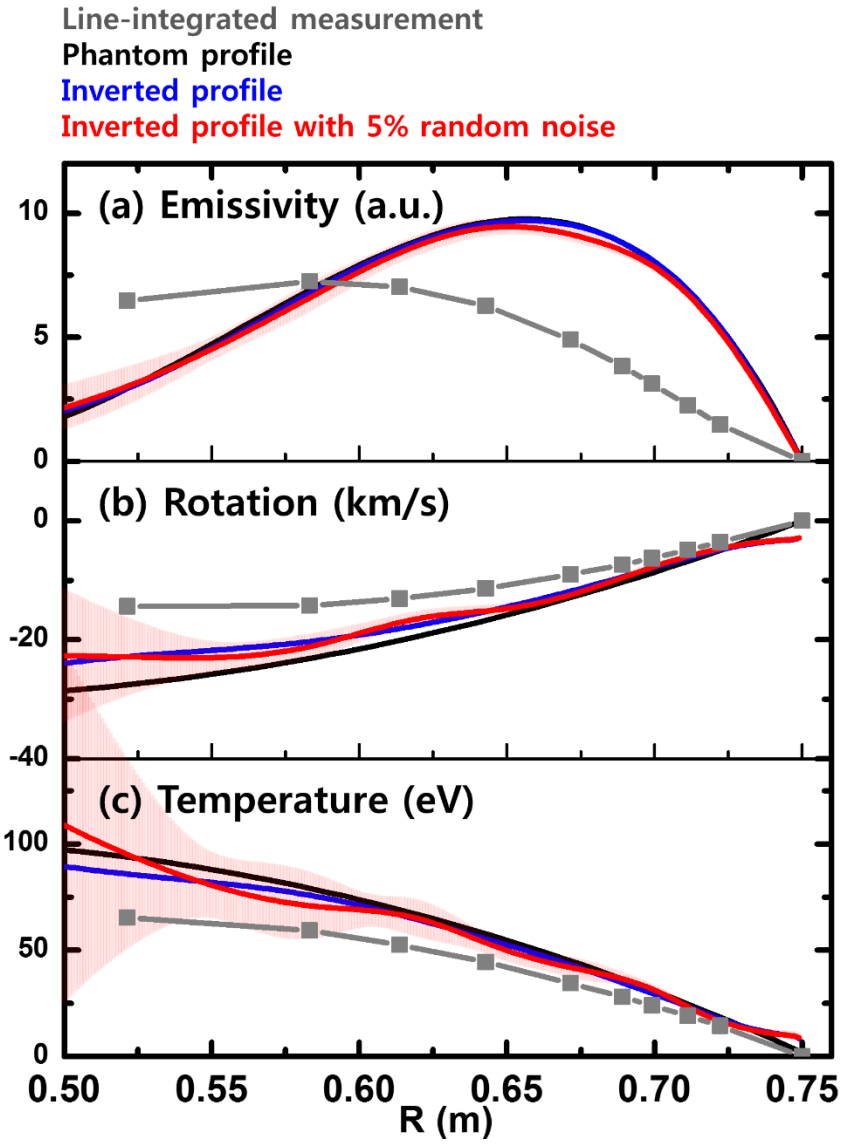

Figure 2-21 Phantom test result. Line-integrated measurement in gray line, Phantom profile in black, tomographic inverted profile without noise in blue, and tomographic inverted profile with 5% noise in red. (a) Emissivity profile (b) Rotation profile (c) ion temperature profile.

The exact knowledge of boundary condition is very important in the tomography problem. In the real case, the plasma position is not fixed and sometimes move inward or outward. However, it is very hard to measure the exact boundary values because the signal to noise ratio near the boundary is bad. The farthest position of installed line-of-sight is R=0.704 m and a typical plasma boundary is set to R=0.75 m. We usually impose the boundary condition as zero values of emissivity, toroidal rotation, and ion temperature at the R=0.75. Sensitivity test of the boundary condition is conducted with different boundary position. The boundary position of the phantom profile is R=0.75 m. Three different boundary condition is tested with R=0.73, 0.75, 0.77 m as shown in Figure 2-22. If the boundary condition is set the inner position than a real boundary, the error is significant in the edge region of emissivity and the error propagates to the core region as shown in rotation and temperature profile. On the other hand, even if the boundary condition is farther than the actual boundary, the reconstructed profile is still good agreement to the phantom profile. Based on the sensitivity test of the boundary condition in tomographic problem, we conclude that the boundary condition is very sensitive to the reconstructed result and the boundary condition should be set to the farther than the actual boundary.

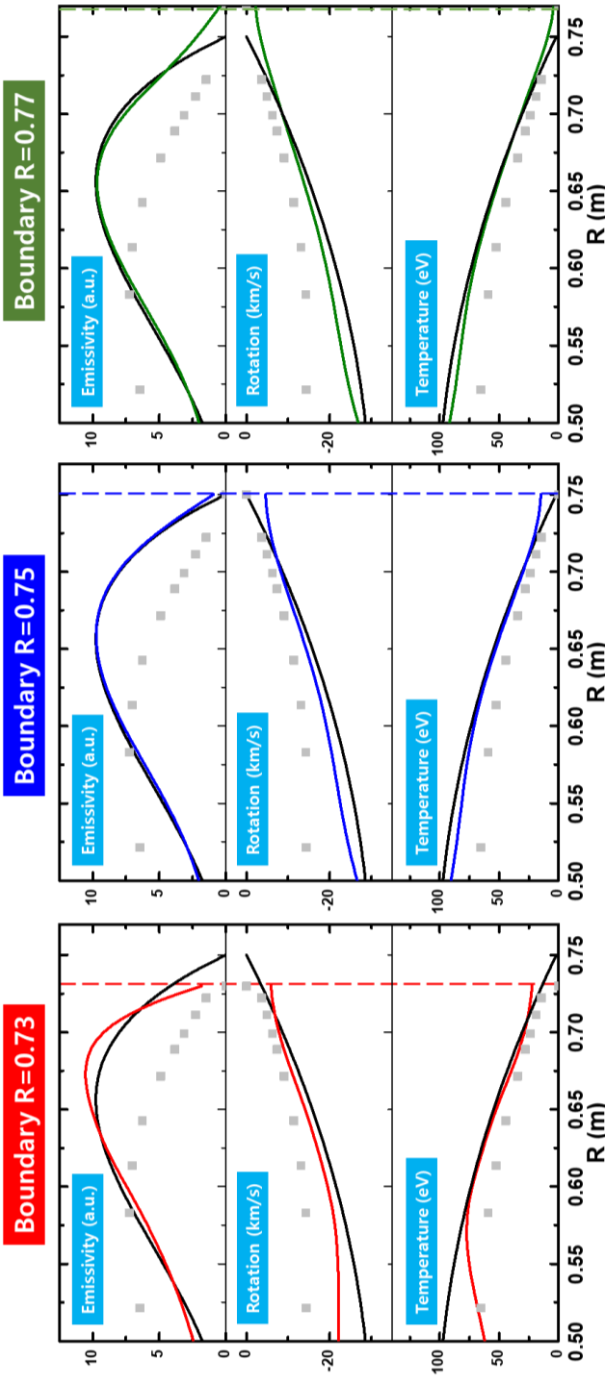

Figure 2-22 Sensitivity test of boundary condition in Doppler tomography.

2.4.4. Quantification of Uncertainty

Quantifying uncertainty is a critical part in tomographic reconstruction problem. An ill-conditioned feature in the inverse problem is amplifying the noises in the reconstructed results. However, the direct uncertainty calculation is very complex in the tomographic problem due to the regularization process. Therefore, we employ the numerical approach to consider the propagation of uncertainties using the Monte-Carlo method and the detailed methodology is described in this section.

The quantification of uncertainty of the Doppler tomography method is done by considering the spectrum fitting error. These uncertainties contain random noises such as photon statistics (shot noise) and thermal noises of a detector. But there are still other sources of uncertainty from the systematic errors. The systematic errors in the hardware setup consist of misalignments of line-of-sight, mechanical or thermal drift of optical components and imperfect calibrations. Also, Doppler tomographic technique has ingredients of systematic error which are the number of the radial grids, choices of regularization parameters and boundary condition. In this section, we consider the random noises as a dominant noise source and estimate the degree of uncertainties by calculating the propagation of fitting errors.

The ten free parameters are inferred by fitting the measured spectra with a model function of combinations of five Gaussian function as described in Section 2.4.1. With asymptotic normal distribution approximation, the confidence intervals for the estimated free parameters with 68% confidence are,

$$\left|\theta_j - \hat{\theta}_j\right| \le s\sqrt{\left(\boldsymbol{J}(\hat{\boldsymbol{\theta}})^T \boldsymbol{J}(\hat{\boldsymbol{\theta}})\right)^{-1}_{jj}}\, t\left(N-P;\frac{0.68}{2}\right). \quad (3.13)$$

Where

$\theta = [I_{cont}, I_{CIII-1}, I_{CIII-2}, I_{CIII-3}, I_{OII-1}, I_{OII-2}, FWHM_{CIII}, FWHM_{OII}, \Delta\lambda_{CIII}, \Delta\lambda_{OII}]$

$\boldsymbol{J}(\hat{\boldsymbol{\theta}}) = \partial(f_1, \ldots, f_N)/\partial(\theta_1, \ldots, \theta_P)$: Jacobian matrix

$s^2 = \sum\left(y_i - f(\boldsymbol{\lambda}_i, \hat{\theta})\right)^2/(N-P)$: Standard deviation

$f(\boldsymbol{\lambda}, \boldsymbol{\theta})$: model function with coefficient θ, data $\boldsymbol{\lambda}$

$t\left(N-P;\frac{0.68}{2}\right)$: t-distribution with degree of freedom N − P

N: # of data point= 52

P: # of free parameters =10

For the numerical MC analysis, random Gaussian samplings of estimated fitted parameters are conducted. There are ten line-of-sight measurements and each spectrum measurement has intensity, spectral width (FWHM), and spectral shift. Total 30 Gaussian samplings of parameters is done for each iteration. Then, tomographic inversion is processed with sampled parameters and we collect the processed quantities. These iterations are continued until convergence of standard deviation of collected quantities. The standard deviations of collected quantities are used for the uncertainty as shown in Figure 2-23. The number of iteration is typically 3000 based on the convergence test result in Figure 2-24.

The typical errors of the fitting parameters are quite small and it is independent

of the measurement position as shown in Figure 2-25. The yypical error is 2% for brightness and 5% for ion temperature. However, Figure 2-26 shows that the uncertainty of reconstruction result from Doppler tomography is very sensitive to the spatial position. The error of emissivity is 1% in the edge and increases up to 15% at the R=0.5 m. The error of ion temperature is 3% in the edge and 35% at the R=0.5 m. It is natural to have a large error in the core parameter because the core result is strongly influenced by not only the core measurement but also the edge measurement. This result indicates the IDS measurement is good enough for the edge and intermediate measurement for VEST. However, in order to measure the core property accurately, other diagnostic techniques such as CES (Charge exchange spectroscopy) should be taken into account in the future [36].

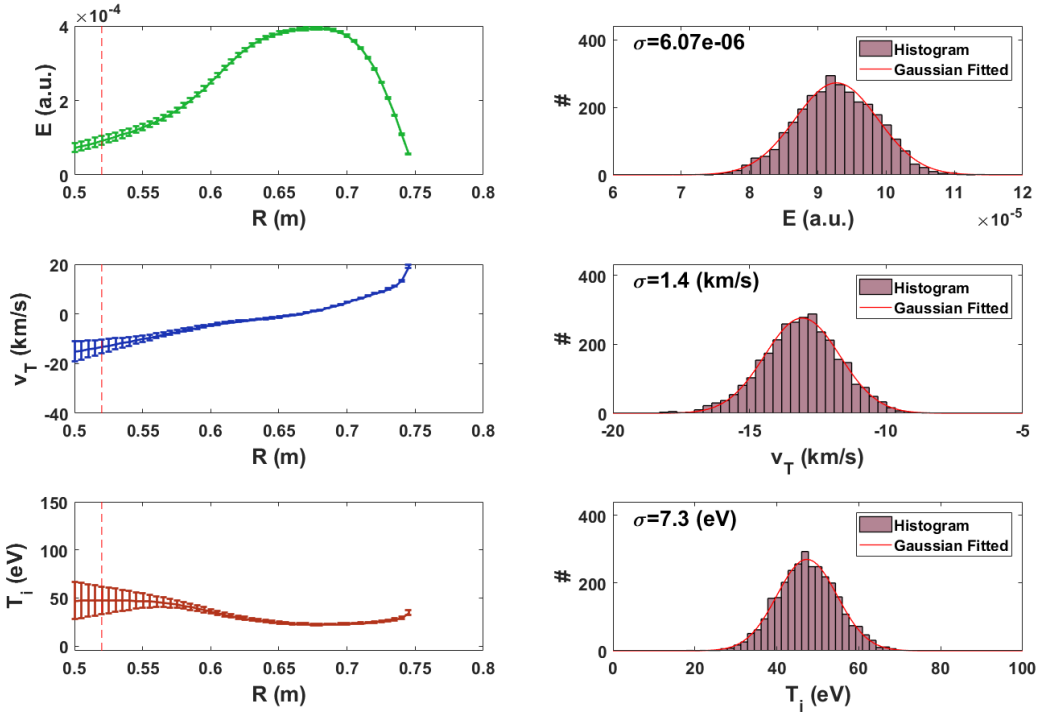

Figure 2-23 Inverted profiles and data histogram at R=0.52 m. (Top) Inverted emission profiles (middle) Inverted toroidal rotation profile (bottom) Inverted ion temperature profile.

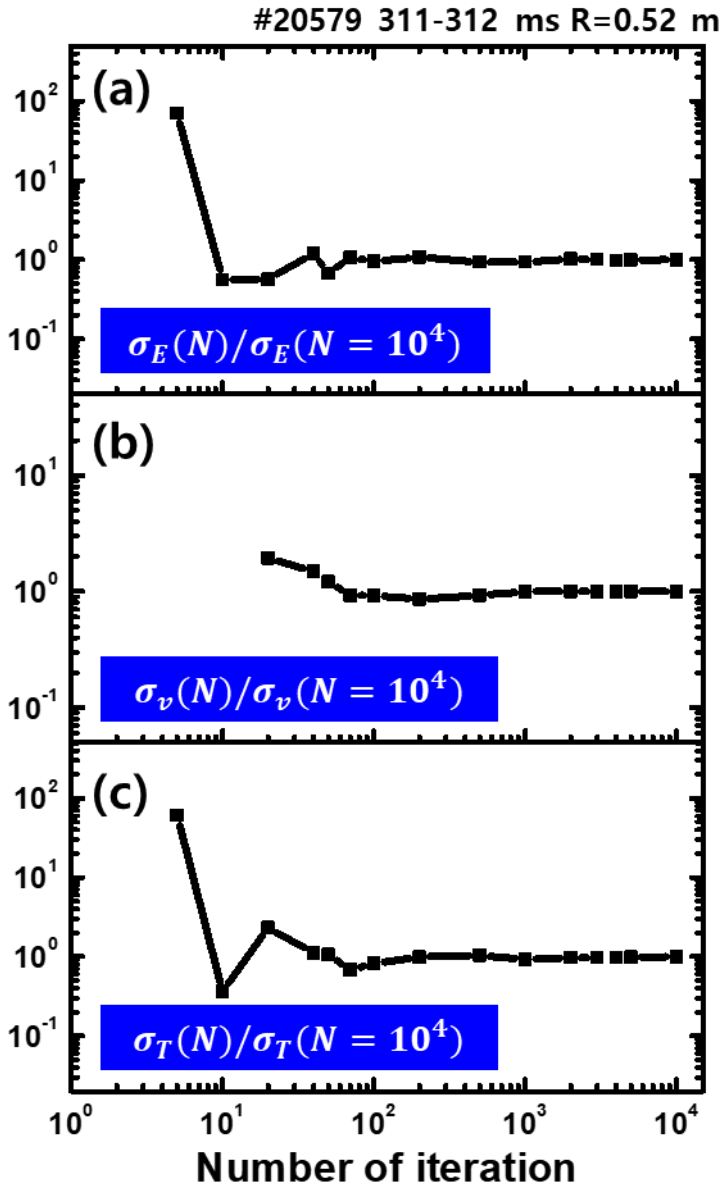

Figure 2-24 The standard deviation with the number of iteration normalized to the standard deviation with 10^4 iterations (a) emissivity inversion (b) rotation inversion (c) ion temperature inversion.

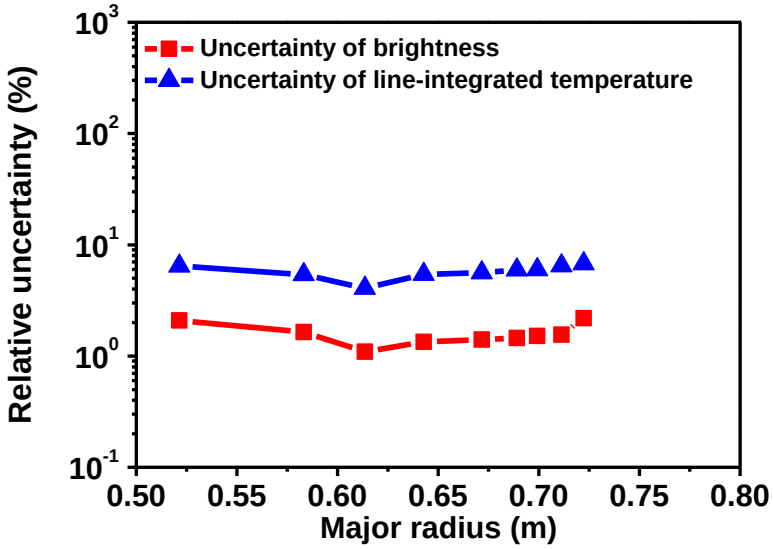

Figure 2-25 Typical error of Line-integrated measurement. Uncertainty of brightness (red) and Uncertainty of temperature (blue)

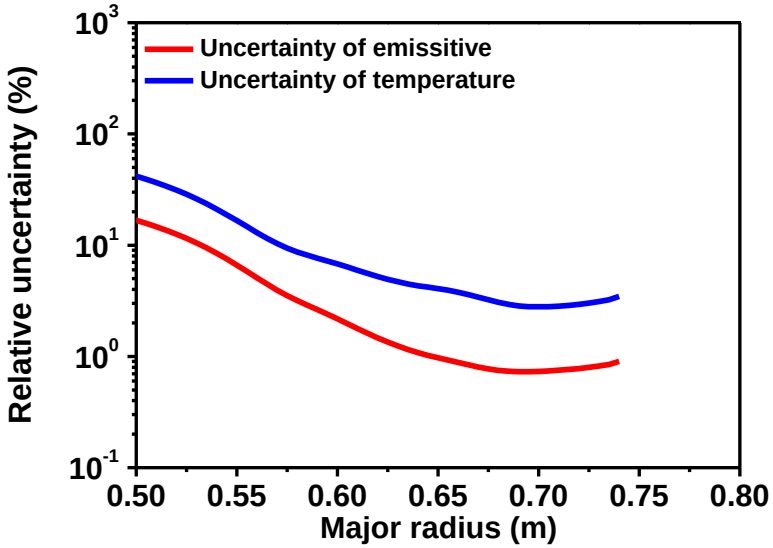

Figure 2-26 Typical error profile calculated by MC method. Emissivity error profile (red) and ion temperature error profile (blue).

Chapter 3. Bursting MHD Events on VEST

There are two kinds of MHD instabilities in Ohmic discharge in VEST: Tearing modes (NTMs) and bursting MHD events. Sometimes, these instabilities are very severe and trigger the minor disruption called IRE (Internal reconnection event) in the spherical torus. They have a similarity in discharge parameters change but differencesin evolution of MHD precursor, growth rate, and effect on plasma rotation. In this chapter, we investigate the characteristics of these two instabilities and their effects on plasma rotation.

3.1. Tearing modes (TMs) on VEST

3.1.1. Characteristics of TMs on VEST

A tearing mode (TM) is a non-ideal MHD plasma instability. The ‘classical’ TM is a current-driven instability, which is accompanied by magnetic reconnection. It can occur when the local resistivity is sufficiently high and the excess free energy is dissipated by the reconnection process forming the magnetic island. The ‘neoclassical’ TM occurs when significant pressure-driven bootstrap current is expected but is not present due to the enhanced heat diffusion at a rational surface. This island flattens the pressure profile, reduces the bootstrap current and reinforce the initial perturbation. The helical current perturbation lies in the magnetic field line with mode number (m, n), where m is the poloidal mode number and n is the toroidal mode number.

The magnetic islands cause many problems in tokamak operation such as limitation of plasma performance and failure of plasma start-up. One well-known effect

of the magnetic island is degradation of confinement. Transport of particles and heats along the magnetic field lines is very fast compared to the perpendicular direction to the field. When the island is formed as shown in Figure 3-1, the field lines at the separatrix connect across the radial region spanned by the island width, allowing fast parallel transport in the radial direction. As a result, the density and temperature become flatted out across the radial extent of the island. This model is known as the ‘belt model’ [34].

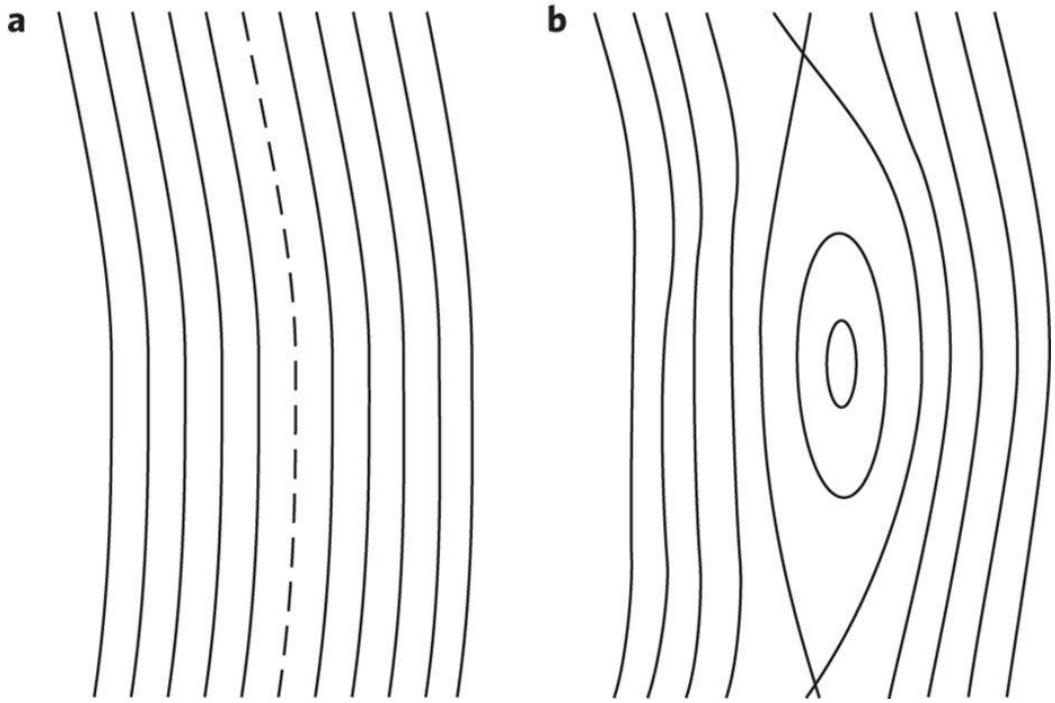

Figure 3-1 Equilibrium field line and magnetic island [35]. (a) Unperturbed magnetic surface (b) A magnetic island has grown around a rational field line.

TM instability could be excited especially in fast plasma current ramp-up [36, 37, 38]. This TM limits the current grow-up and leads to premature discharge termination. In the VEST device, the onset condition control is investigated by adjusting current ramp up rate and the prefill gas pressure. The details result can be found in [38].

The typical tearing mode discharge observed in VEST is shown in Figure 3-2. Initially, two distinct mode with (m, n) = (2, 1) and (3, 2) are mutually excited at 0.306 s and then changed to the (3, 1) and (4, 2) subsequently. During the tearing mode activities, the mode frequencies keep decreasing from 15 kHz to a few kHz. The amplitude of the instabilities grows in several milliseconds, which is comparable to the resistive diffusion time scale ($\tau_R \sim 2\ ms$).

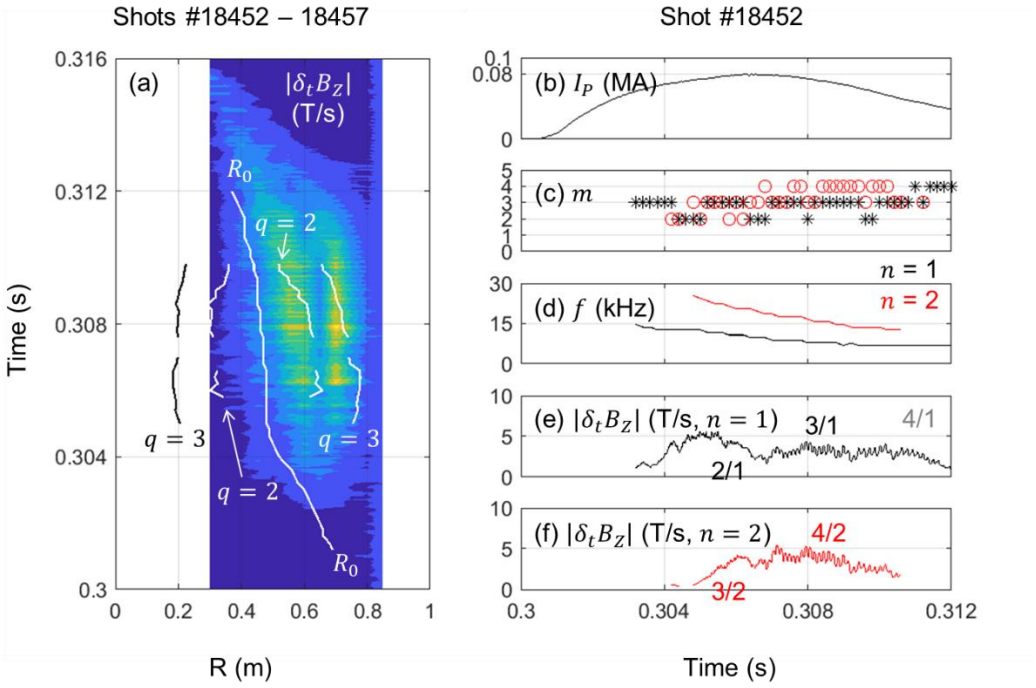

Figure 3-2 Typical evolution of tearing mode on VEST [38]. (a) The internal magnetic probe measurement of the radial profile of averaged $|dB_z/dt|$ during the identical shots from #18452 to #18457. (b) Plasma current. (c) Mode characteristics.

3.1.2. Locking Bifurcation

A notable feature of the tearing mode is the existence of a forbidden band of mode rotation frequency. As the magnetic island grows, the mode frequency continuously decrease, suddenly drop to below 1 kHz and lock to the wall. The non-rotating TM with respect to the lab frame is called locked mode (LM). This LMs can perturb global plasma stability and cause disruption in many tokamak plasmas [39, 40, 41].

The tearing mode locking bifurcation can be interpreted by the momentum balance equation between restoring viscous force and drag force by the wall. The simple model can be expressed as following [42],

$$I\frac{d\omega}{dt} = \beta(\omega_0 - \omega) - \gamma W^4 \frac{\omega\tau_w}{1 + (\omega\tau_w)^2} \tag{3.1}$$

Where I is the moment of inertia of the plasma, ω is the angular frequency of the mode, ω_0 is the natural angular frequency of the mode, W is the mode island width β and γ are coupling coefficient that depends on geometry and plasma condition. τ_w is the effective wall time constant ($\tau_w = [1 - (r_s/r_w)^{2m}]\mu_0\sigma r_w\delta/2m$). Here, r_w is the effective radius, conductivity and thickness of the wall and r_s is the radius of the mode rational surface. The term on the left represents the inertia of the plasma, the first term on the right shows the viscous restoring force from the plasma, and the second term on the right is the wall drag force.

Now, we consider the steady state solution by neglecting LHS of equation (3.1) and rearrange the equation in terms of dimensionless variable as following,

$$(x_0 - x) = a\frac{x}{1+x^2}. \quad (3.2)$$

Where $a = \gamma W^4 \tau_w/\beta$ is the normalized mode amplitude, $x = \omega\tau_w$ is the normalized mode frequency and $x_0 = \omega_0\tau_w$ is the normalized natural mode frequency. The x_0 can be measured directly when the amplitude of the tearing mode is small. In VEST condition, its value is around a hundred ($\omega_0 = 2\pi$f~60 kHz).

When x_0 is less than $x_{0,crit} = 3\sqrt{3}$, the equation (3.2) has only one real solution regardless of mode amplitude. In this case, the mode frequency is continuously decreasing without frequency bifurcation as seen in Figure 3-3 (a). However, when x_0 is greater than $x_{0,crit}$, there can be a three real root with two stable roots in low and high frequency and unstable root in intermediate frequency. As mode amplitude increases, initially rotating mode in (point 1) in Figure 3-3 (b) is continuously slowing down and suddenly drops to the low frequency solution in (point 5) in Figure 3-3 (b). We can clearly see the existence of the forbidden frequency band and this can explain the locking bifurcation. Conversely, Figure 3-3 (c) shows the rotation recovery process when mode amplitude decrease. In order to unlock the LM, the island width should be reduced in various methods such as external current drive [43] or island crash event.

During the tearing mode activity on VEST, the rotation bifurcation is frequently observed as shown in Figure 3-4. The initial rotation plasma with around 10 km/s in counter-current direction suddenly drops to nearly zero as tearing mode grow up. The LM induce the minor disruption event called IRE (internal reconnection event). After IRE, the plasma rotation somewhat recovers due to reducing the magnetic island width.

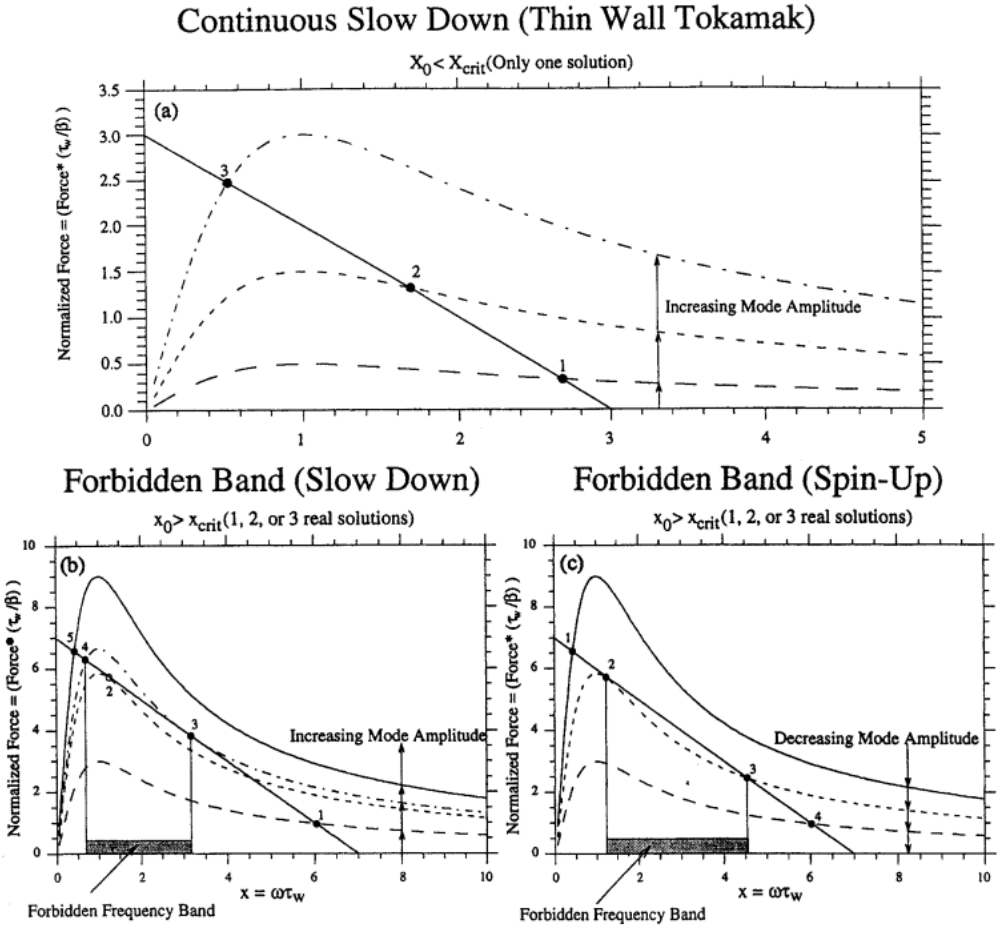

Figure 3-3 Graphical description of the interaction between restoring viscous force and resistive wall force. (a) When normalized natural mode frequency (x_0) is less than the critical value $x_{0,crit}$ (b) when x_0 is greater than $x_{0,crit}$ and the mode amplitude is growing. There is a forbidden frequency band. The high frequency root is bifurcated to the low frequency root at certain mode amplitude (c) when x_0 is greater than $x_{0,crit}$ and the mode amplitude is decreasing.

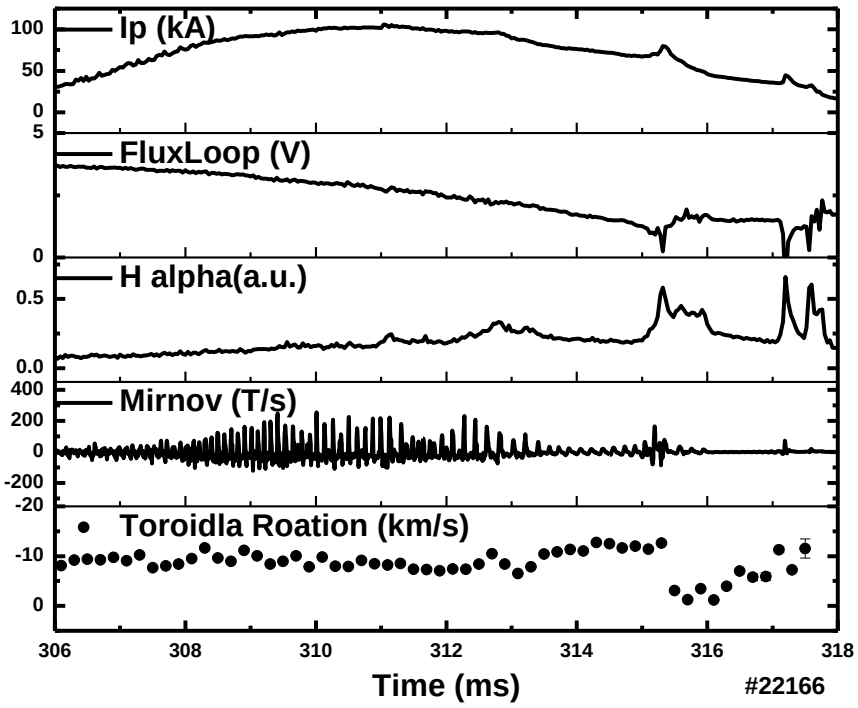

Figure 3-4 Discharge parameter evolution during tearing mode activity. Initially rotating plasma is suddenly lock to the wall (locking bifurcation) and internal reconnection event occur.

3.2. Bursting MHD Events on VEST

3.2.1. Characteristics of Bursting MHD Events on VEST

There are other kinds of instability observed in VEST discharge: bursting MHD event. Figure 3-5 shows the time evolution of the discharge parameters in bursting MHD activity in the VEST device. This activity is usually observed in relatively low-density plasma in the absence of tearing mode. These events are characterized by a spike in the plasma current, loop voltage and the burst of magnetic fluctuations with a high frequency above 10 kHz as shown in Figure 3-6. The spike in plasma current and loop voltage indicates the internal magnetic reconnection. Internal reconnection makes the plasma current profile flattened and reduces the internal inductance which results in current and loop voltage spike. The typical current spike ($\Delta I_p/I_p$) can be up to 15%. An increase in Hα signal shows wall-interaction during the activity and some part of confinement loss (particle and heat) is accompanied. Magnetic fluctuation shows a very fast exponential growth within a typical time constant of tens of microsecond (<100τ_A, τ_A: Alfven time scale =R/v_A) compared to current diffusion timescale (~ms). The broadband frequency spectrum is observed at the time of bursting MHD and disappears within 1 ms. It is hard to identify the exact mode number due to the very short lifetime and limited sampling rate of Mirnov coils but we presume the dominant mode number is (m, n) = (3, 1) or (2, 1) and (1, 1) based on the phase analysis of Mirnov sensors. Plasma current usually is sustained after the activities with the small and moderate strength as seen in Figure 3-5. Sometimes, significant loss of plasma current is often observed as shown in Figure 3-7 and finally, the

discharge is terminated. The events usually occur at ramp down phase and sometimes sawtooth come before the crash activity. The prefill gas pressure, plasma shape(elongation and radial position), and wall condition are believed to key operating parameters in the MHD onset. Further research is needed to characterize the activity and its relation. The clear rotation increase at the activity is shown Figure 3-5 rather than rotation decrease in tearing mode as shown in Figure 3-4. The detail explanation of the spin-up phenomenon is discussed in Chapter 4.

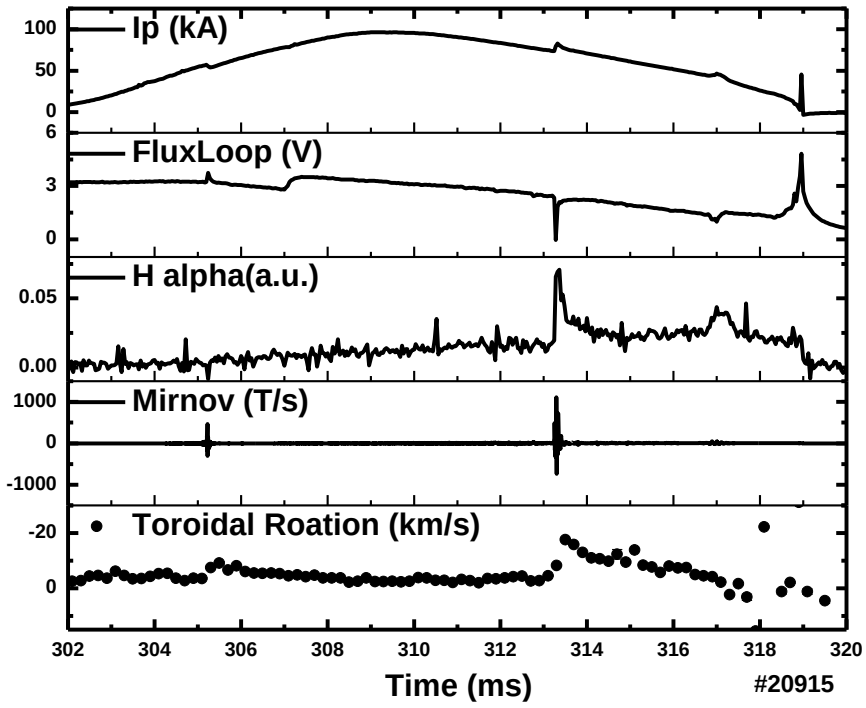

Figure 3-5 Bursting MHD activity in low-*q* Ohmic discharge # 20915. Bursting MHD activity occurs at 313.4 ms and a sudden spin-up of rotation in counter-*Ip* direction.

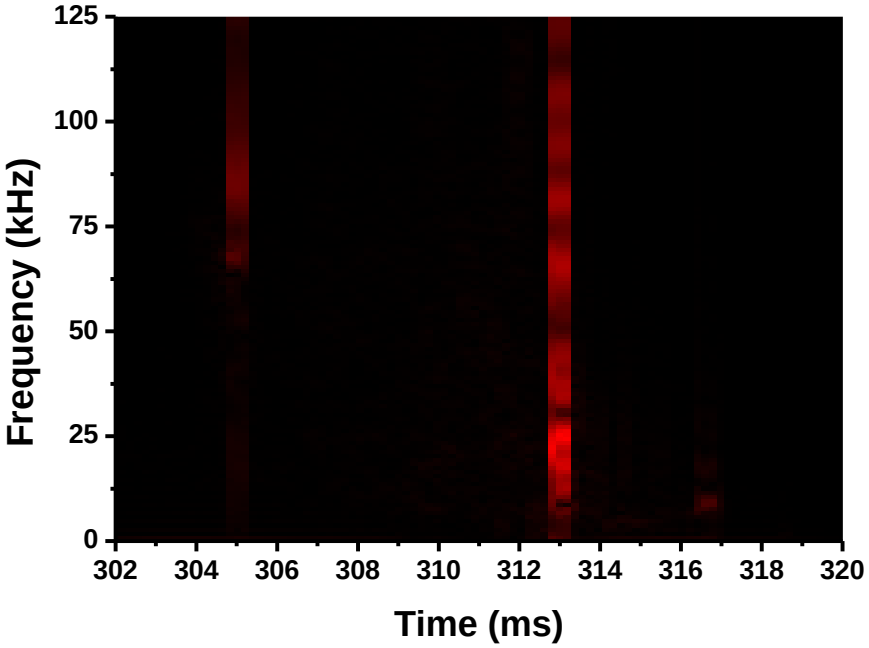

Figure 3-6 Short-time Fourier Transform (STFT) result of Mirnov coil signal installed in outboard midplane in # 20915. The broadband frequency spectrum is observed in bursting MHD activity at ~312.3 ms.

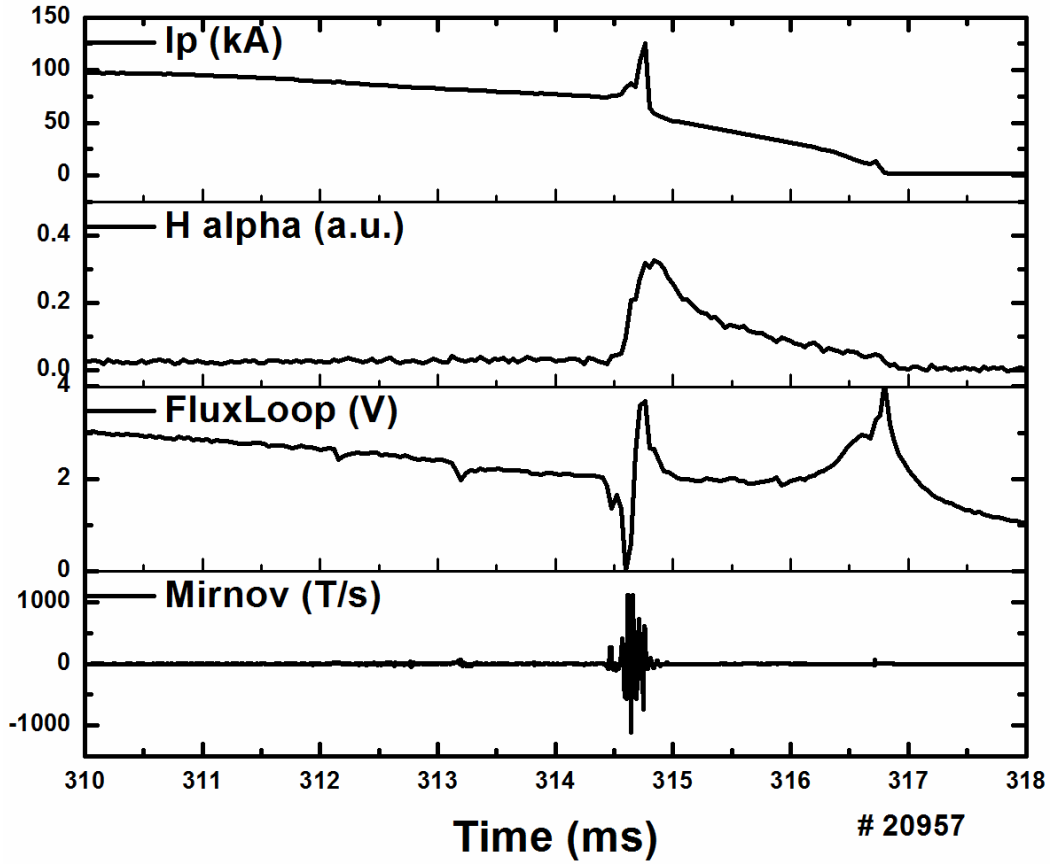

Figure 3-7 Catastrophic bursting MHD at ~ 314.5 ms in # 20957. Significant loss of plasma current is accompanied and finally, discharge is terminated.

3.2.2. Comparison to the Tearing Mode

The temporal evolution of discharge properties of bursting MHD instability is quite different from that of tearing mode as shown in Figure 3-8. In the typical tearing mode discharge, the oscillating magnetic island is born and slowly grows within a few ms. However, in the bursting MHD event, there is no distinct oscillating magnetic precursor to the instability onset and suddenly grow within tens of microseconds (see Figure 3-9). The exponential growth time correspond to ~$30\tau_A$ and is much greater than the resistive diffusion time ($\tau_R \sim 2ms$). This fast growth rate may suggest the ideal character instability such as kink or interchange instability instead of tearing mode.

The major difference in the operating parameter is prefill gas pressure as shown in H alpha signal in Figure 3-8. In the discharge with bursting MHD event, a small amount of prefill gas is injected and result in weak H alpha signal. In this operating condition, high electron temperature may be expected in low plasma density with similar Ohmic power (similar in loop voltage and plasma current). High conductivity of plasma may prevent the magnetic island formation from reconnecting the magnetic flux surface and destabilize the parity instability. Also, there is no indication of the island since the usual mode locking dynamics are not present. For the clear identification of bursting MHD instability, stability analysis will be done with an accurate equilibrium profile. Also, internal property diagnostics such as SXR tomography and an internal magnetic probe will help to classify the instability by analyzing the spatial structure.

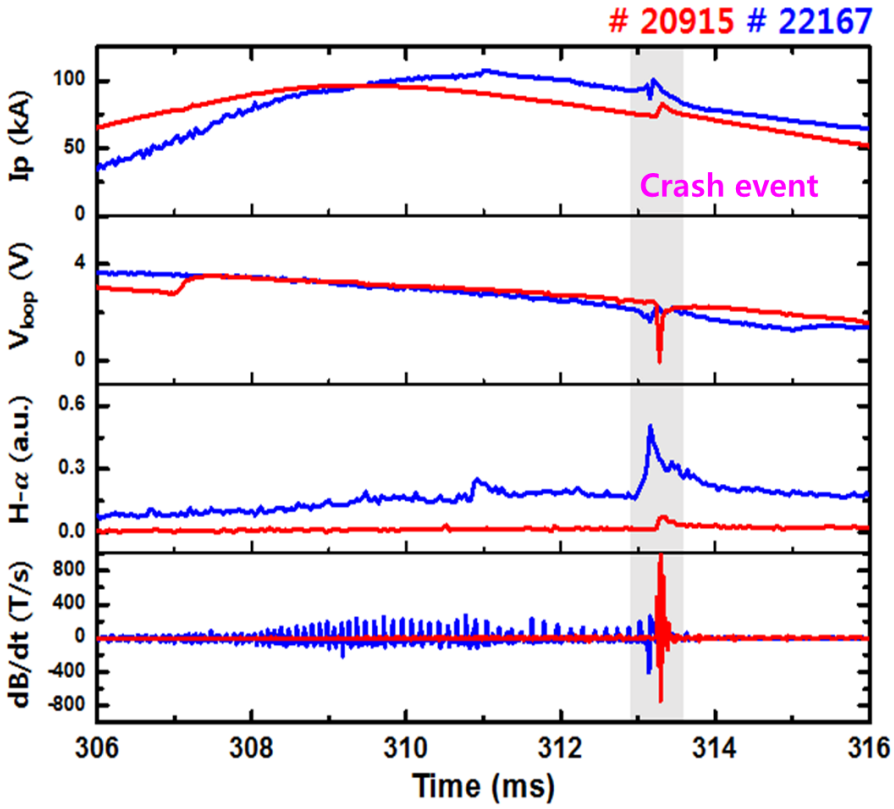

Figure 3-8 Comparison between bursting MHD event and tearing mode. Temporal evolution of plasma current, loop voltage, H alpha intensity, and Mirnov coil signal. (Red) bursting MHD event (Blue) tearing mode.

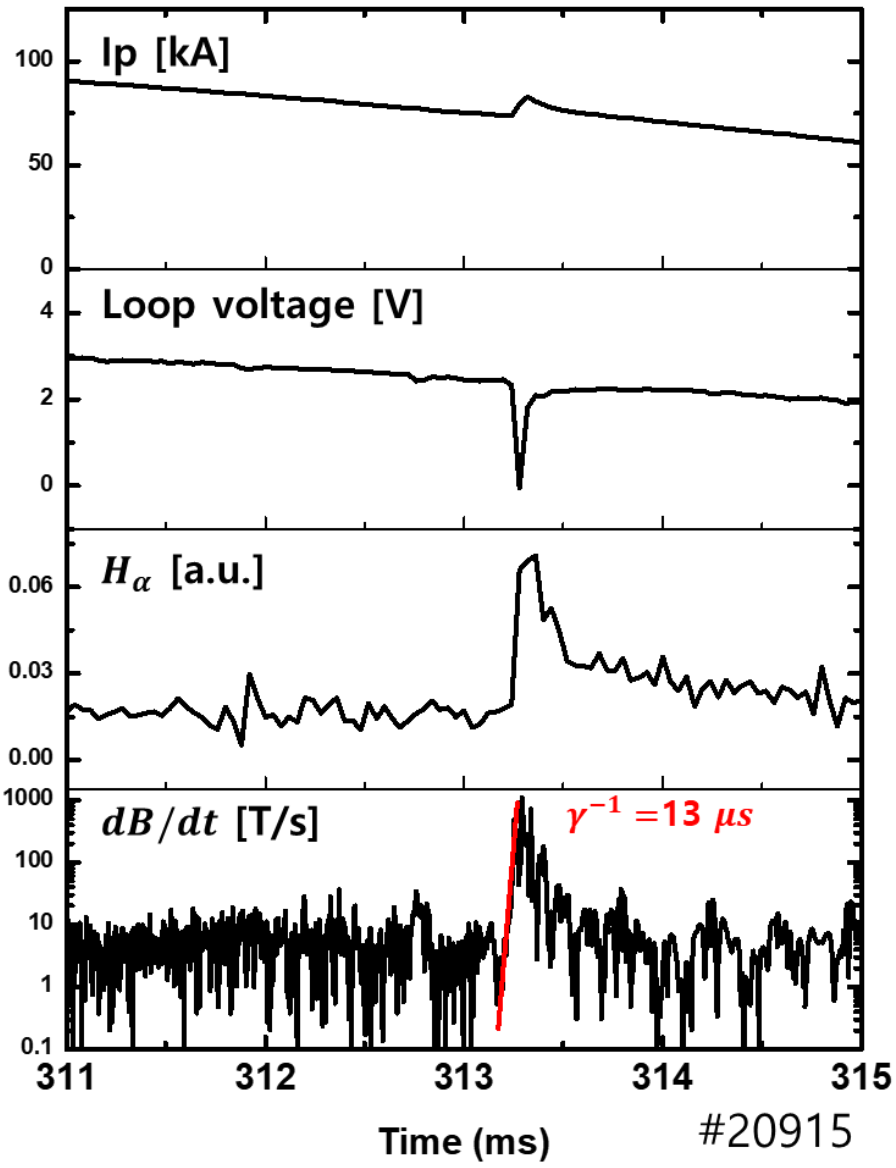

Figure 3-9 Temporal evolution of plasma current, loop voltage, H alpha intensity, and Mirnov coil signal before/after bursting MHD activity in #20915. The Mirnov coil signal shows the fast growth time with 13 μs(~30τ_A) compared to the resistive diffusion time (τ_R~2 ms).

Chapter 4. Ion Heating and Torque from Bursting MHD Events

MHD activity has been observed to affect plasma transport. In particular, sudden transport induce the profile relaxation of particle density, heat, and current in a short time which are different from the transport by micro turbulence. In this manner, there is no reason to expect that momentum transport would be an exception compared to particle and energy. Also, the complex influence of MHD activity on plasma parameter and equilibrium can contribute the potential momentum sink or source. Nevertheless, the effects of MHD activity on the plasma rotation are barely investigated. In our observation, the influence of the MHD activity on plasma rotation is strong and can dominate the rotation profile. We focused on one specific MHD activity: bursting MHD activity which accompany strong impulsive magnetic reconnection phenomena. In this chapter, detail ion rotation dynamics as well as ion temperature are experimentally investigated and compared with characteristics of possible several physical mechanisms.

4.1. Spatio-temporal Behavior of Plasma Rotation and Ion Temperature during Bursting MHD Events

In order to observe the changes of ion properties in the MHD phenomenon, two measurement options described in Chapter 2 were performed: profile measurement with 1ms and 10 spatial channel, fast measurement with 0.2 ms and 1 spatial channel. Since the MHD crash event occurs within ~ 0.3 ms and the changed profile can last for a confinement time (~1 ms for VEST), the profile measurement with 1ms temporal resolution can sufficiently capture the profile variation before and after the event. Fast measurement with 0.2 ms temporal resolution is useful to confirm the detailed time dynamics. These two diagnostic option can be replaced in shot by shot, we select the two similar shot # 20579 and # 20915 which have similar plasma evolution and similar MHD crash amplitude as seen in Figure 4-1. Ion property profile is investigated in #20579 and fast temporal behavior is studied in # 20915.

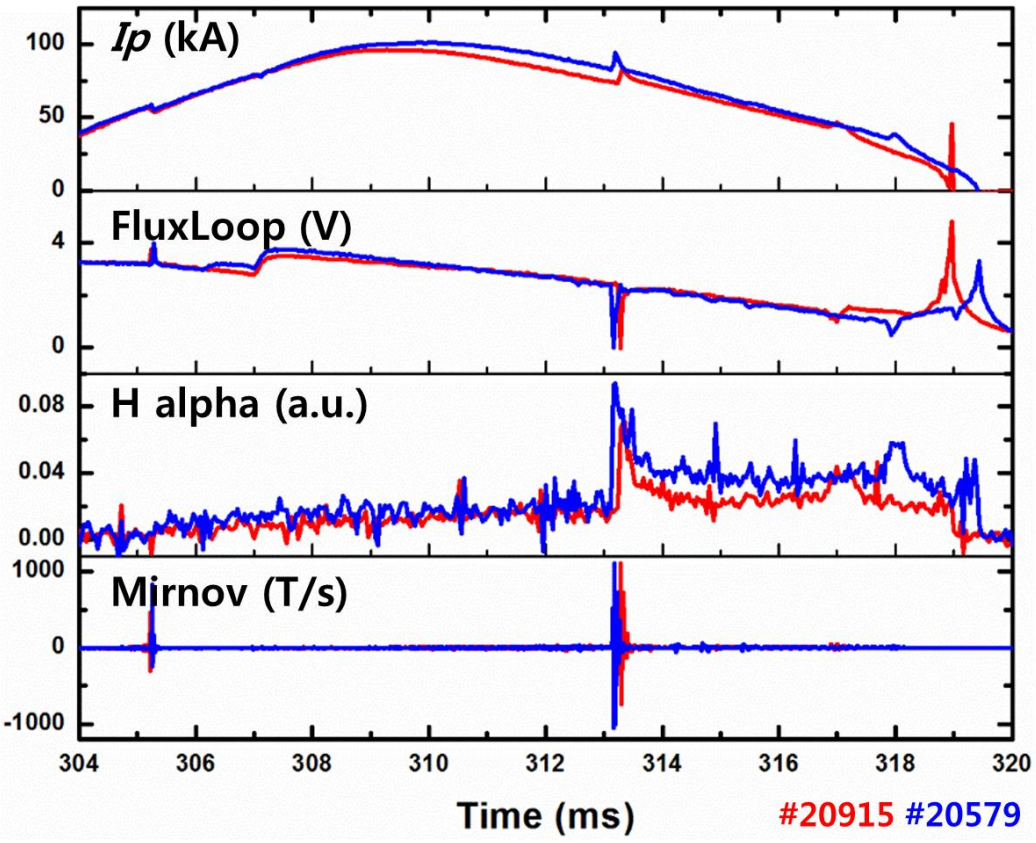

Figure 4-1 Temporal evolution of reference shot (# 20915 and #20579). They have similarities in plasma current, flux loop, H alpha intensity, and Mirnov signal.

4.1.1. Spatial Profile Variation of Rotation and Ion Temperature

The temporal evolution of the discharge parameter and measured raw spectra (line integrated) with 1 ms temporal resolution are shown in Figure 4-2, Figure 4-3, respectively. The measured spectra are dramatically changed after the MHD event. The increase in CIII emission intensity indicates carbon impurities are injected into the plasma as a result of MHD crash. There are significant changes in line shift and broadening which means changes in toroidal rotation and ion temperature, respectively. The temporal evolutions of profiles are shown in Figure 4-4 and Figure 4-5 by tomographic inversion process described in section 2.4.

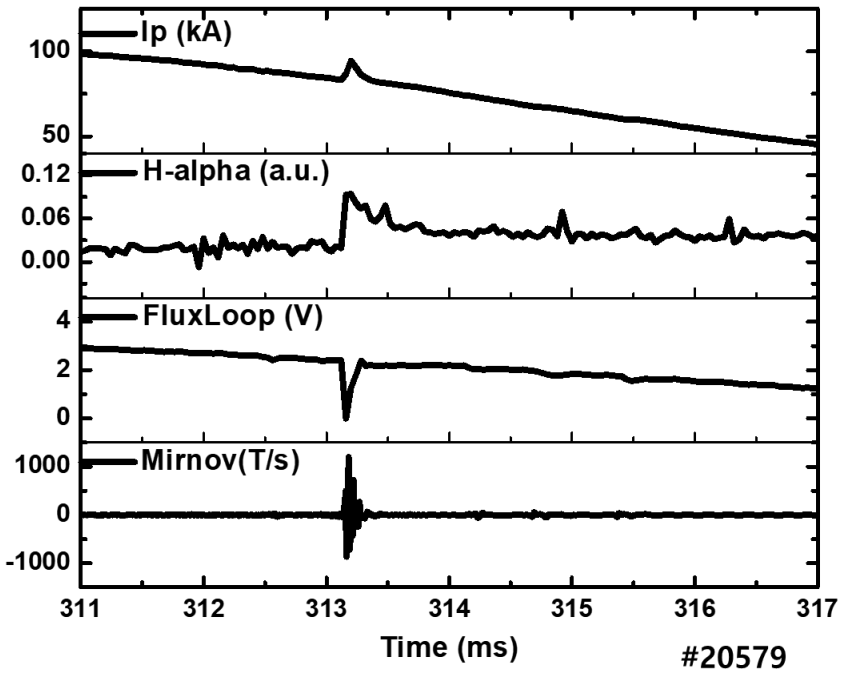

Figure 4-2 Discharge waveform of # 20579. The bursting MHD activity occur at 313.2 ms.

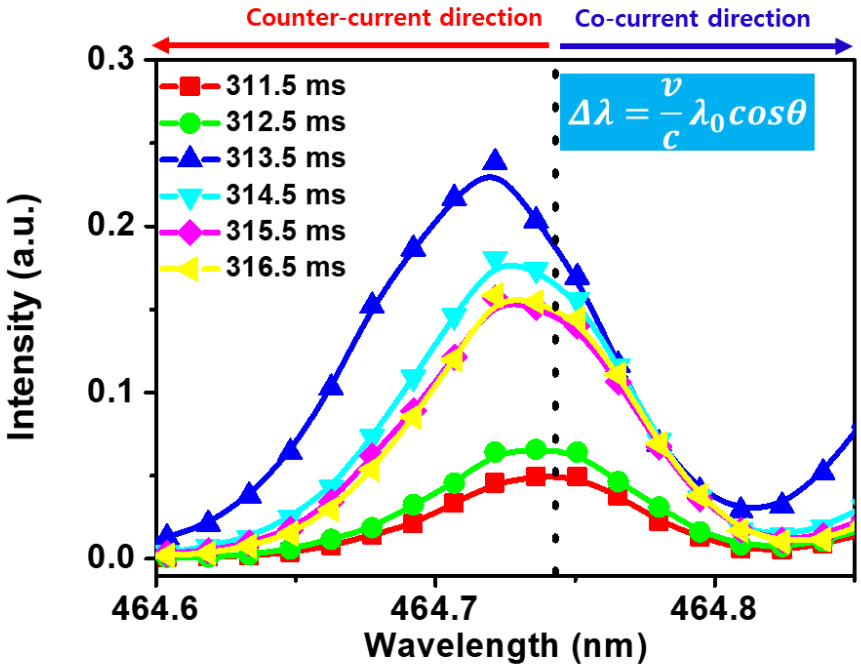

Figure 4-3 Raw line-integrated CIII spectra with the core channel (#9) in #20579. The integration time is 1ms and the time stamp is shown in the median value of integration time.

Before the MHD events, the plasma rotation is counter-current directed in the core and slightly co-current directed in the edge. This profile is a typical rotation profile observed in Ohmic discharge in VEST. The intrinsic rotation is determined by balancing the intrinsic torques and momentum flux. One may find the characteristics and methodologies in elsewhere [46, 47]. The clear rotation acceleration in counter-Ip direction is seen at the MHD crash time (~313.2 ms) and the profile relaxes slowly. The corresponding normalized radius of the measurement range is r/a from 0.3 to 1. The modification of toroidal rotation and ion temperature take place in a very wide region of $0.3< r/a <1$. These global changes indicate that the MHD activity creates a counter-current torque as well as ion heating inside the plasma and it cannot explain by enhanced transport effect alone. The toroidal rotation is accelerated up to 30 km/s and ion temperature increases up to 100eV. The profile changes before/after MHD are plotted in Figure 4-6. The dominant source position seems to be located in around R=0.6 m and the position is somewhat consistent with q=1 radius calculated from the equilibrium reconstruction. The inward shift of maxima position of rotation and temperature change may be the result of diffusion process.

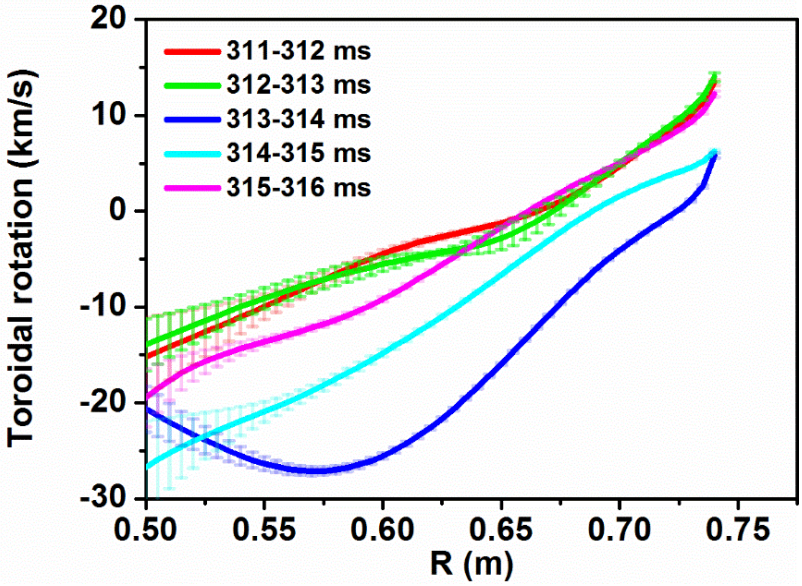

Figure 4-4 Toroidal rotation profile evolution in # 20579. The bursting MHD activity occur at 313.2 ms. Strong rotation acceleration in counter-current direction is observed globally.

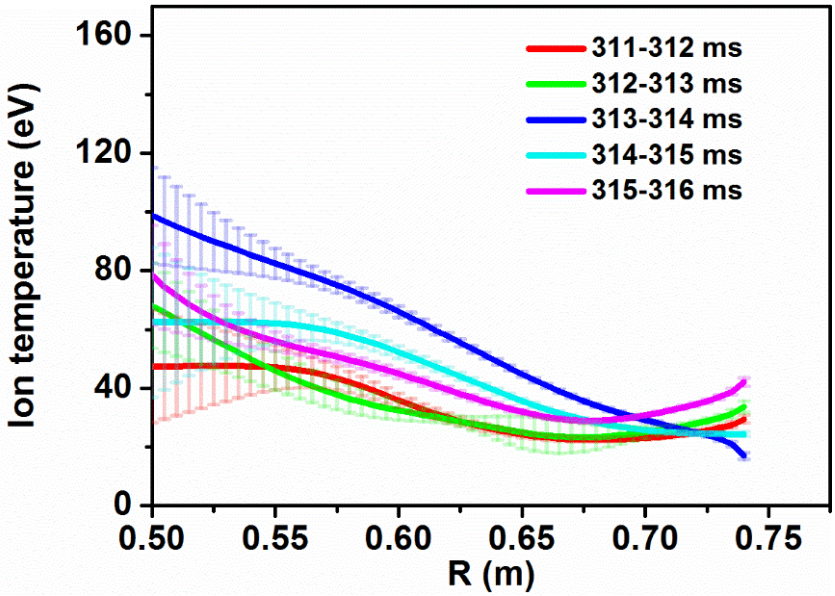

Figure 4-5 Ion temperature profile evolution in # 20579. The bursting MHD activity occur at 313.2 ms. Significant ion heating is observed globally.

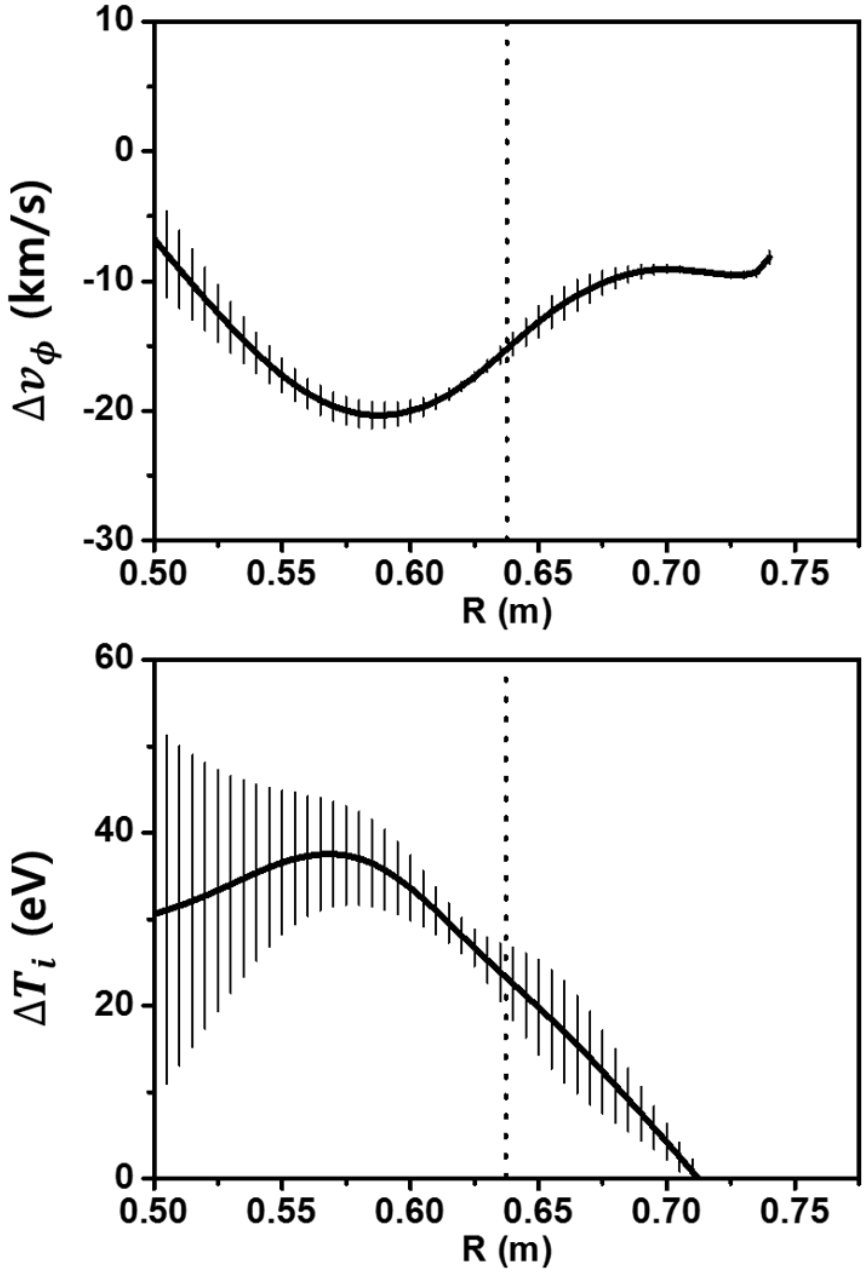

Figure 4-6 Rotation and ion temperature change before and after MHD activity in discharge # 20579. Dashed line shows the q=1 surface based on the equilibrium reconstruction result.

4.1.2. Detail Temporal Dynamics of Ion Properties in Bursting MHD

The temporal evolution of the discharge parameter and raw spectra are seen in Figure 4-7 and Figure 4-8 in discharge #20915. Figure 4-8 shows similar spectra evolution with that of discharge #20579 but the measurement with high temporal resolution (0.2 ms) describes the detail profile recovery process. However, this fast measurement scarifies the information of spatial profile. The measurement position is estimated based on the profile measurement similar discharge and is approximately R= 0.67 which corresponds to r/a is ~0.7.

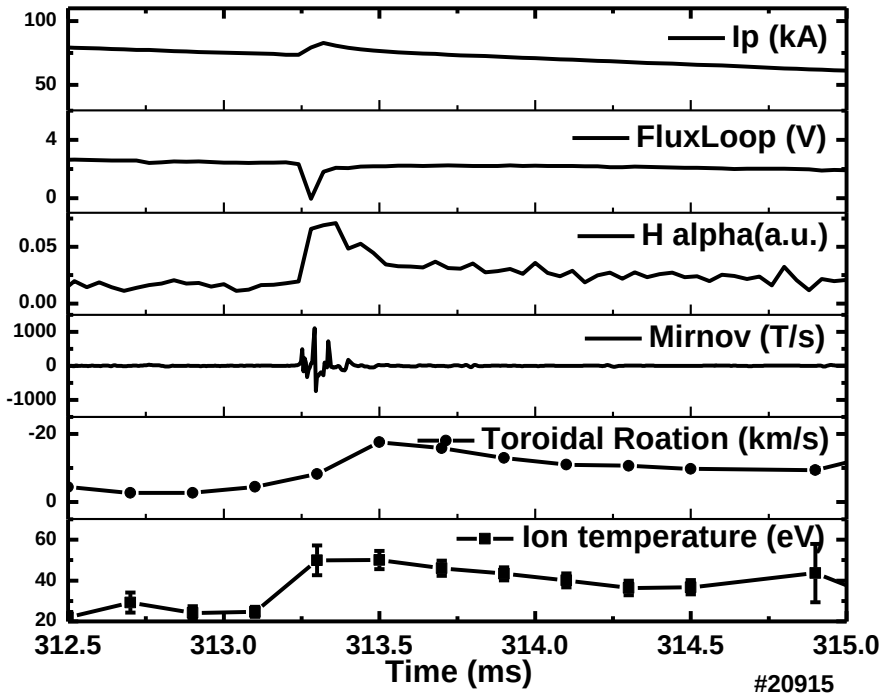

Figure 4-7 Discharge waveform of # 20915. The bursting MHD activity occur at 313.4 ms.

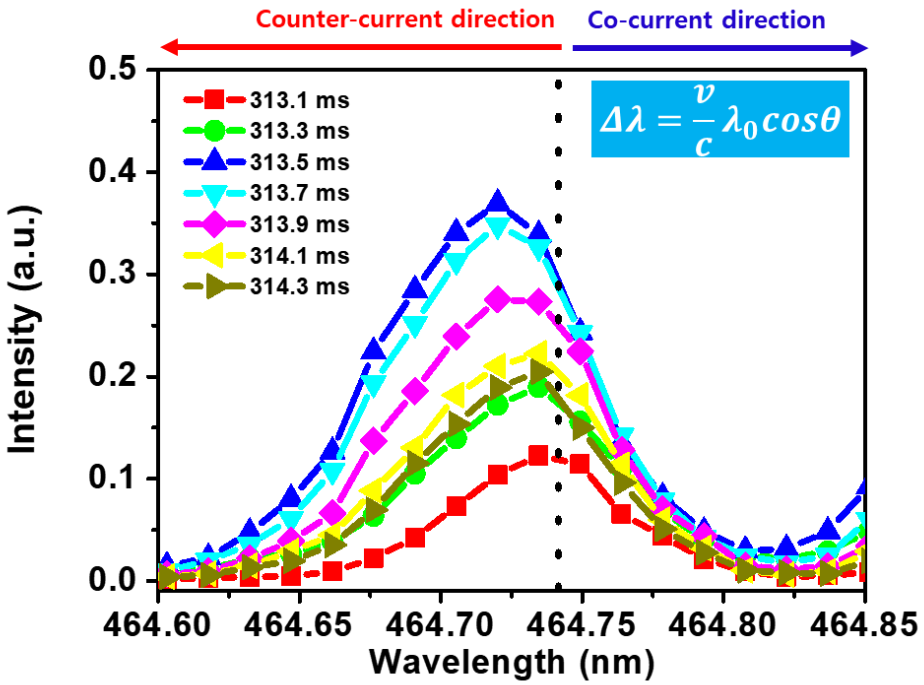

Figure 4-8 Raw line-integrated CIII spectra with the core channel in #20915.

The temporal evolution of ion property can be interpreted based on the simplified 0D balance equation. In the normal state, momentum balance equation is,

$$\frac{d}{dt}\left(m_i n_i R v_\phi\right) = S_{Drive} - S_{loss} - \frac{1}{\tau_M}\left(m_i n_i R v_\phi\right) = 0. \quad (4.1)$$

Where v_ϕ is toroidal rotation, S_{Drive} is the sum of momentum source, S_{loss} is the sum of momentum sink, and τ_M is the momentum transport time. The momentum equation in the normal state determines the intrinsic (baseline) rotation in discharge. Meanwhile, if we consider the unknown torque source during the fast MHD crash event (for $\tau_{MHD} \ll \tau_M, \tau_{Heating}, \tau_{loss}$) the change of rotation (Δv_ϕ) can be described by,

During MHD (For $\tau_{MHD} \ll \tau_M, \tau_{Heating}, \tau_{loss}$)

$$\frac{d}{dt}\left(m_i n_i R \Delta v_\phi\right) \cong S_{MHD} \rightarrow \Delta v_\phi \sim \frac{S_{MHD}}{m_i n_i R}(t - t_0). \quad (4.2)$$

After MHD

$$\frac{d}{dt}\left(m_i n_i R \Delta v_\phi\right) \cong -\frac{1}{\tau_M}\left(m_i n_i R v_\phi\right) \rightarrow \Delta v_\phi \cong \Delta v_M \exp\left(-\frac{t - t_1}{\tau_M}\right). \quad (4.3)$$

Where S_{MHD} is the unknown torque from the MHD, Δv_M is the maximum increment of rotation. From 0-D model point of view, the toroidal rotation increase when the torque exist and then exponentially decay with the momentum confinement time scale. With this analogy, we fit the temporal evolution of toroidal rotation as shown in Figure 4-10. Similar work is also conducted for the ion temperature. The experimental data are well-fitted in this manner and the decay time is 1.1 ms which is consistent with typical confinement time of VEST [46]. The acceleration and ion heating time is very fast <300 μs.

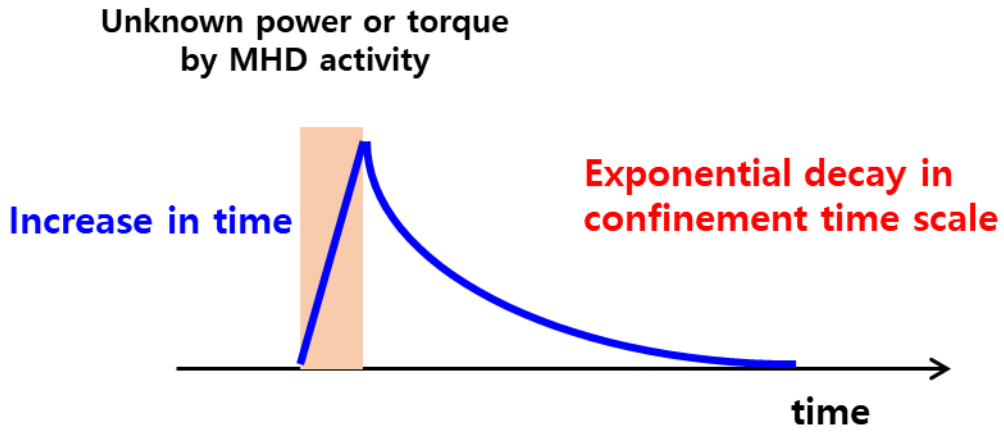

Figure 4-9 Simple 0-D description of the temporal behavior of ion property with unknown source during MHD activity.

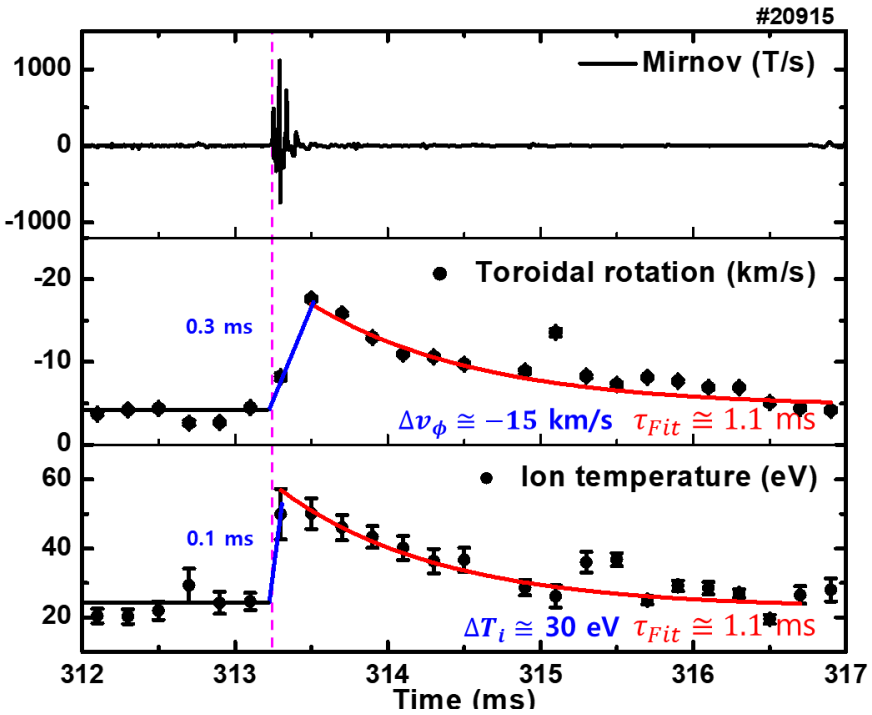

Figure 4-10 Temporal dynamic of toroidal rotation and ion temperature during a bursting MHD activity. The measurement position is approximately R=0.67 (i.e. r/a~-0.7). The fitting result with a 0-D balance point of view is overlaid in a solid line.

4.2. Ion Heating during the MHD Events

A clear increase of ion temperature is accompanied in bursting MHD activity. The MHD activity accompanies magnetic reconnection and the main effect in tokamak plasma is degrade the confinement by disrupting closed magnetic surfaces, allowing the hot central plasma to mix with cooler plasma closer to the edge [34]. On the other hand, magnetic reconnection is the relaxation process and released magnetic energy can be transferred to the particle. Significant ion heating during the magnetic reconnection is frequently observed in the laboratory [47, 48, 49, 50, 51] and the astrophysical plasma [39]. Particularly, ion heating in the MHD relaxation process is also reported in reversed field pinch (RFP) [50] and ST [46]. Even though the exact ion heating mechanism is still in many argument [47, 51, 48, 50], fast ion heating characteristics is well-known similar to our observation.

The increased ion thermal energy come from the magnetic field energy via the magnetic reconnection. Magnetic reconnection occurs by combining adjacent flux surface and the main reconnecting magnetic field may be some part of the poloidal magnetic field. After the MHD activity, there will be a drop of the poloidal magnetic field energy. We calculate the poloidal magnetic field energy based on the equilibrium reconstruction as following

$$W_B = \int_{V_{plasma}} \frac{B_p^2}{2\mu_0} dV. \tag{4.4}$$

The temporal variation of poloidal magnetic field energy is plotted in Figure 4-11. We can clearly see the poloidal magnetic field energy drop after MHD activity. The slight delay

of the drop of magnetic energy may be due to the uncertainty of equilibrium reconstruction during the distorted magnetic surface.

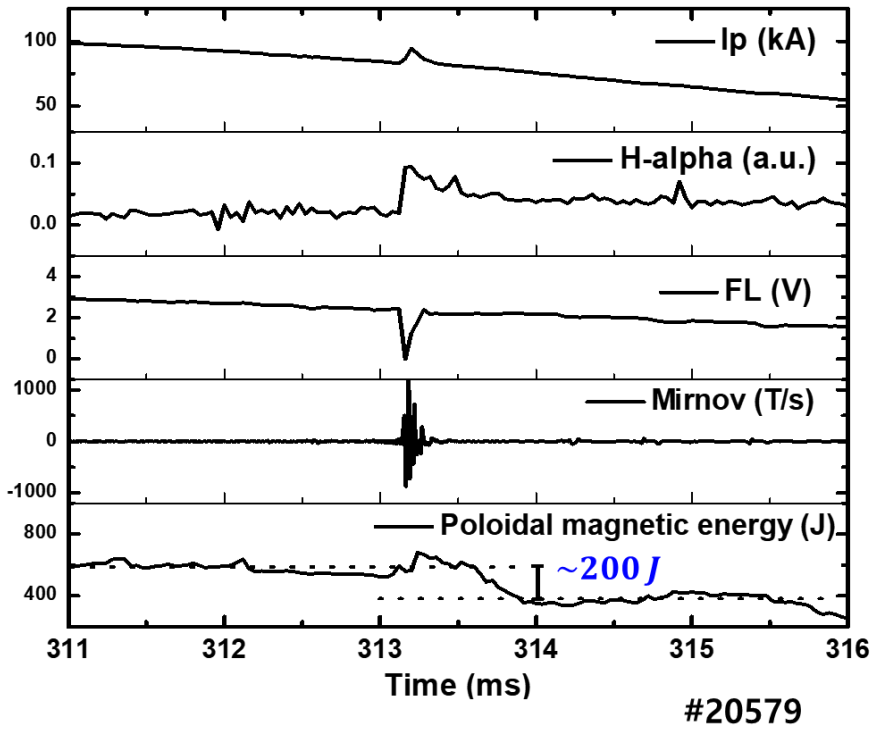

Figure 4-11 Poloidal magnetic field energy drop after MHD activity. Poloidal magnetic field energy is calculated from the equilibrium reconstruction result.

Now, we estimate the energy transfer rate during the bursting MHD in VEST. The dissipated magnetic energy is,

$$\Delta W_B = \Delta \int_{V_{plasma}} \frac{B_p^2}{2\mu_0} dV \sim -200\, J. \tag{4.5}$$

The increase of ion thermal energy is estimated with TS data and assume the flat density profile with$n_e = 10^{18} m^{-3}$.

$$\Delta W^i_{thermal} = \int_{V_{plasma}} \frac{3}{2} n_i \Delta T_i \, dV \sim \frac{3}{2} n \Delta T_i V \sim 10\, J. \tag{4.6}$$

The increment of ion rotation energy is,

$$\Delta W^i_{rotation} = \int_{V_{plasma}} \frac{1}{2} n_i m_i \, (v_f^2 - v_i^2) \, dV \sim \frac{1}{2} m_i n_i v_f^2 V \sim 1\, J \tag{4.7}$$

The energy transfer rate ($\Delta W^i_{thermal}/\Delta W_B$**)** is about 5% in the bursting MHD activity. By considering the uncertainty of equilibrium reconstruction and measurement, it is a reasonable agreement with the value of other magnetic reconnection experiments which is in the range of 10% to 80%. Therefore, we can conclude the strong ion heating come from reconnection heating.

There are many hypotheses to explain the anomalous ion heating during the magnetic reconnection such as viscous damping of reconnection outflows [47, 52], resonant heating of magnetic fluctuation at the ion cyclotron frequency [51], Re-magnetization in the downstream region with collisional scattering process [48]. Based on the mechanism of viscous damping of reconnection outflows, bi-directional flows should be captured in the reconnection region. However, we cannot measure such bi-directional flows in several experiments. Ultrafast diagnostic system (~5 μs) such as a Mach probe will be required to clarify the detail process because these flows are very instantaneous [47] and damped quickly in previous results.

Another candidate mechanism for ion heating is related to the magnetic perturbation. In RFP plasmas at MST device [51], impurity ion temperatures above 1 keV were observed during the MHD dynamo activity. They found that high frequency magnetic perturbation was observed during the activity up to the ion cyclotron frequency. There is a dip in the frequency spectrum of the fluctuation near the ion cyclotron frequency and it suggests that the magnetic perturbation energy is transfer to the ion thermal energy by cyclotron heating mechanism.

Based on the fluctuation heating model, we investigate the correlation between ion temperature increase (ΔT_i) and magnetic perturbation amplitude ($\delta B/B$). One note that the ion heating is believed to relate to the high frequency perturbation in the magnetic reconnection. However, the current status of magnetic sensor installed in VEST is limited to measure the high frequency perturbation above 100 kHz. In this preliminary analysis, we use moderate frequency perturbation (> 5 kHz) instead and additional magnetic

sensors will be necessary. Statistical analysis is conducted by collecting the data of various amplitudes of bursting MHD activities. For the amplitudes of the magnetic perturbations, we use the peak amplitudes of magnetic perturbations during the bursting events. Figure 4-12 shows the correlation between ion temperature increase and amplitude of magnetic perturbation. At the small magnetic perturbation amplitude, the ion heating rate is correlated with the amplitude of magnetic perturbation. However, at the large amplitude of magnetic perturbation, the ion heating rate is saturated. This result could be explained by competition between reconnection heating and confinement degradation. If strong magnetic reconnection occurs, not only reconnection heating but also significant confinement degradation can be expected. In small reconnection events, the reconnection heating is dominant and ion heating is correlated with the amplitude of magnetic perturbation. On the other hand, in large reconnection events, the confinement degradation by magnetic topology change plays a role and the ion heating rate is saturated. The change in H alpha signal supports the explanation. Figure 4-13 shows the collected data of change in H alpha intensity during bursting MHD events. At the small reconnection event ($\delta B/B$ <4%), the change in H alpha intensity is small and it suggest weak confinement loss during the events. However, in strong reconnection with $\delta B/B$ >5%, a significant increase in H alpha intensity is observed and a huge amount of energy loss is expected. This is consistent with the usual observations of an energy drop in conventional tokamak during the severe MHD instabilities.

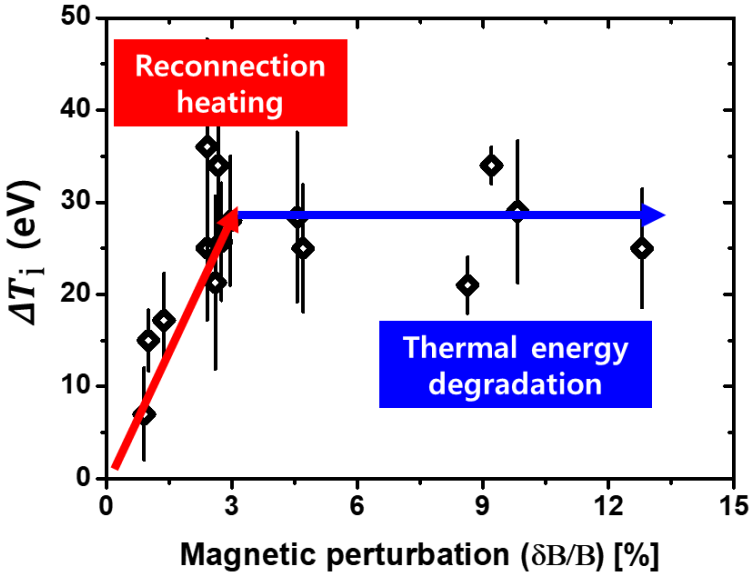

Figure 4-12 Ion temperature increase versus the maximum amplitude of magnetic perturbation during the bursting MHD events. At the small magnetic perturbation amplitude, the ion heating rate is correlated with the amplitude of magnetic perturbation. At the large amplitude of magnetic perturbation, the ion heating rate is saturated.

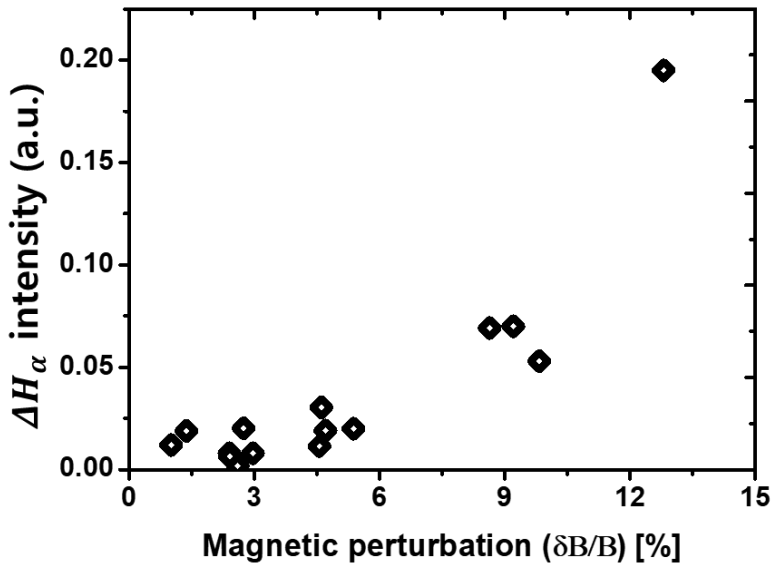

Figure 4-13 Ion temperature increase versus the maximum amplitude of magnetic perturbation during the bursting MHD events. This result shows the degradation of confinement exponentially increases as the amplitude of magnetic perturbation grows.

4.3. Possible Candidate Mechanisms for the Sudden Spin-up

The study has shown that MHD evens have a significant effect on plasma rotation and strong torque can be exerted to the plasma. In this section, we discuss the rotation acceleration mechanism in terms of temporal behavior, the direction of torque and torque amplitude. We consider four candidate mechanisms: Reconnection outflows, Toroidal electric field by reconnection process, Enhanced electron loss, and NTV torque with an offset rotation.

4.3.1. Reconnection Outflows

Many observations suggest a generation of strong outflows during the magnetic reconnection [60, 61, 53, 62, 54]. These flows can contribute the reconnection heating via the viscous damping [47]. The bidirectional outflows are generated right after the reconnection, suddenly damped by viscosity and then heat the ions. This process suggests that the ion acceleration should come before the ion heating. But in our observation (see Figure 4-14), the increase of ion temperature precedes the rotation acceleration. This temporal sequence is inconsistent with the reconnection model. Also, the preferential acceleration direction in counter-current cannot be explained by this mechanism because bi-directional outflow cannot generate total angular momentum.

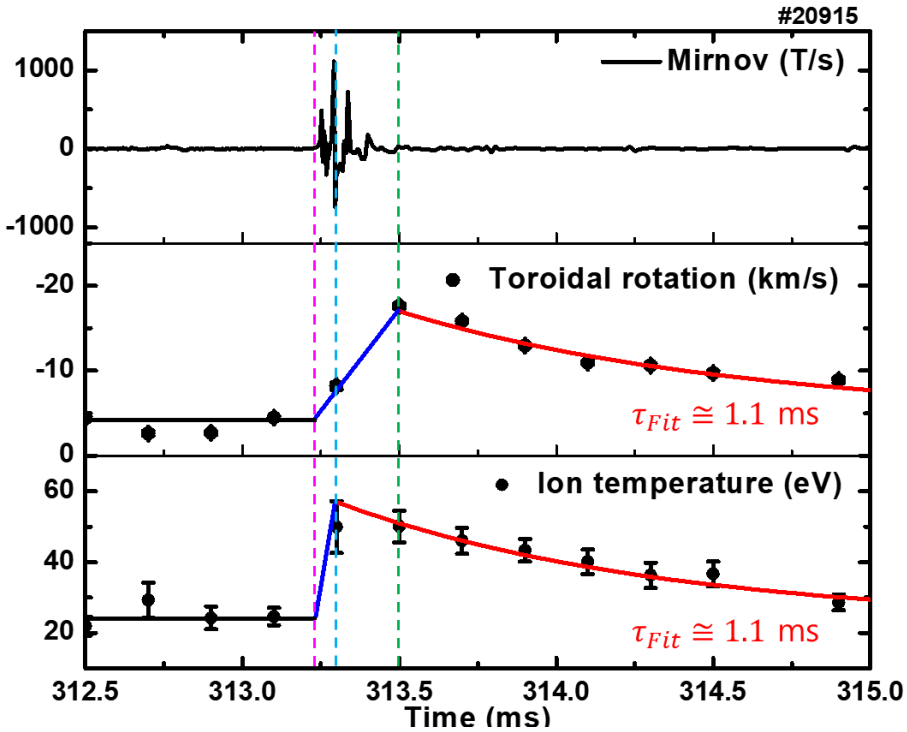

Figure 4-14 Detail temporal behavior of toroidal rotation and ion temperature. The increase of ion temperature precedes the rotation acceleration.

4.3.2. Toroidal Electric Field by Reconnection Process

MHD crash events redistribute the plasma current profile in a very short time. The fast change in current profile accompanies poloidal flux change and toroidal electric field can be produced by induction law. This mechanism is considered as an important mechanism in generation of energetic ions [56, 57] and electrons [58]. In order to test this mechanism, the simplified momentum equation considering poloidal flux change is used. If we assume the reconnection occurs in an axisymmetric way, the loop voltage can be obtained from a standard equilibrium reconstruction.

Toroidal electric field is induced by poloidal flux change as a following equation

$$E_\phi = -\frac{1}{2\pi R}\frac{d\psi}{dt}. \tag{4.8}$$

Simplified momentum equation neglecting the momentum transport is,

$$\frac{dv_\phi}{dt} \cong \frac{qE_\phi}{m} = -\frac{q_i}{2\pi mR}\frac{d\psi}{dt}. \tag{4.9}$$

By integrating over the crash time, change in Toroidal rotation after MHD event is as following

$$\Delta v_\phi \cong \frac{qE_\phi}{m} = -\frac{q_i}{2\pi mR}\Delta\psi. \tag{4.10}$$

The result shows that the change of toroidal rotation is proportional to the poloidal flux change. We note that the result is independent to the time but the equation is only valid when torque from toroidal electric field is dominant and other effects such as collisional drag, viscous force and transport are negligible. Figure 4-15 shows the poloidal flux change after the event based on the equilibrium reconstruction result. The toroidal

rotation by poloidal flux change is calculated based on the equation (). The maximum poloidal flux change is about 0.5 mWb on R=0.5m and estimate rotation change is maximum 1km/s in co-current direction. The rotation drive direction is opposite to our experimental observation and its magnitude is also negligibly small.

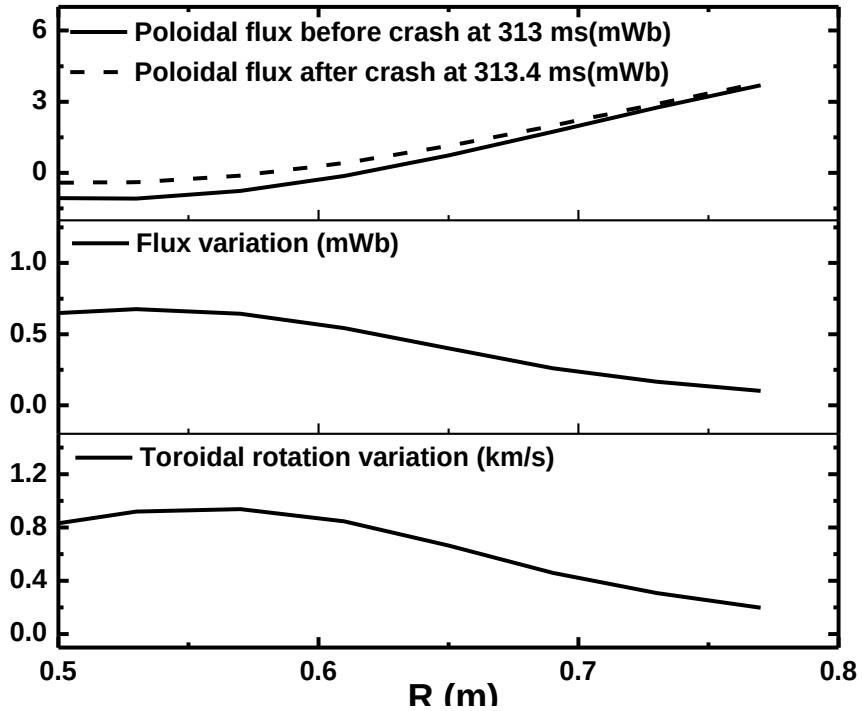

Figure 4-15 Estimated toroidal rotation change from the electric field by MHD event. (Top) poloidal flux before/after MHD crash event (middle) poloidal flux change (bottom) induced toroidal rotation by poloidal flux change.

4.3.3. Enhanced Electron Loss Mechanism

In the experiment of DED (Dynamic Ergodic Divertor) in TEXTOR, the deeply penetrating external magnetic field perturbation increases the toroidal rotation [59]. The explanation of the rotation acceleration is an enhanced radial transport of electrons. When the magnetic perturbation is induced by DED coil current, stochastic magnetic flux is formed and electrons are lost along the open field lines. This causes charge separation and generate a radial electric field (E_r). In order to satisfy the radial force balance ($E_r = (Z_i e n_i)^{-1} \partial_{\mathrm{r}} P_i - v \times B$), the toroidal rotation is produced. (i.e. $v_\phi \times B_\theta$ component is balanced with E_r.)

The MHD activity accompanies strong magnetic perturbation as shown in Figure 4-14. In that sense, the MHD phenomenon can play a similar role. However, the fast electron loss induces the co-current rotation and it is the opposite direction of our observation based on this mechanism.

4.3.4. NTV Torque with an Offset Rotation Velocity

We can consider MHD activity as a kind of 3D magnetic perturbation. One important effect of 3D magnetic perturbation is the NTV torque. The viscous force by NTV toward the offset frequency ($v_{\phi,NTV}$) is theoretically predicted [60, 61] and experimentally validated in DIII-D [62]. In the presence of 3D non-axisymmetric magnetic perturbation, plasma ion can radially drift on the perturbed magnetic field line. The non-ambipolar radial ion flux induces the NTV torque. The offset rotation represents the decrease in E_r needed to hold back more thermal ions to obtain ambipolarity when dT_i/dr < 0 [49]. The neoclassical theory predict a NTV torque (S_{NTV}) and offset rotation ($v_{\phi,NTV}$) as following [62, 64]

$$S_{NTV} = -m_i n_i \mu_{\parallel} \left(\frac{\delta B}{B}\right)^2 \left(v_{\phi} - v_{\phi,NTV}\right) \tag{4.11}$$

$$v_{\phi,NTV} \cong R \frac{k_c}{q_i} \frac{dT_i}{d\psi_p}. \tag{4.12}$$

Where S_{NTV} is the NTV torque density, the $\mu_{\parallel}$ is the damping constant depending on the collisionality regime. $v_{\phi,NTV}$ is NTV offset rotation velocity, δB is the magnetic perturbation, and k_c is the constant depending on the collisionality regime: $k_c \cong 3.5$ in the banana regime with $\omega_E < \nu_i/\varepsilon < \omega_{ti}\sqrt{\varepsilon}$.

In ion collisionality regime in 1/ν ($\nu_i/(\omega_{ti}\varepsilon^{3/2}) \cong 0.3 < 1$ (with T_i=20 eV, n_e=10^{18} m^{-3},) the offset rotation velocity is calculated based on the equilibrium reconstruction and ion temperature measurement in Figure 4-16. The offset rotation velocity is 40 km/s in counter-current direction and it is enough value to accelerate plasma.

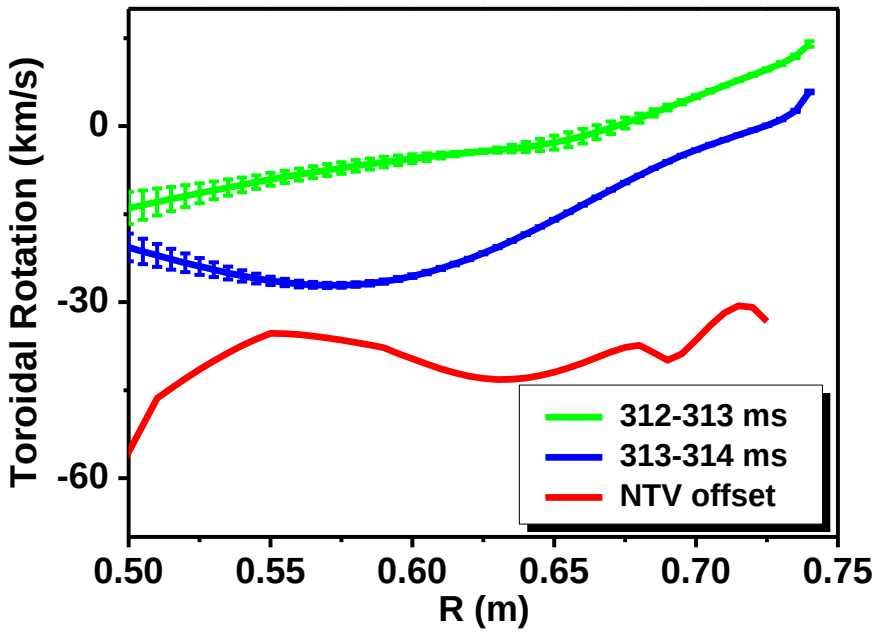

Figure 4-16 Estimated NTV offset rotation velocity in # 20519. The offset rotation is about 40 km/s in counter current direction

The estimation is conducted based on a simplified 0D momentum balance equation and we compare the model result to experimental result in # 20915. We consider only rotation change (Δv_ϕ). The balance equation is written as,

$$m_i n_i R \frac{d\Delta v_\phi}{dt} = S_{NTV} - \frac{m_i n_i R \Delta v_\phi}{\tau_M} \tag{4.13}$$

And

$$S_{NTV} \cong 6.1C \;\; n_i m_i v_{ti}^2 \; \frac{\epsilon^{\frac{3}{2}}}{\nu_i R} n^2 (\delta B/B)^2 \left(v_\phi - v_{\phi,\,NTV}\right). \tag{4.14}$$

Where $(\delta B/B)$ is the magnetic perturbation, $v_{\phi,\,NTV}$ is the NTV offset velocity, n_i is the ion density, T_i is the ion temperature. The magnetic perturbation is a result of MHD instability and plasma response plays a key role in determining δB. For the simply estimate the magnitude of NTV torque, we use the Mirnov sensor signal installed in vacuum chamber in LFS and compensate radial decay with the following formula: $\frac{1}{2}\left(\frac{b}{r}\right)^{m+1} |\delta B_z|_{wall}$ [63]. The NTV offset velocity is set to -40 km/s based on similar discharge # 20579 as shown in Figure 4-15.

The 0D model based temporal behavior of toroidal rotation is compared with measured rotation (see Figure 4-17). Because there is uncertainty about the ion density in the present situation, we plotted numerical results at various reasonable density conditions. The small moment of inertia with low density plasma and small major radius in ST allow strong variation of rotation. The NTV torque is strong enough to drive the toroidal rotation up to the experimental value in counter-current direction with $n_i = 10^{19}$ m^{-3}. It strongly suggests that NTV torque is a most probable mechanism to explain the sudden spin-up

after MHD activity.

However, there is a timescale problem to apply NTV torque theory. NTV torque is a result of neoclassical transport theory and it requires the successive time scale for several constraints [49]. At first, MHD radial force balance equilibrium should be satisfied from the compressional Alfven waves on the Alfvenic time scale (~μs). It usually holds because the MHD crash time is around 300 μs and there is two orders of magnitude difference. Second, the electron and ion should be equilibrated along the field lines by the thermalization process. Typically, the thermalization process needs a collision times which are 20 μs for electrons and 0.1 ms for ions. Also, the poloidal flow should be damped from the ion collisional effect and it takes the time of ion collision time. In the MHD crash event, the time scale (~0.1ms) for thermalization and poloidal flow damping is comparable to the MHD crash time (~0.3ms) and it is in the marginal region to apply NTV torque theory. Due to time-scale issues, NTV torque may not be fully utilized but may be partial.

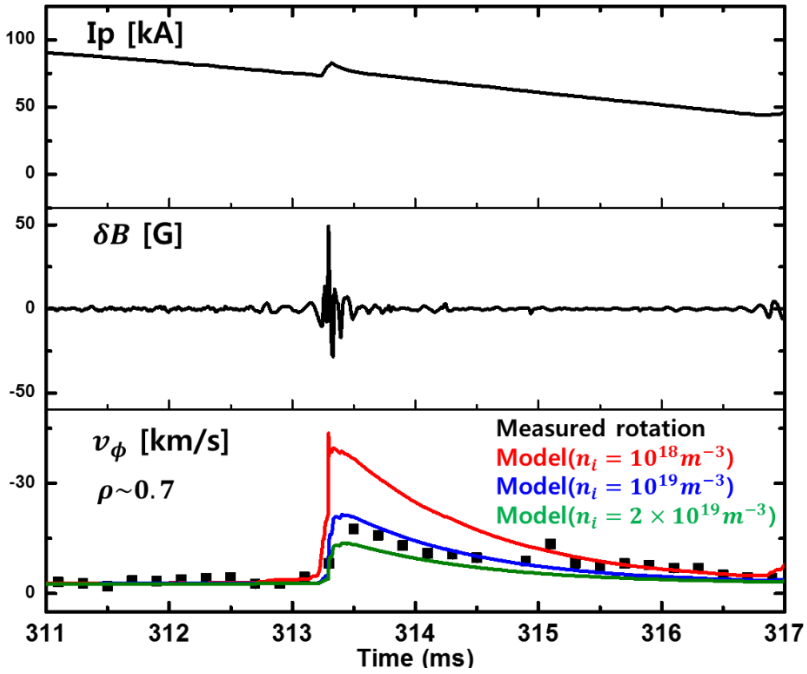

Figure 4-17 Measured toroidal rotation is compared with the 0-D NTV torque model result during bursting MHD event. With a model result with an ion density 10^{19} m^{-3}, the experimental result is a reasonably agreement

Chapter 5. Conclusions and Future Work

5.1. Summary and Conclusions

This work has aimed to investigate the dynamic evolution of ion properties (ion temperature and rotation) during the fast bursting MHD activities by using ultrafast IDS (Ion Doppler Spectroscopy) diagnostics.

In order to explore the influence of the MHD activities with a very short time scale, fast IDS (Ion Doppler Spectroscopy) system has been successfully designed, constructed, and optimized. The high throughput (f/2.8) spectrograph based on the grism as a dispersive component is made to obtain the sufficient signal-to-noise ratio even in sub-millisecond exposure time. There are two special measurement modes. Multi-channel measurement mode with 10 spatial channel is used for spatial profile measurement by using a tomographic technique with 1ms temporal resolution. And, single-channel measurement mode with 0.2 ms temporal resolution allows detail temporal dynamics of rotation and ion temperature.

Doppler tomography technique is intensively tested and utilized to unfold the line-integrated spectra along the line-of-sight. The major improvement is a systematic formulation of the tomographic technique by utilizing 2nd order Tikhonov regularization technique. This technique efficiently reduces the ill-posedness of the tomographic problem. The validation works of the technique are conducted with VEST-plasma like phantom profiles. The reconstructed profiles are good agreements with the phantom profiles within the 10% systematic errors. The boundary conditions as additional constraints are very sensitive to the reconstruction result and should be set to the farther

than the actual boundary. Also, appropriate quantification of the uncertainties of the IDS system is analyzed by considering the propagation of errors of fitted parameters of spectra based on the numerical Monte Carlo (MC) method. The typical uncertainties are 1-15% and 3-35% from the edge to the core for the emissivity and ion temperature, respectively. In order to measure the accurate parameters in the core region, different measurement methods such as charge exchange spectroscopy (CES) or high charge-state emission are recommended in the future for a high performance discharge.

The significant rotation acceleration ($\Delta v_\phi \sim 20\mathrm{km/s}$) as well as ion heating ($\Delta T_i \sim 40$ eV) is observed during the bursting MHD activity, accompanying global profile change even in the interior region (up to $\rho > 0.3$) within a short time scale(<0.3 ms). Because there are no external heating and torque sources in Ohmic plasmas, this result clearly shows MHD instabilities act as torque and heating source. Bursting MHD activities accompany magnetic reconnection phenomenon by reconnecting magnetic field line and combining adjacent flux surfaces. During the magnetic reconnection, reduced magnetic field energy is converted to the thermal particles (especially ions). From the equilibrium reconstruction result, poloidal magnetic field energy is reduced from 600 J to 400 J. About 5% of reconnected magnetic field energy is converted to the ion thermal energy during the reconnection. Based on the fluctuation heating model, we collect the database of the bursting MHD activity and investigate the correlation between magnetic fluctuation amplitude with a frequency above 5 kHz and ion temperature increase. Ion heating rate increase and then saturate as fluctuation amplitude increase. One explanation of this tendency is a competition between reconnection heating and confinement

degradation. In the weak reconnection event, reconnection heating is a dominant process compared to the confinement loss. However, in the strong reconnection event, confinement loss during the reconnection event plays a role in ion heating rate. The H alpha emission signal supports the tendency. The intensity of the H alpha emission spike is quite weak in the small event and dramatically increase in the strong reconnection event. Further analysis and experimental exploration will be required to clarify the details.

Several physical mechanisms to account for the sudden spin-up of the plasma are discussed in terms of temporal behavior, the direction of torque and torque amplitude. We consider four candidate mechanisms: Reconnection outflows, Toroidal electric field by reconnection process, Enhanced electron loss, and NTV torque with an offset rotation. Among them, the NTV torque mechanism is a strong candidate to account for the experimental observation. In the $1/\nu$ collisionality regime, NTV torque can accelerate up to 40 km/s (NTV offset velocity) in the counter-current direction and this value is enough to explain the experimental result. The observed temporal behavior of toroidal rotation during the bursting MHD event is understood by the 0-D torque model, balancing the NTV torque and confinement loss. The simulation results are consistent with the experimental data within the reasonable parameter range.

Strong plasma rotation accelerations during the MHD activities are experimentally investigated for the first time. This observation will help us understand the interaction between the MHD event and the plasma rotation. In particular, this result suggests the possibility of the interplay between MHD instability and induced plasma rotation such as the self-organization process.

5.2. Recommendations for Future Work

In this work, experimental explorations on bursting MHD activities are conducted by developing new spectroscopic diagnostics. For the extension of this work, several remaining subjects are recommended for further understanding.

Bursting MHD events on VEST plasma should be identified to understand detailed process and control the mode onset. In order to classify the MHD events, stability analysis with numerical codes should be done with an improved equilibrium result. Especially, since MHD stability is very sensitive to the kinetic profiles and safety factor, equilibrium reconstruction with constraints in internal properties (n_e, T_e, and q) is essential. Also, the MHD instability can be characterized by spatial structures in radial or/and poloidal structure. The internal measurements such as SXR measurement with tomography technique and an internal magnetic probe will be helpful to identify the structure. By comparing the mode structures obtained by experiments and numerical results [69], further understanding of bursting MHD events can be achieved.

The heating mechanisms during the magnetic reconnection process still remains unsolved. According to the viscous heating model by reconnection outflows, two bi-directional outflows occur in a very short time. In order to capture the detail dynamics during the reconnection, an ultrafast diagnostics system with improved time resolution on the order of few microseconds will be required. Probably, PMTs (Photomultiplier tubes)-based spectroscopy or Mach probe could be used for that purpose. Also, high frequency fluctuations are believed to play a role in particle heating during the reconnection. The

initial result in bursting MHD events shows the broadband frequency spectra above 100 kHz. Recent experimental results on the reconnection events revealed that when magnetic reconnection occurs, magnetic fluctuation occurs up to lower hybrid frequency. Installation of additional magnetic sensors will be helpful to understand the mode cascade phenomenon during the reconnection and to clarify its roles.

Bibliography

[1] M. Kikuchi, K. Lackner and M. Q. Tran, Fusion Physics, Vienna: IAEA, 2012.

[2] J. Wesson, Tokamaks, New York: Clarendon Press - Oxford, 2004.

[3] M. Gryaznevich, R. Akers, P. G. Carolan, N. J. Conway, D. Gates, A. R. Field, T. C. Hender, I. Jenkins, R. Martin, M. P. S. Nightingale, C. Ribeiro, D. C. Robinson, A. Sykes, M. Tournianski, M. Valovi and M. J. Walsh, "Achievement of Record β in the START Spherical Tokamak," *Physical Review Letters,* vol. 80, p. 3972, 1998.

[4] M. Ono, S. Kaye, Y.-K. Peng, G. Barnes, W. Blanchard, M. Carter, J. Chrzanowski, L. Dudek, R. Ewig, D. Gates, R. Hatcher, T. Jarboe, S. Jardin, D. Johnson, R. Kaita, M. Kalish, C. Kessel, H. Kugel, R. Maingi, R. Majeski, J. Manickam, B. McCormack, J. Menard, D. Mueller, B. Nelson, B. Nelson, C. Neumeyer, G. Oliaro, F. Paoletti, R. Parsells, E. Perry, N. Pomphrey, S. Ramakrishnan, R. Raman, G. Rewoldt, J. Robinson, A. Roquemore, P. Ryan, S. Sabbagh, D. Swain, E. Synakowski, M. Viola, M. Williams and J. Wilson, "Exploration of spherical torus physics in the NSTX device," *Nuclear Fusion,* vol. 40, p. 557, 2000.

[5] B. Lloyd *et al.,* "Overview of recent experimental results on MAST," *Nuclear Fusion,* vol. 43, p. 1665, 2003.

[6] A. Sykes, A. Costley, C. Windsor, O. Asunta, G. Brittles, P. Buxton, V. Chuyanov, J. Connor, M. Gryaznevich, B. Huang, J. Hugill, A. Kukushkin, D. Kingham, A. Langtry, S. McNamara, J. Morgan, P. Noonan, J. Ross and V. Shev, "Compact fusion energy based on the spherical tokamak," *Nucl. Fusion,* vol. 58, p. 016039, 2017.

[7] K. J. Chung, Y. H. An, B. K. Jung, H. Y. Lee, C. Sung, Y. S. Na, T. S. Hahm and Y. S. Hwang, "Design Features and Commissioning of the Versatile Experiment Spherical Torus (VEST) at Seoul National University," *Plasma Sci. Technol.,* vol. 15, p. 244, 2013.

[8] Eurofusion organization, "Tokmak Principle," [Online]. Available: https://www.euro-fusion.org/2011/09/tokamak-principle-2/?view=gallery-11.

[9] M. Ono and R. Kaita, "Recent progress on spherical torus research," *Phys. Plasmas,* vol. 22, p. 040501, 2015.

[10] A. Leonard, R. Groebner, M. Mahdavi, T. Osborne, M. Fenstermacher, C. Lasnier and T. Petrie, "ELM energy scaling in DIII-D," *Plasma Phys. Control. Fusion,* vol. 44, p. 945, 2002.

[11] H. Lee, S. Lee, J. Seol, A. Aydemir, C. Bae, J. Yoo, Y. Na, H. Kim, M. Woo, J. Kim, M. Joung, K. You and B. Park, "Tearing modes induced by perpendicular electron cyclotron resonance heating in the KSTAR tokamak," *Nucl. Fusion,* vol. 54, p. 103008, 2014.

[12] S. Gerhardt, D. Brennan, R. Buttery, R. L. Haye, S. Sabbagh, E. Strait, M. Bell, R. Bell, E. Fredrickson, D. Gates, B. LeBlanc, J. Menard, D. Stutman, K. Tritz and H.

Yuh, "Relationship between onset thresholds, trigger types and rotation shear for the m/n = 2/1 neoclassical tearing mode in a high-β spherical torus," *Nucl. Fusion,* vol. 49, p. 032003, 2009.

[13] R. Buttery, R. L. Haye, P. Gohil, G. Jackson, H. Reimerdes, E. Strait and DIII-DTeam, "The influence of rotation on the βN threshold for the 2/1 neoclassical tearing mode in DIII-D," *Phys. Plasmas,* vol. 15, p. 056115, 2008.

[14] J. Berkery, S. Sabbagh, R. Betti, B. Hu, R. Bell, S. Gerhardt, J. Manickam and K. Tritz, "Resistive Wall Mode Instability at Intermediate Plasma Rotation," *Phys. Rev. Lett,* vol. 104, p. 035003, 2010.

[15] M. Okabayashi, P. Zanca, E. Strait, A. Garofalo, J. Hanson, Y. In, R. L. Haye, L. Marrelli, P. Martin, R. Paccagnella, C. Paz-Soldan, P. Piovesan, C. Piron, L. Piron, D. Shiraki, F. Volpe, DIII-DTeam and RFX-modTeam, "Avoidance of tearing mode locking with electro-magnetic torque introduced by feedback-based mode rotation control in DIII-D and RFX-mod," *Nucl. Fusion,* vol. 57, p. 016035, 2017.

[16] M. Okabayashi, J. Bialek, M. Chance, M. Chu, E. Fredrickson, A. Garofalo, R. Hatcher, T. Jensen, L. Johnson, R. L. Haye, G. Navratil, H. Reimerdes, J. Scoville, E. Strait, A. Turnbull, M. Walker and DIII–DTeam, "Stabilization of the resistive wall mode in DIII–D by plasma rotation and magnetic feedback," *Plasma Phys. Control. Fusion,* vol. 44, p. B339, 2002.

[17] A. Kuritsyn, G. Fiksel, A. Almagri, D. Brower, W. Ding, M. Miller, V. Mirnov, S. Prager and J. Sarff, "Measurements of the momentum and current transport from tearing instability in the Madison Symmetric Torus reversed-field pinch," *Phys. Plasmas,* vol. 16, p. 055903, 2009.

[18] J. Seol, S. Lee, B. Park, H. Lee, L. Terzolo, K. Shaing, K. You, G. Yun, C. Kim, K. Lee, W. Ko, J. Kwak, W. Kim, Y. Oh, J. Kim, S. Kim and K. Ida, "Effects of Electron-Cyclotron-Resonance-Heating-Induced Internal Kink Mode on the Toroidal Rotation in the KSTAR Tokamak," *Phys. Rev. Lett.,* vol. 109, p. 195003, 2012.

[19] S. Sabbagh, J. Berkery, R. Bell, J. Bialek, S. Gerhardt, J. Menard, R. Betti, D. Gates, B. Hu, O. Katsuro-Hopkins, B. LeBlanc, F. Levinton, J. Manickam, K. Tritz and H. Yuh, "Advances in global MHD mode stabilization research on NSTX," *Nucl. Fusion,* vol. 50, p. 025020, 2010.

[20] S. Sabbagh *et al,* "Resistive wall stabilized operation in rotating high beta NSTX plasmas," *Nucl. Fusion,* vol. 46, p. 635, 2006.

[21] B. Tobias, M. Chen, I. G. J. Classen, C. W. Domier, R. Fitzpatrick, B. A. Grierson, J. N. C. Luhmann, C. M. Muscatello, M. Okabayashi, K. E. J. Olofsson and C. Paz-Soldan, "Rotation profile flattening and toroidal flow shear reversal due to the coupling of magnetic islands in tokamaks," *Phys. Plasmas,* vol. 23, p. 056107, 2016.

[22] J. Yang, Tearing Modes during Tokamak Plasma Current Ramp Up, Ph.D Thesis: Seoul National University, 2019.

[23] Y.-G. Kim, D. Kim, J.-H. Lee, M.-G. Yoo, H. Lee, S. Kim, C.-Y. Lee, Y. Kim,

Y.S.Hwang and Y.-S. Na, "Development of Thomson scattering system on VEST," *Fus. Eng. Des.,* vol. 143, p. 130, 2019.

[24] R. E. Bell, "An inversion technique to obtain full poloidal velocity profiles in a tokamak plasma," *Rev. Sci. Instrum.,* vol. 68, p. 1273, 1997.

[25] I. Condrea, E. Haddad, B. Gregory and G. Abel, "Local poloidal and toroidal plasma rotation velocities and ion temperature in a tokamak plasma obtained with a matrix inversion method considering asymmetries," *Phys. Plasmas,* vol. 7, p. 3641, 2000.

[26] Y. Shi, S. Lee, K. Hill and M. Bitter, "Inversion technique to obtain local rotation velocity and ion temperature from line-integrated measurements for elongated tokamak plasma," *Rev. Sci. Instrum.,* vol. 83, p. 10D717, 2012.

[27] Y. Kim, Y.-J. Shi, K. Lee, S.-G. Oh, M. v. Hellermann, K.-J. Chung and Y. .Hwang, "Design of combined system of helium charge exchange spectroscopy and hydrogen beam emission spectroscopy in VEST," *Fus. Eng. Des.,* vol. 123, p. 975, 2017.

[28] M. Czerny and A. F. Turner, "Über den Astigmatismus bei Spiegelspektrometern," *Z. Physik.,* vol. 61, p. 792, 1930.

[29] R. E. Bell, "Exploiting a transmission grating spectrometer," *Rev. Sci. Instrum.,* vol. 75, p. 4158, 2004.

[30] Y. An, K.-J. Chung, D. Na and Y. Hwang, "Control and data acquisition system for versatile experiment spherical torus at SNU," *Fus. Eng. Des.,* vol. 88, p. 1204, 2013.

[31] A. Kramida, Y. Ralchenko, J. Reader and NIST ASD TEAM, "NIST Atomic Spectra Database (ver. 5.6.1)," 2018. [Online]. Available: https://physics.nist.gov/asd.

[32] A. Striganov and N.S.Sventitskii, Tables of spectral lines and neutral and ionized atoms, New York: Plenum Press, 1968.

[33] G. Herzberg, Atomic spectra and atomic structure, New York: Dover Press, 1994.

[34] C. W. Groetsch, The Theory of Tikhonov Regularization for Fredholm Integral Equations of the First Kind, Boston: Pitman, 1984.

[35] P. Hansen, "ANALYSIS OF DISCRETE ILL-POSED PROBLEMS BY MEANS OF THE L-CURVE," *SIAM Rev.,* vol. 34, p. 561, 1992.

[36] G. Golub, M. Heath and G. Wahba, "Generalized cross-validation as a methodforchoosing a good ridge parameter," *Technometrics,* vol. 21, p. 215, 1979.

[37] W.-H. Ko, H. Lee, Y. Jeon, K. Ida, J. Lee, S. Yoon, K. Lee, Y. Bae, Y. Oh and J. Kwak, "Rotation characteristics during the resonant magnetic perturbation induced edge localized mode suppression on the KSTAR," *Rev. Sci. Instrum.,* vol. 85, p. 11E413, 2014.

[38] Z. Chang and J. Callen, "Global energy confinement degradation due to macroscopic phenomena in tokamaks," *Nucl. Fusion,* no. 30, p. 219, 1990.

[39] J. Ongena, R. W. R. Koch and H. Zohm, "Magnetic-confinement fusion," *Nature Physics,* no. 12, p. 398, 2016.

[40] J. Menerad, B. LeBlanc, S. Sabbagh, M. Bell, R. Bell, E. Fredrickson, D. Gates, S.

Jardin, D. Johnson, S. Kaye, H. Kugel, R. Maingi, R. Maqueda, D. Mueller, M. Ono, F. Paoletti, S. Paul, C. Skinner and D. Stutman, "Ohmic flux consumption during initial operation of the NSTX spherical torus," *Nucl. Fusion,* no. 41, p. 1197, 2001.

[41] H. Furth, J. Killeen and M.Rosenbluth, "Finite-resistivity instabilities of a sheet pinch," *Phys. Fluids,* no. 6, p. 459, 1963.

[42] M. Choi, H. Park, G. Yun, W. Lee, N. L. J. K. Lee, W.-H. Ko, Y.-S. Park, B. Park and Y. In, "2D/3D electron temperature fluctuations near explosive MHD instabilities accompanied by minor and major disruptions," *Nucl. Fusion,* no. 56, p. 066013, 2016.

[43] S. Gerhardt, R. Bell, A. Diallo, D. Gates, B. LeBlanc, J. Menard, D. Mueller, S. Sabbagh, V. Soukhanovskii, K. Tritz and H. Yuh, "Disruptions, disruptivity and safer operating windows in the high-β spherical torus NSTX," *Ncul. Fusion,* no. 53, p. 043020, 2013.

[44] J. Scoville, R. L. Haye, A. Kellman, T. Osborne, R. Stambaugh, E. Strait and T. Taylor, "Locked modes in DIII-D and a method for prevention of the low density mode," *Nucl. Fusion,* no. 31, p. 875, 1991.

[45] D. Gates and T. Hender, "Resistive wall induced forbidden bands of mode rotation frequency on the COMPASS-D tokamak," *Nucl. Fusion,* no. 36, p. 273, 1996.

[46] F. Volpe, M. Austin, R. Haye, J. Lohr, R. Prater, E. Strait and A. Welander, "Advanced techniques for neoclassical tearing mode control in DIII-D," *Phys. plasmas,* no. 16, p. 102502, 2009.

[47] S. Yang, Y.-S. Na, D. Na, J.-K. Park, Y. Shi, W.H.Ko, S. Lee and T. Hahm, "Perturbative studies of toroidal momentum transport in KSTAR H-mode and the effect of ion temperature perturbation," *Nucl. Fusion,* vol. 58, p. 066008, 2018.

[48] D.H. Na, Yong-Su Na, S.G. Lee, C. Angioni, S.M. Yang, H.-S. Kim, T.S. Hahm, W.H. Ko, H. Jhang, W.J. Lee and KSTARTeam, "Observation of the intrinsic rotation in KSTAR Ohmic L-mode plasmas," *Nucl. Fusion,* vol. 56, p. 036011, 2016.

[49] J. Yang, Y. Kim, W. Jeong and Y. Hwang, "Simple and accurate method of diamagnetic flux measurement in Versatile Experimental Spherical Torus (VEST)," *Rev. Sci. Instrum.,* vol. 89, p. 103508, 2018.

[50] S. v. Goeler, W. Stodiek and N. Sauthoff, "Studies of Internal Disruptions and m=1 Oscillations in Tokamak Discharges with Soft—X-Ray Tecniques," *Phys. Rev. Lett.,* vol. 33, p. 1201, 1974.

[51] S. Gangadhara, "Ion heating during reconnection in the Madison Symmetric Torus reversed field pinch," *Phys. Plasmas,* vol. 15, p. 056121, 2008.

[52] A. Ejiri, S. Shiraiwa, Y. Takase, T. Yamada, Y. Nagashima, H. Kasahara, D. Iijima, Y. Kobori, T. Nishi, T. Taniguchi, M. Aramasu, S. Ohara, M. Ushigome and K. Yamagishi, "Ion temperature increase during MHD events on the TST-2 spherical tokamak," *Nucl. Fusion,* vol. 43, p. 547, 2003.

[53] Y. Ono, M. Yamada, T. Akao, T. Tajima and R. Matsumoto, "Ion Acceleration and Direct Ion Heating in Three-Component Magnetic Reconnection," *Phys. Rev. Lett.,* vol. 76, p. 3328, 1996.

[54] J. Yoo, M. Yamada, H. Ji and C. E. Myers, "Observation of Ion Acceleration and Heating during Collisionless Magnetic Reconnection in a Laboratory Plasma," *Phys. Rev. Lett.,* vol. 110, p. 215007, 2013.

[55] M. Yamada, "Study of energy conversion and partitioning in the magnetic reconnection layer of a laboratory plasma," *Phys. Plasmas,* vol. 22, p. 056501, 2015.

[56] X. H. Deng and H. Matsumoto, "Rapid magnetic reconnection in the Earth's magnetosphere mediated by whistler waves," *Nature,* vol. 410, p. 557, 2001.

[57] G. Fiksel, A. Almagri, B. Chapman, V. Mirnov, Y. Ren, J. Sarff and P. Terry, "Mass-Dependent Ion Heating during Magnetic Reconnection in a Laboratory Plasma," *Phys. Rev. Lett.,* vol. 103, p. 145002, 2009.

[58] E. Scime, S. Hokin, N. Mattor and C. Watts, "Ion heating and magnetohydrodynamic dynamo fluctuations in the reversed-field pinch," *Phys. Rev. Lett.,* vol. 68, p. 2165, 1992.

[59] Y. Ono, H. Tanabe, Y. Hayashi, T.Ii, Y. Narushima, T. Yamada, M. Inomoto and C. Cheng, "Ion and Electron Heating Characteristics of Magnetic Reconnection in a Two Flux Loop Merging Experiment," *Phys. Rev. Lett.,* vol. 107, p. 185001, 2011.

[60] S. Masuda, T. Kosugi, H. Hara, S. Tsuneta and Y. Ogawara, "A loop-top hard X-ray source in a compact solar flare as evidence for magnetic reconnection," *Nature,* vol. 371, p. 495, 1994.

[61] H. Hara, T. Watanabe, L. K. Harra, J. L. Culhane and P. R. Young, "PLASMA MOTIONS AND HEATING BY MAGNETIC RECONNECTION IN A 2007 MAY 19 FLARE," *ApJ,* vol. 741, p. 107, 2011.

[62] T. Gray, V. Lukin, M. Brown and C. Cothran, "Three-dimensional reconnection and relaxation of merging spheromak plasmas," *Phys. Plasmas,* vol. 17, p. 102106, 2010.

[63] P. Helander, L.-G. Eriksson, R. Akers, C. Byrom, C. Gimblett and M. Tournianski, "Ion Acceleration during Reconnection in MAST," *Phys. Rev. Lett.,* vol. 89, p. 235002, 2002.

[64] J. Galdon-Quiroga, M. Garcia-Munoz, K. McClements, M. Nocente, M. Hoelzl, A. Jacobsen, F. Orain, J. Rivero-Rodriguez, M. Salewski, L. Sanchis-Sanchez, W. Suttrop and E. Viezzer, "Beam-Ion Acceleration during Edge Localized Modes in the ASDEX Upgrade Tokamak," *Phys. Rev. Lett.,* vol. 121, p. 025002, 2018.

[65] P. Helander, L.-G. Eriksson and F. Andersson, "Runaway acceleration during magnetic reconnection in tokamaks," *Plasma Phys. Control. Fusion,* vol. 44, p. B247, 2002.

[66] K. Finken and e. al., "Toroidal Plasma Rotation Induced by the Dynamic Ergodic Divertor in the TEXTOR Tokamak," *Phys. Rev. Lett.,* vol. 94, p. 015003, 2005.

[67] J. D. Callen, "Effects of 3D magnetic perturbations on toroidal plasmas," *Nucl. Fusion*, vol. 51, p. 094026, 2011.

[68] A. Cole, C. Hegna and J. Callen, "Effect of Neoclassical Toroidal Viscosity on Error-Field Penetration Thresholds in Tokamak Plasmas," *Phys. Rev. Lett.*, vol. 99, p. 065001, 2007.

[69] A. Garofalo, K. Burrell, J. DeBoo, J. deGrassie, G. Jackson, M. Lanctot, H. Reimerdes, M. Schaffer, W. Solomon and E. Strait, "Observation of Plasma Rotation Driven by Static Nonaxisymmetric Magnetic Fields in a Tokamak," *Phys. Rev. Lett.*, vol. 101, p. 195005, 2008.

[70] A. J. Cole, C. C. Hegna and J. D. Callen, "Neoclassical toroidal viscosity and error-field penetration in tokamaks," *Phys. Plasmas*, vol. 15, p. 056102, 2008.

[71] R. L. Haye, R. Buttery, S. Guenter, M. Maraschek and H. Wilson, "Dimensionless scaling of the critical beta for onset of a neoclassical tearing mode," *Phys. Plasmas*, vol. 7, p. 3349, 2000.

[72] G. Huysmans, T. Hendera and B. Alper, "Identification of external kink modes in JET," *Nucl. Fusion*, vol. 38, p. 179, 1998.

국 문 초 록

VEST 장치에서 Bursting MHD 현상에 의한 이온 가열 및 회전 가속

김 유 성
에너지시스템공학부
(핵융합 및 플라즈마 공학 전공)
서울대학교 대학원

자장 가둠 플라즈마에서 MHD 불안정성이 발생하게 되면 가둠 성능을 저하시키며 심한 경우 플라즈마 붕괴 현상을 초래할 수 있다. 플라즈마 회전은 NTMs (Neoclassical Tearing Modes) 및 RWMs (Resistive Wall Modes)과 같은 다양한 MHD 불안정성에 안정화 효과를 갖는다. 반대로, MHD 불안정성 또한 플라즈마 회전에 상당한 영향을 줄 수 있다. MHD 불안정성과 플라즈마 회전 사이의 상호 작용을 이해하는 것은 매우 중요한 부분이지만, 이와 관련된 연구는 몇 가지 현상으로 제한되어 있으며 여전히 많은 부분이 해결되지 않은 채로 남아 있다. 그에 대한 이해를 향상시키기 위해서 본 연구에서는 Bursting MHD 현상이 발생했을 때 플라즈마 회전 및 이온온도에 대한 자세한 시변 특성을 확인하였다. 이러한 연구의 목적에 적합한 0.2-1 ms의 높은 시간 해상도를 가지는 고성능 이온 도플러 분광기 (IDS)가 새롭게 개발되었다. 이 IDS 진단을 통하여 매우 빠르게 발생하는 Bursting MHD

현상이 발생할 때에 상당한 이온 가열 및 플라즈마 회전 가속 현상을 최초로 관측하였다. 이러한 갑작스런 가속 현상을 설명하기 위해 여러 가지 가능한 메커니즘에 대해서 논의 하였고 실험결과와 비교하였다.

고속 IDS 시스템은 VEST에서 플라즈마 회전 및 이온 온도를 측정하기 위해 신중하게 설계되었고 설치되었다. 투과형 그레이팅을 이용하여 높은 광 수집 효율을 가지는 분광 시스템을 개발하였고, 광학 시스템의 각각의 컴포넌트들의 etendue를 일치시킴으로써 최적화를 수행하였다. 높은 효율의 분광기를 통하여 10 개의 공간 채널 측정의 경우 1 ms, 한 공간 채널에 대해서는 0.2 ms까지 달성하였다. 플라즈마 내부에 탄소 불순물의 라인 방출을 기반으로 측정이 수행되었으며, 측정 범위는 R> 0.5 m을 포함하게 된다.

IDS 시스템으로 측정한 스펙트럼은 측정 시선에 대해 적분된 스펙트럼을 측정하게 된다. 이러한 신호로부터 국소의 플라즈마 회전 및 이온 온도를 알아내기 위해서 도플러 단층 촬영 해석 기술을 사용하였다. 하지만 도플러 단층 촬영 해석 기술은 매우 불량 조건(ill-posed)인 문제이며, 계산된 결과는 비 물리적으로 진동하는 결과를 보이게 된다. 이러한 문제를 해결하고자 2 차 Tikhonov 정규화 방법을 도입하였고, 연속적인 것으로 생각되는 국부적인 플라즈마 특성을 적절하게 추정하는데 이용하였다. 이 방법은 재구성하는데 있어서 측정의 정확도뿐만 아니라 해의 연속성이 고려된 함수를 최적화하는 것을 기반으로 한다. 개발된 해석기법은 수치적인 몬테 카를로

(MC) 방법을 이용하여 측정된 스펙트럼의 오차의 전파를 고려하여 진단계의 불확정도 평가하였다.

Bursting MHD 현상은 방전기체를 적게 주입하고 낮은 안전계수로 운전하는 저항가열 방전에서 주로 나타난다. 이 현상은 플라즈마 전류, Loop voltage 및 고주파수의 Mirnov 신호의 급격한 변동이 특징이다. 이 현상이 발생했을 때, 수십 마이크로 초(~ $100\tau_A$)의 시간 상수를 가지는 매우 빠른 성장율이 Mirnov 신호를 통해서 확인되었다. 순간적인 MHD 활동이 발생할 때 이온 가열과 전류 반대 방향으로의 회전 가속이 일어남을 IDS 진단계를 통해 확인하였다. 이러한 변화는 플라즈마 전체 영역에 걸쳐서 관측되며, 이는 MHD 현상에 의해서 회전 토크 및 이온 가열이 플라즈마에 작용 함을 분명히 보여준다. 회전 및 이온온도는 300 μs 이내의 시간에서 매우 빠르게 증가하며, 가둠 시간상수를 가지고 천천히 회복하였다. Bursting MHD 현상에서 발생하는 순간적인 회전가속을 설명하기 위해서 여러가지 물리적인 메커니즘들을 살펴보았고, 시변 특성, 토크의 방향 및 토크의 크기 측면에서 논의가 진행되었다. 본 연구에서 평가한 메커니즘은 자장 재결합 유동, 자장 재결합 현상에 의한 토로이달 전계, 급격한 전자 유출, NTV 토크이다. 그 중에서도 MHD 현상에 의한 비대칭 자기장이 주는 NTV 토크가 가장 가능성 있는 메커니즘으로 나타났다.

본 연구에서 MHD 활동 중에 급격한 플라즈마 가속현상을 실험적으로 처음 연구되었다. 이 결과는 MHD 현상과 플라즈마 회전 사이의 상호작용을

이해하는데 도움을 줄 수 있다. 특히, 이 결과는 MHD 현상에 의한 회전에 의해서 스스로 안정화하는 자기재조직화(Self-organization)현상의 가능성을 암시한다.

주요어: 이온 도플러 분광, 플라즈마 회전, MHD 현상, 구형 토러스, NTV, VEST
Student Number: 2013-21007